ALMA MATER STUDIORUM
UNIVERSITÀ DI BOLOGNA

DEPARTMENT OF PHYSICS AND ASTRONOMY "A. RIGHI"

SECOND CYCLE DEGREE

PHYSICS

Sensitivity studies for Left-Right Symmetric Model Heavy Neutrinos Search with the ATLAS Experiment at LHC

Supervisor
Chiar.mo Prof. Maximiliano Sioli

Co-supervisors
Dott. Antonio Sidoti

Dott.ssa Elisa Sanzani

Defended by
Irene Borghesi

Graduation Session July 2026

Academic Year 2025/2026

Vinca dunque la perseveranza,
perchè, se la fatica è tanta,
il premio non sarà mediocre.
Tutte le cose preziose
son poste nel difficile.

Giordano Bruno

Abstract

Within the Standard Model of particle physics, neutrinos are massless. However, the experimental observation of flavour oscillations suggests otherwise, motivating the search for Beyond the Standard Model extensions.

Among these, Seesaw mechanisms offer a natural explanation for the lightness of neutrino masses, especially when embedded within the Left-Right Symmetric Model.

This thesis presents a feasibility study for a search for heavy Majorana neutrinos predicted by this model, based on data collected by the ATLAS detector at CERN.

The theoretical framework and the Monte Carlo simulation methods used to model both Standard Model background processes and the Beyond the Standard Model signal are introduced. The study then aims at improving the expected sensitivity of the search targeting the heavy-neutrino decay into a dilepton and multi-jets final state, using proton-proton collision data at centre-of-mass energy $\sqrt{s} = 13\,\text{TeV}$, corresponding to $140\,\text{fb}^{-1}$ integrated luminosity collected during LHC Run 2. The signal Monte Carlo model is validated at truth-level, alternative selection strategies are developed and their efficiency is quantified. Finally, the expected sensitivity is estimated through a statistical fit and compared to the baseline analysis approach.

Contents

Introduction

The Standard Model (SM) represents one of the greatest achievements of modern particle physics. It provides a remarkably good description of almost all current experimental data, by including fundamental particles and forces acting between them at the subatomic scale, with the notable exception of gravity. However, the model fails to account for several key experimental observations, such as the existence of non-zero neutrino masses, thus motivating the search for new physics Beyond the Standard Model (BSM).

BSM extensions typically introduce new particles and interactions at energy scales potentially accessible at colliders. Among these frameworks there are the so-called Seesaw mechanisms, which enlarge the SM by introducing heavy-neutrinos. An appealing model from an experimental point of view, leading to rich collider phenomenology, is the Left-Right Symmetric Model (LRSM), which naturally embeds Type-I and Type-II of the above-mentioned Seesaw mechanisms.

An excellent environment to probe such scenarios is the Large Hadron Collider (LHC), and more specifically, the ATLAS (A Torodidal LHC ApparatuS) detector with its optimal capability to reconstruct proton-proton interaction products and study processes with very small cross sections $O(10-100)$ fb, as the ones expected for BSM processes.

In this thesis, it is presented a search for heavy-neutrinos in proton-proton collision data collected by the ATLAS detector during LHC Run 2, at a centre-of-mass energy of $\sqrt{s} = 13$ TeV. Starting from an existing analysis that investigates a LRSM-allowed process never searched for at colliders, this work focuses on identifying and quantifying the optimal event selection strategy to maximise the signal selection efficiency and analysis sensitivity. The approach adopted is that of a relative efficiency study: starting from the baseline selection used in the ongoing ATLAS analysis, an alternative selection strategy is constructed by introducing variations to the final state objects requirements. Studies of the final-state leptons and jet transverse momentum thresholds are presented. The final goal is to compute a scale factor quantifying the gain or loss in signal efficiency induced by each variation of the event selection. This is complemented by an estimate of the expected sensitivity obtained through a statistical fit. Together, these results provide a concrete strategy for improving the signal sensitivity of the existing analysis, guiding future optimisation efforts towards the observation of this new class of phenomena.

In Chapter 1, the theoretical framework is presented, starting from a brief overview of the SM, which paves the way to more exotic BSM scenarios, including Seesaw mechanisms and LRSM. A description of the ATLAS detector, its sub-detectors, Trigger and Data Acquisition systems is given in Chapter 2, followed by the exploited reconstruction techniques and simulation strategies in Chapter 3. The truth-level MC validation and its results are presented in Chapter 4. Finally, Chapter 5 presents the event selection optimisation and scale factor computation, complemented by an approximate smearing-based extrapolation towards reconstruction level and a statistical fit estimating the expected analysis sensitivity.

Chapter 1

Theoretical framework

The SM is the most powerful tool able to describe the fundamental constituents of matter and their interactions, that includes three out of the four fundamental forces known in nature: electromagnetic, weak and strong force. However, some experimental observations such as the existence of non-zero neutrino masses, which are extraordinarily small compared with those of the other SM fermions, remain unaccounted for. A possible explanation for both the origin and the smallness of neutrino masses is offered by extensions of the SM that introduce Heavy Neutral Leptons.

In this chapter, an overview of the particles and forces included in the SM is discussed. A description of the BSM frameworks which can address this problem is then provided. In particular, the focus is placed on Seesaw mechanisms and the LRSM, which embeds Type-I and Type-II Seesaw scenarios.

1.1 The Standard Model of particle physics: theoretical formalism

In terms of *Group Theory*, the SM is a Quantum Field Theory (QFT) [1] built upon the principle of local gauge invariance of the group

$$\mathrm{SU}(3)_\mathrm{C} \times \mathrm{SU}(2)_\mathrm{L} \times \mathrm{U}(1)_\mathrm{Y} \tag{1.1}$$

where the Non-Abelian Special Unitary group $\mathrm{SU}(3)_\mathrm{C}$ represents the strong interaction, governed by Quantum Chromodynamic (QCD) (Sec. 1.3), while the combination of $\mathrm{SU}(2)_\mathrm{L} \times \mathrm{U}(1)_\mathrm{Y}$ represents the unification of electromagnetic and weak interaction into Electroweak interaction (Sec. 1.5), described by the Glashow-Weinberg-Salam (GSW) Model. Finally the Unitary group $\mathrm{U}(1)_\mathrm{Y}$ is associated to the weak hypercharge. The subscripts in (Eq. 1.1) denote respectively the colour charge of the strong interaction (C), the weak isospin of the left-handed (LH) sector (L) and the weak hypercharge (Y).

Within the SM, interactions between matter fields consist in an exchange of elementary particles called mediators or gauge bosons. Using Lie's Algebra group formalism, the number of these gauge bosons can be found and this is related to the number of generators of each group:

- **SU**(3) has 8 generators corresponding to the 8 mediators of strong force, the massless gluons;

- **SU**(2) has 3 generators corresponding to the 3 gauge fields W_i;
- **U**(1) has 1 generator, corresponding to the gauge field B.

Notice that, W_i and B are not the actual electroweak physical bosons $W^{\pm}$ and Z^0. The physical mediators are instead a linear combinations of the gauge fields W_i and B.

Under the exact local gauge symmetry (Eq. 1.1) all bosons are predicted as massless, nevertheless, $W^{\pm}$ and Z^0 are proved to be massive. To explain this, Higgs, Englert and Brout proposed the Spontaneous Symmetry Breaking (SSB) mechanism [2, 3], which introduces an additional neutral scalar (spin-0) Higgs field, able to give mass to the SM particles (Sec. 1.5.1).

1.1.1 The Standard Model constituents

The fundamental particles of the SM can be distinguished into two classes, depending on their spin [4]: the mediators of interactions, *bosons*, have an integer spin and follow the so called Bose-Einstein statistics, while *fermions*, which represent the elementary constituents of matter, have semi-integer spin and follow the Fermi-Dirac statistics. In the SM there are twelve fundamental spin-$\frac{1}{2}$ fermions, with a corresponding antiparticle with opposite quantum numbers each. The SM fermions are organised into three *generations* with increasing mass (Fig. 1.1) and each generation contains one $\mathrm{SU}(2)_\mathrm{L}$ doublet of quarks and one $\mathrm{SU}(2)_\mathrm{L}$ doublet of leptons:

$$\begin{pmatrix} u \\ d \end{pmatrix}_\mathrm{L}, \quad \begin{pmatrix} c \\ s \end{pmatrix}_\mathrm{L}, \quad \begin{pmatrix} t \\ b \end{pmatrix}_\mathrm{L}, \qquad \begin{pmatrix} \nu_e \\ e^- \end{pmatrix}_\mathrm{L}, \quad \begin{pmatrix} \nu_\mu \\ \mu^- \end{pmatrix}_\mathrm{L}, \quad \begin{pmatrix} \nu_\tau \\ \tau^- \end{pmatrix}_\mathrm{L}. \tag{1.2}$$

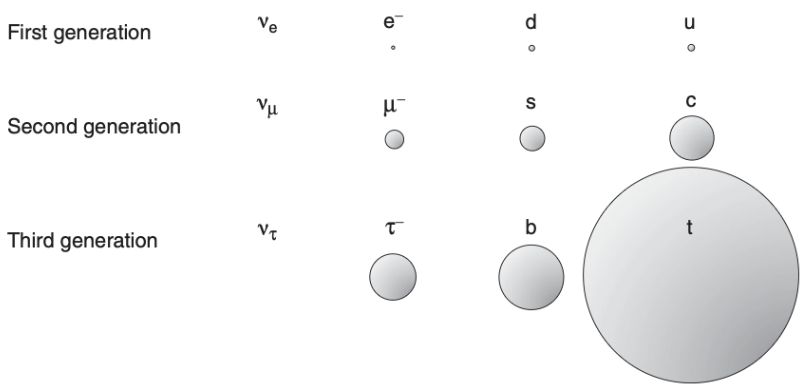

Figure 1.1: Graphical representation of the three generations of fermions: the masses of the elementary particles are depicted as spheres of constant density. In reality, fundamental particles are believed to be point-like [4].

The right-handed (RH) components of the charged fermions transform as $\mathrm{SU}(2)_\mathrm{L}$ singlets: u_R, d_R, e^-_R, together with their second and third-generation counterparts. Crucially, this means that no RH-neutrino is present in the SM framework.

Quarks carry colour charge and are therefore directly subject to the strong interaction, differently from leptons which are colour-neutral. However, both quarks and charged leptons can participate to electroweak interactions. The existence of exactly three generations of fermions is one of the unexplained features of the SM.

Finally, the particle spectrum is completed by the presence of a spin-0 Higgs boson H, observed for the first time in 2012 by the ATLAS and CMS Collaborations[1] [5, 6], representing the only physical scalar of SM, remaining after the $\mathrm{SU}(2)_\mathrm{L} \times \mathrm{U}(1)_\mathrm{Y}$ gauge symmetry breaking.

1.2 Quantum Electrodynamics

Quantum ElectroDynamics (QED) [4] is an Abelian theory describing electromagnetism, which involves interactions between charged particles, mediated by the spin-1 massless photon. It is based on the gauge group $\mathrm{U}(1)$ and is derived starting from Maxwell's equations and the free Dirac Lagrangian

$$\mathcal{L}_D = \bar{\psi}(i\gamma^\mu \partial_\mu - m)\psi \tag{1.3}$$

where ψ is the Dirac spinor, $\bar{\psi} = \psi^\dagger \gamma_0$ is the adjoint spinor and m is the fermion mass, to which gauge invariance under local $\mathrm{U}(1)$ phase transformation

$$\psi \longrightarrow \psi' = e^{-ie\alpha(x)}\psi \tag{1.4}$$

is imposed. This forces the introduction of a gauge field, the photon field, and the replacement of the derivative with the so called covariant derivative $D_\mu = \partial_\mu + ieA_\mu$. At this point, the Lagrangian for QED can be written as

$$\mathcal{L}_{QED} = \bar{\psi}(i\gamma^\mu \partial_\mu - m)\psi - \frac{1}{4}F_{\mu\nu}F^{\mu\nu} - j^\mu A_\mu \tag{1.5}$$

where $j^\mu = q\bar{\psi}\gamma^\mu\psi$ represents the conserved electromagnetic current, that arises as a direct consequence of Noether's theorem[2] [7] applied to $\mathrm{U}(1)$, and $F_\mu = \partial_\mu A_\nu - \partial_\nu A_\mu$ Maxwell's electromagnetic tensor. The terms that compose this Lagrangian represent respectively the free propagation of the fermion ($\bar{\psi}(i\gamma^\mu \partial_\mu - m)\psi$), the free propagation of the photon ($\frac{1}{4}F_{\mu\nu}F^{\mu\nu}$) and the interaction between the two ($j^\mu A_\mu$). Notice that, a mass term for the photon of the type $\frac{1}{2}m^2 A_\mu A^\mu$ would break local gauge invariance, therefore the photon is required to be strictly massless.

1.3 Quantum Chromodynamics

Quantum Chromodynamics (QCD) [8] is the gauge theory of the strong interaction, described by the $\mathrm{SU}(3)_\mathrm{C}$ gauge group. The theory was developed in the early 1970s and accounts for the binding of quarks into hadrons and the interactions among hadrons. The QCD Lagrangian is

$$\mathcal{L}_{\mathrm{QCD}} = \sum_q \bar{\psi}_{q,a}(i\gamma^\mu \partial_\mu \delta_{ab} - g_s \gamma^\mu t^C_{ab} A^C_\mu - m_q \delta_{ab})\psi_{q,b} - \frac{1}{4}F^A_{\mu\nu}F^{A\,\mu\nu}\,, \tag{1.6}$$

[1] In July 2012, the ATLAS and CMS collaborations announced the observation of a new scalar boson with mass $m_H \simeq 125$ GeV, consistent with the SM Higgs boson, representing one of the most significant experimental confirmations of the SM.

[2] Noether's theorem relates continuous symmetries with conserved quantities. It states that every continous symmetry of the Lagrangian gives rise to a conserved current j^μ since the equation of motion implies $\partial_\mu j^\mu = 0$; moreover, every conserved current gives rise to a conserved charge $Q = \int_{R^3} d^3x\, j^0$.

where the sum is done over quark flavours $q \in \{u, d, s, c, b, t\}$, $\bar{\psi}_{q,a}$ and $\psi_{q,b}$ are the quark field spinors of colour index a and b, γ^μ are the 4×4 Dirac matrices, g_s is the strong coupling constant (the dimensionless $\alpha_s = g_s^2/(4\pi)$ is the analogous to the fine-structure constant in electromagnetism), $t^C_{ab} = \frac{1}{2}\lambda^C$ where λ^C are the Gell-Mann matrices, related to the 8 generators of SU(3), A^C_μ ($C = 1, \ldots, 8$) are the eight gluon fields associated with the generators of $\mathrm{SU}(3)_\mathrm{C}$, m_q are the quark masses and $F^A_{\mu\nu}$ is the gluon field strength tensor, that can be expressed as

$$F^A_{\mu\nu} = \partial_\mu A^A_\nu - \partial_\nu A^A_\mu + g_s f^A_{BC} A^B_\mu A^C_\nu \,, \tag{1.7}$$

where f^A_{BC} are the SU(3) structure constants. The non-Abelian nature of $\mathrm{SU}(3)_\mathrm{C}$, given by the fact that its generators do not commute, $[t^A, t^B] = i f_{ABC} t^C$, implies that gluons carry colour charge themselves, giving rise to three and four-gluon self-interaction vertices (Fig. 1.2), a very defining feature which has no counterpart in electromagnetism, for example.

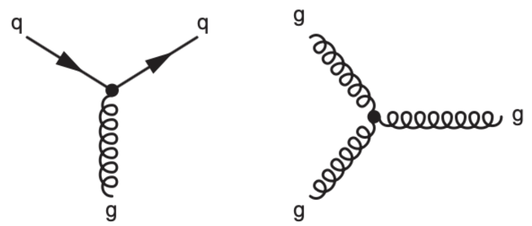

Figure 1.2: QCD vertices: the presence of self-interactions arises from the request of local gauge invariance under $\mathrm{SU}(3)_\mathrm{C}$ [4].

A peculiarity of the strong $\alpha_s = g_s^2/(4\pi)$ is that it depends on the energy scale of the interaction $\alpha_s(Q^2)$, so it is said to be *running* and therefore indicates the effective strength of the strong interaction in that given process, at a given energy scale. This energy dependence arises from the structure of the QCD vacuum and is responsible for increasing α_s at low energies, while decreasing it at $\Lambda_\mathrm{QCD} \simeq 200\,\mathrm{MeV}$. This strong-coupling regime is responsible for the so called *confinement* of quarks and gluons, which are never observed as free particles but are always bound into colour-neutral states, called hadrons.

1.4 Weak interactions

Weak interactions are the one responsible for β-decays. In 1930, W. Pauli [9] hypothesized the existence of a new particle, the neutrino, to solve an apparent problem of violation of energy, momentum and angular momentum conservation for these types of decays. Pauli's idea was then formalized by E. Fermi [10] into a model for beta decays, which inspired the modern description of all weak-interaction processes.

1.4.1 Fermi theory for β-decay

In his original theory (1934), in analogy with QED, Fermi represented β-decay as an interaction between two currents, each carrying the weak charge. Unlike the electromagnetic force, which is mediated by the photon and has a long range ($R \longrightarrow \infty$, so massless boson), the weak force has a very short range ($R = 10^{-18}$ m), so the currents interact directly at a single point, without a mediator (point-like interaction). This interaction causes a transfer of electric (weak) charge between the currents, changing the nature of the particles involved. In neutron beta-decay, for instance, the neutron current gains one unit of charge and transforms into a proton-current, while the electron-current loses one unit of charge and transforms into a neutrino current. At the end, the overall process is charge-neutral, but individual currents "transfer" charge between each other.

Although providing excellent explanations and predictions for experimental observables, this theory was still incomplete. The dimensionality of the coupling constant (G_{F}, which characterises the strength of the interaction) makes the theory non-renormalisable and the assumption of parity[3] conservation was later rejected following the results of Madame Wu's experiment [11]. Nevertheless, Fermi's theory still remains an effective low-energy limit for electroweak interactions (Sec. 1.5).

1.4.2 Important features

Weak interactions [12] can be described with the Non-Abelian $\mathrm{SU}(2)_{\mathrm{L}}$ symmetry group, known as the weak isospin group, which has three generators I_a, $a = 1, 2, 3$. In two-dimensional representation, $I_a = \frac{\tau_a}{2}$, where τ_1, τ_2, τ_3 are the three Pauli Matrices. An important feature that distinguishes weak interactions from the other two types mentioned before, which are "felt" only by electrically-charged or colour-charged particles respectively, is that all the twelve fundamental fermions carry the weak isospin and therefore, they can all undergo weak interactions.

A peculiarity of weak interactions is also that they have a chiral nature, coupling only to LH $\mathrm{SU}(2)_{\mathrm{L}}$ fermionic doublets. RH fields instead, are said to be singlets under $\mathrm{SU}(2)_{\mathrm{L}}$ gauge group and so do not participate in weak charged-current (CC) interactions (Sec. 1.4.3). This fact was established experimentally thanks to the observation of parity violation in nuclear β-decays with the famous Madame Wu's experiment, and it is taken into consideration in the SM via the $V - A$ (vector minus axial-vector) structure of weak CC

$$j^{\mu}_{\mathrm{CC}} = \frac{1}{\sqrt{2}} \bar{\nu}_L \gamma^{\mu} l_L = \frac{1}{2\sqrt{2}} \bar{\nu} \gamma^{\mu} (1 - \gamma^5) l \tag{1.8}$$

where $\gamma^5 = i\gamma^0\gamma^1\gamma^2\gamma^3$ is the chirality operator[4], that couples $W^{\pm}$ bosons, mediators of CC interactions, to lepton doublets. A consequence of the chiral structure of this type of interactions is that the SM neutrinos are only LH [13], while their antiparticles are always RH. Therefore, neutrinos appear only in the $\mathrm{SU}(2)_{\mathrm{L}}$ doublet and have no RH counterpart in the field content. Moreover, since no gauge-invariant Dirac mass term $m_D \bar{\nu}_L \nu_R$ can be written for the mass term of the Lagrangian of weak interactions (Sec. 1.5.1), neutrinos are massless in the SM (in conflict with the observation of neutrino flavour oscillations[5] [14, 15]).

Finally, since weak interactions violate parity ($\hat{P}\phi(\vec{x}, t) = \phi(-\vec{x}, t)$) and also charge conjugation ($\hat{C}$(particle) = antiparticle), for the CPT-theorem they also violate time reversal ($\hat{T}\phi(\vec{x}, t) = \phi(\vec{x}, -t)$), again differently with respect to both QED and QCD interactions.

[3] Parity is a symmetry transformation for which $\psi \to \hat{P}\psi = \gamma_0\psi$, where ψ is a solution of the Dirac equation and $\hat{P}$ is the parity operator.

[4] Chiral projection operators are defined as $P_L = \frac{1}{2}(1 - \gamma^5)$ and $P_R = \frac{1}{2}(1 + \gamma^5)$ and are used to decompose Dirac spinors into LH and RH chiral components.

[5] Neutrino oscillations are a quantum mechanical phenomenon, in which a neutrino of a specific flavour (electron, muon or tau) can transform into one of another flavour, as it propagates through space.

1.4.3 Mediators of the interactions

Weak interactions can be mediated by three massive vector bosons $W^{\pm}$ and Z^0 (Fig. 1.3), which do not bring a colour-charge. The Z^0 boson mediates neutral current (NC) interactions, whose existence was confirmed experimentally at CERN in 1973, with the Gargamelle bubble chamber [16]. CC interactions instead are mediated by $W^{\pm}$ bosons.

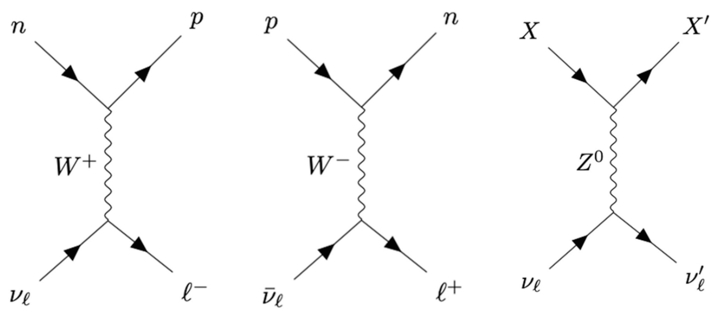

Figure 1.3: Examples of Feynman diagrams for charged current interaction mediated by W^+ (on the left) and W^- (in the middle), and neutral current interaction mediated by Z^0 (on the right). [17]

Despite having an intrinsic coupling strength $\alpha_W \simeq \frac{1}{30}$, larger than the one for QED ($\alpha \simeq \frac{1}{137}$), the weak interaction is heavily suppressed at low energies due to the large masses of its mediators $W^{\pm}$ and Z^0, respectively $M_{W^{\pm}} \simeq 80.4\,\text{GeV}$ and $M_{Z^0} \simeq 91.2\,\text{GeV}$. At energies of the order of the Fermi scale (approximately 100 GeV), however, this suppression is lifted and the weak interaction is expected to reach a strength comparable to the electromagnetic one, making their unification possible.

1.5 Electroweak theory

In the 1960s, Glashow, Weinberg and Salam (GWS) formulated the gauge theory of ElectroWeak (EW) interactions [18, 19, 20], which together with the Spontaneous Symmetry Breaking mechanism (SSB), allows for the correct unification of weak and electromagnetic interactions.

This gauge theory is based on the group $\mathrm{SU}(2)_\mathrm{L} \times \mathrm{U}(1)_\mathrm{Y}$ [12], where the Special Unitary group $\mathrm{SU}(2)_\mathrm{L}$ of weak interactions unifies with the Unitary group $\mathrm{U}(1)_\mathrm{Y}$, where Y stands for hypercharge, related to the third component of the weak isospin I_3 through the Gell-Mann-Nishijima relation [21, 22]

$$\mathrm{Q} = I_3 + \frac{\mathrm{Y}}{2} \tag{1.9}$$

being Q the charge operator.

In the EW theory, two independent coupling constants are considered: g, for $\mathrm{SU}(2)_\mathrm{L}$, and g', for $\mathrm{U}(1)_\mathrm{Y}$. Moreover, to preserve local gauge invariance of the new group, also three bosonic fields A_a^μ with $a = 1, 2, 3$, associated with the three generators of $\mathrm{SU}(2)_\mathrm{L}$ group (I_1, I_2, I_3), and one bosonic field B_μ, associated with the generator of $\mathrm{U}(1)_\mathrm{Y}$ group (Y), are needed. However, these are not yet the physical gauge bosons that mediate EW interactions, which actually appear thanks to the mixing of fields after Electroweak Spontaneous Symmetry Breaking (EWSSB).

1.5.1 Higgs mechanism and Electroweak Symmetry Breaking

In the SM, all elementary particles are massless at the Lagrangian level before SSB; however, it is experimentally proven that the $W^{\pm}$ and Z^0 bosons, as well as the other fermions of the SM, are massive. These masses can be provided by a mechanism which is known as the Brout-Englert-Higgs mechanism of SSB. In the GWS model, this mechanism is applied to the $\mathrm{SU}(2)_\mathrm{L} \times \mathrm{U}(1)_\mathrm{Y}$ local gauge symmetry and is able to provide masses for the three weak mediators $W^{\pm}$ and Z^0 bosons, keeping the electromagnetic mediator, the photon, massless.
In general, the Higgs mechanism is based on two complex scalar fields placed in an $\mathrm{SU}(2)_\mathrm{L}$ weak isospin doublet ϕ, with hypercharge Y = +1,

$$\phi = \begin{pmatrix} \phi^+ \\ \phi^0 \end{pmatrix} = \frac{1}{\sqrt{2}} \begin{pmatrix} \phi_1 + i\phi_2 \\ \phi_3 + i\phi_4 \end{pmatrix}, \tag{1.10}$$

where the neutral component of the doublet ϕ^0 and the charged component ϕ^+ are needed to generate the electroweak bosons. The Lagrangian for this doublet is

$$\mathcal{L}_{\mathrm{Higgs}} = (D_\mu \phi)^\dagger (D^\mu \phi) - V(\phi)\,, \tag{1.11}$$

with D_μ standing for the covariant derivative and V being the Higgs potential

$$V(\phi) = \mu^2 \phi^\dagger \phi + \lambda(\phi^\dagger \phi)^2, \quad \lambda > 0. \tag{1.12}$$

This potential, for $\mu^2 < 0$, has an infinite set of degenerate minima satisfying

$$\phi^\dagger \phi = -\frac{\mu^2}{2\lambda} \equiv \frac{v^2}{2} \tag{1.13}$$

where v is the so called Vacuum Expectation Value (VEV). By choosing a specific value for v, the $\mathrm{SU}(2)_\mathrm{L} \times \mathrm{U}(1)_\mathrm{Y}$ symmetry can be spontaneously broken down to $\mathrm{U}(1)_\mathrm{Y}$, preserving electromagnetic gauge invariance. This choice is dictated by the need of the neutral photon to remain massless after SSB and so the neutral scalar field ϕ^0 needs to acquire a non-zero VEV

$$\langle 0|\phi|0\rangle = \frac{1}{\sqrt{2}} \begin{pmatrix} 0 \\ v \end{pmatrix}. \tag{1.14}$$

At this point, considering Goldstone Theorem[6] [23, 24] and working in the so called Unitary Gauge, where the three Goldstone bosons (which would be massless scalar degrees of freedom otherwise) are absorbed as the longitudinal states of polarisation for the weak bosons $W^{\pm}$ and Z^0, the Higgs doublet can be rewritten as

$$\phi = \frac{1}{\sqrt{2}} \begin{pmatrix} 0 \\ v + h(x) \end{pmatrix}, \tag{1.15}$$

where $h(x)$ is the physical Higgs field. Substituting this into the Lagrangian (Eq. 1.11), in the term containing the covariant derivative $D_\mu = \partial_\mu + igA^a_\mu I_a + ig'\frac{Y}{2}B_\mu$, the gauge boson masses can be determined. For the $W^{\pm}$, the mass is found to be equal to

$$m_W = \frac{1}{2} g v, \tag{1.16}$$

[6]The Goldstone Theorem states that whenever a continuous global symmetry is spontaneously broken, the spectrum contains at least a massless, spin-zero boson and there are as many Goldstone Bosons as the broken generators of the symmetry.

where g is exactly the weak coupling constant and v the VEV of the Higgs field. For the photon and the Z^0 instead, considering the term in the Lagrangian that contains a mix between the A^3_μ and B_μ and diagonalising the resulting mass matrix, one massless eigenstate, identified as the photon, and one massive eigenstate, identified as the Z^0, can be found

$$A_\mu = \cos\theta_W B_\mu + \sin\theta_W A^3_\mu, \qquad Z_\mu = -\sin\theta_W B_\mu + \cos\theta_W A^3_\mu, \tag{1.17}$$

where the angle θ_W is known as the Weinberg angle and is defined such that $\sin^2\theta_W = 1 - \frac{m_W^2}{m_Z^2}$. Finally, the mass of the Z^0 can be written as

$$m_Z = \frac{1}{2} v \sqrt{g^2 + g'^2} = \frac{m_W}{\cos\theta_W}, \tag{1.18}$$

correctly predicted by the GSW model and experimentally confirmed at LEP in the 1990s [25].

Fermion masses and Yukawa couplings

For what concerns fermion masses instead, they are generated thanks to the Yukawa interactions between the Higgs doublet and fermionic fields. In the lepton sector, the Yukawa part of the Lagrangian can be written as:

$$\mathcal{L}^l_{\text{Yukawa}} = -y_l\,\bar{L}\phi\,l_R + \text{h.c.}\,, \tag{1.19}$$

where y_l is the Yukawa coupling for leptons and, after SSB, the mass for charged leptons appears as

$$m_l = \frac{y_l v}{\sqrt{2}}. \tag{1.20}$$

A similar expression can be found also for the quarks, involving the so called Cabibbo-Kobayashi-Maskawa (CKM) matrix[7] [26, 27]. Nevertheless, since in the SM there are no RH-neutrinos, there is no Yukawa term for them, so their masses cannot be explained using the same mechanism as above, as will be discussed in Sec. 1.7.

1.6 Limitations of the Standard Model

Despite its extraordinary success, the SM is an incomplete theory and this fact is supported by several experimental observations and theoretical considerations, like:

- **Neutrino masses**: the observation of neutrino flavour oscillations is the most evident experimental proof that neutrinos have non-zero masses, in contradiction with what expected from the SM, which predicts them as massless;

[7] The CKM unitary matrix relates the mass eigenstates (d, s, b) to the weak eigenstates (d', s', b') in the quark sector. The unitary matrix for neutrino mixing is instead the Pontecorvo-Maki-Nakagawa-Sakata (PMNS) matrix.

- **Matter-antimatter asymmetry in Universe**: as cosmological observations have shown, the Universe is composed almost entirely by matter. However, right after the Big Bang, the difference between baryons and antibaryons was zero, meaning that there was the same amount of matter and antimatter. To explain this, the three Sakharov conditions [28] required for baryogenesis involve: baryon number violation, C and CP violation and departure from thermal equilibrium. Even if these conditions are qualitatively satisfied in the SM, the amount of CP violation in the quark sector is insufficient to account for the observed asymmetry;

- **Dark matter**: evidence for dark matter emerged from two independent lines of observation. In the 1930s, F. Zwicky noted that the velocity dispersion of galaxies in the Coma Cluster was far too large to be explained by the visible mass alone, postulating the existence of unseen matter. Later, in the 1960s, V.C. Rubin studied stellar motions in the Andromeda Galaxy and found an inconsistency involving the behaviour of galactic rotation curves. With the distribution of visible matter alone, Newtonian gravity predicts that rotational velocities should decline with increasing distance from the galactic centre. However, observations revealed that rotation curves remain flat also at large radii. This implies the existence of a non-luminous, gravitationally interacting mass component, which was indicated as dark matter. This is now estimated to constitute roughly 84% of all matter in the Universe, but it is not accounted for in the SM;

- **Absence of gravity**: even if it has a very solid structure, the SM does not include gravity. This is not a problem in the region of interest of collider experiments, where gravitational effects are believed to be negligible, but in the end, a complete theory must unify all of the four fundamental forces.

Overall, these facts suggest that the SM must be revised in some sense, to reach a more fundamental form and this legitimates the study of BSM physics.

Among all the experimental facts listed above, neutrino masses represent the most direct proof of BSM physics, since they require at least the introduction of new fields to generate the observed flavour oscillations. The following discussion is dedicated to the introduction of these new theoretical frameworks, which aim to connect the existence and the smallness of neutrino masses with a new BSM scenario at high energy scales.

1.7 Neutrino mass generation mechanisms: Standard Model and beyond

Up to date, only upper limits on neutrino masses could be established experimentally.

The most stringent constraints on electron neutrino mass were obtained by the KATRIN experiment [29] (2025), through the study of the endpoint of the electron energy spectrum in nuclear β-decay of tritium (^3H), leading to

$$m_{\nu_e} < 0.45\,\mathrm{eV} \tag{1.21}$$

at 90% Confidence Level (CL).
Constraints on muon neutrino mass instead, arose from measurements performed at PSI [30],

involving the kinematics of pion-decay, leading to

$$m_{\nu_\mu} < 170\,\text{KeV} \tag{1.22}$$

at 90% CL.
Finally, limits on the tau neutrino mass were obtained from direct kinematical studies of rare tau-decay $\tau^- \longrightarrow 3\pi^- 2\pi^+ \nu_\tau$ by ALEPH (LEP) [31], yielding

$$m_{\nu_\tau} < 18.2\,\text{MeV}. \tag{1.23}$$

at 95% CL.

It is worth noticing that neutrino masses are only upper bounds and their absolute values and hierarchy are still unknown. Nevertheless, these masses are much smaller with respect to the ones of the other fermions (Fig. 1.4) and the origin of this huge suppression is still an open question in particle physics.

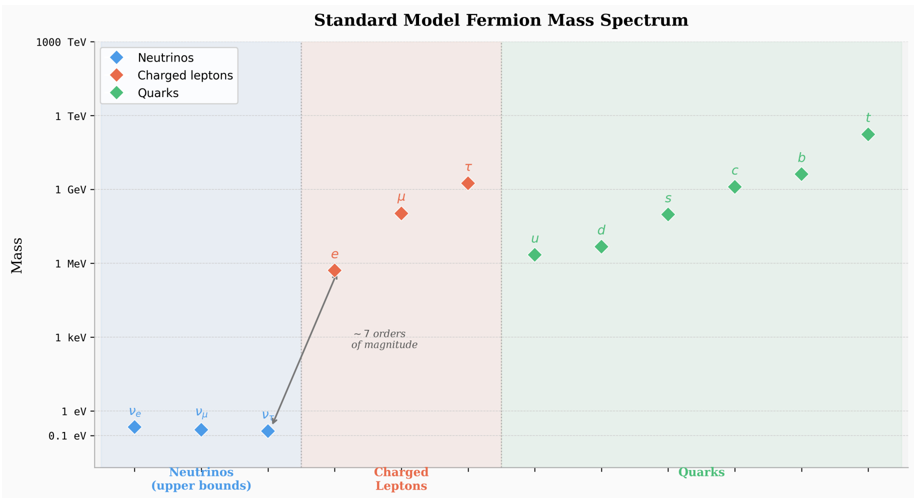

Figure 1.4: Fermion mass spectra: the log scale on the y-axis highlights the range of masses. This spans over 17 orders of magnitude, from the sub-eV for neutrinos, to the approximately 173 GeV of the top quark. The arrow is used to underline that from the heaviest neutrino to the lightest charged lepton there are approximately 7 orders of magnitude, still unexplained.

A simple way to generate these small neutrino masses is to introduce RH heavy-neutrinos, one for each generation [32].

1.7.1 Naturalness problem

It is possible to show that, if neutrinos acquire their masses through the same mechanism of all other fermions, this would lead to a "naturalness" problem, involving the value of the Yukawa coupling. In fact, assuming neutrinos to be pure Dirac particles and introducing RH-neutrino fields within the SM Lagrangian, the fermion mass terms, generated after EWSSB, would take the form

$$m_\nu = y_\nu \frac{v}{\sqrt{2}} \tag{1.24}$$

$$m_l = y_l \frac{v}{\sqrt{2}} \tag{1.25}$$

where $v \simeq 246$ GeV is the VEV and y_ν, y_l are the Yukawa couplings for neutrinos and leptons, respectively.

Now, considering the mass of the electron $m_e \simeq 0.5$ MeV and a neutrino mass of $m_\nu \simeq 0.05$ eV (coherent with limits from oscillation experiments), the couplings would look like

$$y_\nu \simeq 10^{-13} \ll y_l \simeq 10^{-6} \tag{1.26}$$

with 7 orders of magnitude of difference between one another.

This problem can be solved by extending the model to include Majorana fermions, as will be discussed in the following section.

1.7.2 Majorana fermions

Neutral, massive fermions can be described with Majorana spinors $\phi = \phi_L + \phi_L^C$ (or $\phi = \phi_R + \phi_R^C$) [12]. If neutrinos were assumed to be Majorana particles, then they would satisfy the Majorana condition $\nu = \nu^C$, meaning that there would be no distinction between neutrinos and their antiparticles.

Within this framework, neutrino masses can arise from BSM mechanisms, through the generation of Majorana mass terms. In particular, a Majorana mass can be constructed by coupling the LH-neutrino field ν_L to its charge-conjugate ν_L^C:

$$\mathcal{L}_M = \frac{1}{2} m_L \overline{(\nu_L)^C} \nu_L + \text{h.c.} \tag{1.27}$$

where C is the operator of charge-conjugation. This term is not invariant under EW gauge symmetry group $\mathrm{SU(2)_L \times U(1)_Y}$. Nevertheless, two possibilities exist to obtain a gauge-invariant Majorana mass:

- **Effective Field Theory** (EFT): in which neutrino masses arise from non-renormalisable operators, with dimension $d > 4$, added to the SM Lagrangian. In this case, the smallness of neutrino masses is naturally explained by the presence of a high-energy scale $\Lambda \gg v$ and, at leading order, this results in

$$m_\nu = \frac{v^2}{2\Lambda} \tag{1.28}$$

- **Seesaw mechanisms**: introduced in 1979, even before the first evidence for neutrino masses, which reduce to EFT at low energy.

1.8 EFT and Seesaw mechanisms

From an EFT perspective [33], the SM Lagrangian can be extended by adding dimension $d > 4$ operators, together with a factor Λ^{4-d}, in order to preserve the true mass dimension $[E]^4$ of the Lagrangian:

$$\mathcal{L}_{EFT} = \mathcal{L}_{SM} + \mathcal{L}_5 + \ldots \tag{1.29}$$

The $d = 5$ operator $\mathcal{L}_5 = \frac{c_5^{\alpha\beta}}{\Lambda} \left(\overline{L_\alpha^C}\, \tilde{\phi}^*\right) \left(\tilde{\phi}^\dagger L_\beta\right) + \text{h.c.}$ (Weinberg operator [34]), where c_5 is the dimensionless Wilson coefficient, $L = (\nu_L, l_L)^T$ is the LH lepton doublet, L^C is the charge-conjugate, ϕ is the SM Higgs doublet and $\tilde{\phi} = i\sigma_2\phi^*$, can lead directly to neutrino masses. Indeed, after the EWSSB

$$(m_\nu)^{\alpha\beta} = c_5^{\alpha\beta}\frac{v^2}{\Lambda} \tag{1.30}$$

and after diagonalisation, the eigenvalues of the mass matrix give the physical masses [12].

In the case of Seesaw mechanisms, the scale of Λ is related with the mass of a new heavy RH-neutrino, which acts as the Seesaw partner of the light active LH one. In this case, the light neutrino mass becomes

$$m_\nu = y_\nu^2\frac{v^2}{M_R} \tag{1.31}$$

where $m_D = y_\nu v$ is the Dirac mass and M_R is the heavy RH-neutrino mass, suppressed by the large scale of M_R [35, 36, 37, 38].

1.8.1 Seesaw models

Due to the presence of lepton weak doublets and SM Higgs doublet in $\mathcal{L}_5$, both singlet and triplet mediators can appear. Within this framework, three different realisations [39] of Seesaw mechanism can be identified:

1. *Type-I* Seesaw: neutrino masses arise from the exchange of heavy fermion singlets N_R. This leads to a Majorana mass for the light active neutrino $m_\nu \simeq Y_N^T\frac{v^2}{M_N}Y_N$, suppressed by the large Majorana mass M_N of the singlet;

2. *Type-II* Seesaw: introduces an $\mathrm{SU}(2)_\mathrm{L}$ scalar triplet $\Delta = (\Delta^{++}, \Delta^+, \Delta^0)$ [40], which couples directly to LH lepton doublets and their charge conjugates, inducing Lepton Number Violation (LNV). The resulting neutrino mass is $m_\nu \simeq Y_\Delta\frac{\mu_\Delta}{M_\Delta^2}v^2$, where μ_Δ denotes the trilinear coupling between the scalar triplet and the Higgs doublet. This model, together with Type-I, can be naturally embedded within the LRSM (Sec. 1.9);

3. *Type-III* Seesaw: introduces an $\mathrm{SU}(2)_\mathrm{L}$ fermionic weak triplet $\Sigma = (\Sigma^+, \Sigma^0, \Sigma^-)$ [40]. Differently from Type-I, Σ is not sterile, however it still gives the typical mass suppression through the same relation $m_\nu \simeq Y_\Sigma^T\frac{v^2}{M_\Sigma}Y_\Sigma$.

All three types of Seesaw require neutrinos to be Majorana[8] and lead to the same relation for the mass (Eq. 1.31). The distinguishing feature among them is the nature of the heavy fields exchanged in the interaction, as shown in Fig. 1.5.

[8] In the SM instead, there are no gauge singlet or triplet Higgs scalars, so Majorana masses cannot be generated [41].

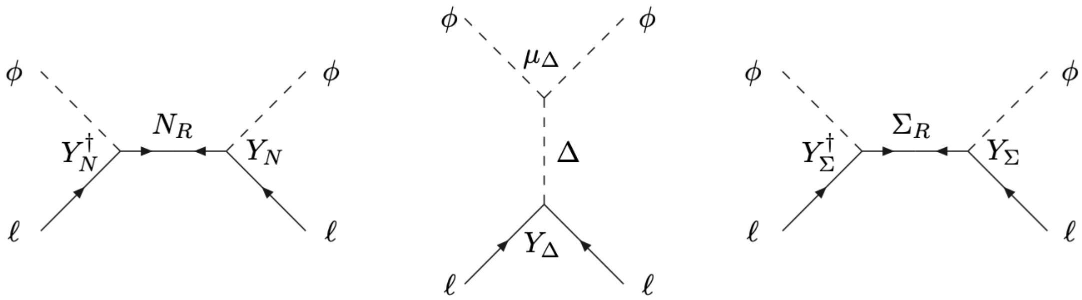

Figure 1.5: Seesaw models: Type-I Seesaw (left), exchanging SM singlet fermions N_R; Type-II Seesaw (centre), exchanging SM triplet scalars Δ; and Type-III Seesaw (right), exchanging SM triplet fermions Σ_R. The Ys are Yukawa couplings and μ_Δ is the coupling between the scalar triplet and the Higgs doublet ϕ.

1.9 Left-Right Symmetric Models

An appealing model from an experimental point of view, leading to a very rich collider phenomenology, greatly enhanced by the prediction of additional heavy states and new interaction channels, is the LRSM. This was motivated by the experimental observation of parity violation by weak interactions, to search for a higher symmetry in which parity is conserved at high energy scales and later broken spontaneously [42]. In this framework, parity violation can emerge as a low-energy consequence of the symmetry breaking, rather than a fundamental assumption, like in the SM.

The first formulation for a LRSM came in 1970 from Salam, Mohapatra and Pati, later extended by Senjanović [36]. In its minimal realisation, LRSM extends the EW sector of the SM by introducing a local $\mathrm{SU(2)_R}$ symmetry, which leads to a gauge structure of the kind:

$$\mathrm{SU(3)_C \times SU(2)_L \times SU(2)_R \times U(1)_{B\text{-}L}} \tag{1.32}$$

where B and L are baryon and lepton numbers, respectively. The LRSM predicts the existence of heavy RH-neutrinos, RH-counterparts of the W and Z bosons and minimal Higgs fields needed for symmetry breaking. Moreover, both Dirac and Majorana mass terms arise naturally.

1.9.1 Scalar sector

In its minimal realisation, the LRSM scalar sector [43] contains a bi-doublet Φ and two scalar triplets $\Delta_{R,L}$

$$\Phi = \begin{pmatrix} \phi_1^0 & \phi_2^+ \\ \phi_1^- & \phi_2^0 \end{pmatrix} \quad , \quad \Delta_{R,L} = \begin{pmatrix} \Delta^+/\sqrt{2} & \Delta^{++} \\ \Delta^0 & -\Delta^+/\sqrt{2} \end{pmatrix} \tag{1.33}$$

whose neutral components acquire VEVs. The scale of the LR-symmetry breaking is set by $\langle \Delta_R^0 \rangle = v_R$, while the EWSSB is given by $\langle \phi_1^0 \rangle = v$.

Expanding the scalar potential around the minimum, a 2×2 mass matrix for the neutral scalars is obtained. Its diagonalisation gives the two physical mass eigenstates: the SM-like Higgs boson H with mass $m_H^2 \simeq 4\lambda v^2 - \alpha^2 v^2/\rho$ and the heavier LRSM neutral scalar Δ with mass $m_\Delta^2 \simeq 4\rho v_R^2$ where α and ρ are the quartic couplings in the scalar potential.

The two states mix with a mixing angle

$$\theta \simeq \frac{\alpha}{2\rho}\frac{v}{v_R} \tag{1.34}$$

that is estimated to be around $\sin\theta < 0.44$ at 2σ CL, for $m_\Delta < 200\,\mathrm{GeV}$. The Majorana masses for heavy-neutrinos and for the W_R boson instead, arise from the Yukawa term

$$\mathcal{L} = Y_N L_R^T \Delta_R L_R + h.c. \tag{1.35}$$

that gives

$$M_N = 2Y_N v_R \quad , \quad M_{W_R} = g v_R \tag{1.36}$$

where g stands for the gauge coupling of the new $\mathrm{SU}(2)_{\mathrm{L,R}}$, both strictly related to the scale of LR-symmetry breaking.

1.10 LRSM-allowed phenomenology

Although the scale of LR-symmetry breaking is not fixed by the theory, LRSMs become testable at LHC, if the mass of the RH charged gauge boson W_R lies in the TeV range [44]. In the minimal LRSM, both the SM and the RH heavy-neutrinos are Majorana particles. This feature allows for lepton-number-violating processes such as the Keung–Senjanović (KS) process. The Majorana or Dirac nature of RH-neutrinos can be experimentally probed by analysing the electric charges of the final-state leptons. Specifically, if neutrinos are Dirac particles, the decay produces only Opposite Sign (OS) dileptons, while if they are Majorana, their decay leads to a mixture of Same Sign (SS) and OS dileptons, with approximately equal probabilities (50% OS - 50% SS).

1.10.1 Keung-Senjanovic process

The KS process represents the golden channel for probing LRSM, as it leads to very clear and distinctive final state, containing two charged leptons and two jets

$$pp \to W_R^{(*)} \to lN \to lljj \tag{1.37}$$

Experimentally, there are two cases that can be distinguished, depending on the mass hierarchy between the RH gauge boson and the heavy-neutrino:

- If $m_{W_R} > m_{N_R}$ (Fig. 1.6, a): the W_R is produced on-shell and its mass can be reconstructed from the invariant mass of the $lljj$ system;
- If $m_{W_R} < m_{N_R}$ (Fig. 1.6, b): the W_R is produced off-shell and the on-shell heavy-neutrino N_R decays into a charged lepton and an on-shell W_R. In this case, the W_R mass can be reconstructed from the invariant mass of the jj system.

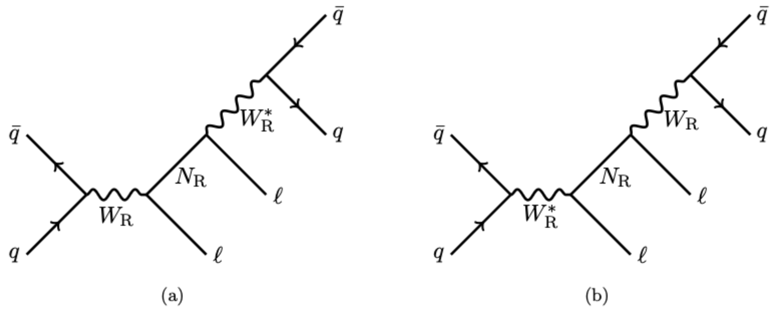

Figure 1.6: KS process: two cases with $m_{W_R} > m_{N_R}$ (a) and $m_{W_R} < m_{N_R}$ (b). The quarks in the final state then hadronize into jets [45].

The $lljj$ final state in the electron and muon channels, has been studied extensively by both ATLAS and CMS collaborations, using data collected at $\sqrt{s} = 7, 8$ and 13 TeV [46, 47, 48, 49]. In these analysis, no evidence for a W_R boson or a N_R neutrino was observed, therefore upper limits were set on m_{W_R} and m_{N_R}.

1.10.2 Lepton-number-violating Higgs decay

A fundamental feature of LRSM is the spontaneous origin of the heavy RH-neutrinos, which follows from the breaking of $\mathrm{SU}(2)_\mathrm{R} \times \mathrm{U}(1)_\mathrm{B\text{-}L}$ symmetry by the triplet Δ_R. This can be seen as analogue to what happens in Higgs mechanism for charged fermions

$$\Gamma_{\Delta \to NN} \propto m_N^2 \quad \text{and} \quad \Gamma_{h \to f\bar{f}} \propto m_f^2 \tag{1.38}$$

and suggests that lepton-number-violating decays of the Δ can directly probe the origin of heavy-neutrino masses, in the same way in which SM Higgs decays can test the origin of charged fermion masses [44].

For this reason, the LRSM channel studied in this thesis is

$$gg \to h/\Delta \to NN \to 2l^{\pm}4j \tag{1.39}$$

proposed in [43, 50], with the corresponding Feynman diagram reported in Fig. 1.7.

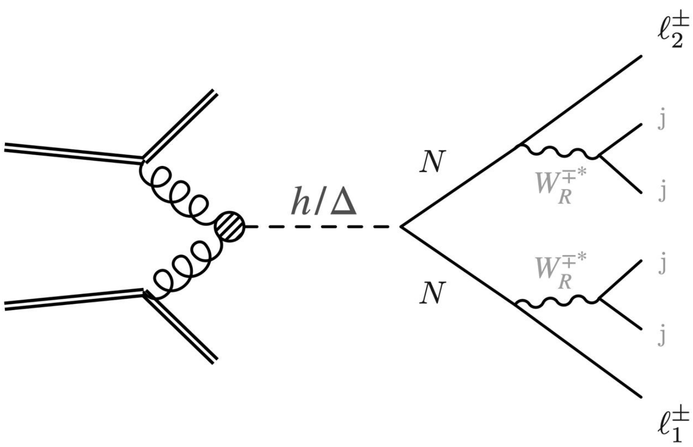

Figure 1.7: Feynman diagram for LRSM heavy-neutrino pair production via Δ resonance after gluon-gluon fusion, yielding a final state with SS or OS lepton pair and multi-jets [50].

The SM Higgs (h), produced via gluon-gluon fusion, mixes with a neutral scalar from the LRSM (Δ), which consequently decays into a pair of heavy RH Majorana neutrinos (N). Each N, subsequently decays into a charged lepton ($l^{\pm}$) and two jets, from the hadronic decay of an off-shell W_R. Since the neutrinos involved in this process are Majorana, it is expected a LNV in 50% of the events, producing a very peculiar SS dilepton final state together with four jets and no missing energy.

This process can happen since the SM Higgs can mix with the triplet that breaks spontaneously LR symmetry (Sec. 1.9.1). In this way, h can decay into a pair of heavy-neutrinos $h \to NN$, with a decay rate normalised to the dominant $h \to b\bar{b}$ channel, expressed as

$$\frac{\Gamma_{NN}}{\Gamma_{b\bar{b}}} \simeq \frac{\tan\theta^2}{3}\left(\frac{m_N}{m_b}\right)^2\left(\frac{M_W}{M_{W_R}}\right)^2\left(1-\frac{4m_N^2}{m_h^2}\right)^{\frac{3}{2}} \tag{1.40}$$

that is enhanced by a factor 2-3 based on the Δ mass (Fig. 1.8), if also QCD and NLO (Next to Leading Order) corrections [51] are taken into consideration.

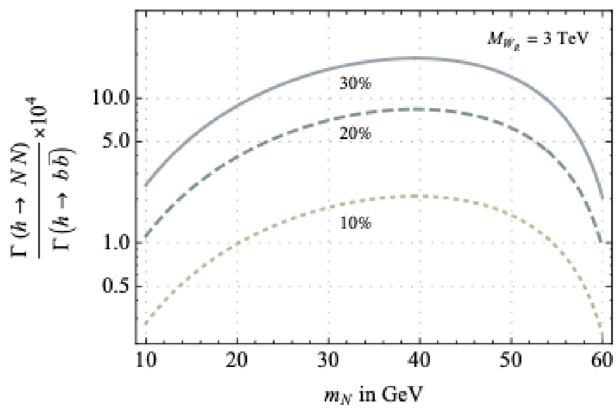

Figure 1.8: Decay rate for the SM Higgs decay into a pair of heavy-neutrinos ($h \to NN$) normalised to the dominant process $h \to b\bar{b}$. The 10%, 20% and 30% labels are different values of the Higgs–triplet mixing angle, specifically, they represent $\sin\theta = 0.1, 0.2, 0.3$ [43].

For the process to be experimentally accessible, the production cross-section for $gg \to \Delta$ (Fig. 1.9, left), as well as the Branching Ratio (BR) for the $\Delta \to NN$ must be appreciable (Fig. 1.9, right). This last condition is satisfied as long as $2m_N < M_\Delta$ and $m_N < m_{VV}$, i.e. below the threshold for decay into gauge boson pairs, where the NN final state dominates. For what concern the production cross-section instead, this decreases rapidly with increasing m_Δ but remains sizeable for $m_\Delta \simeq 100\,\text{GeV}$.

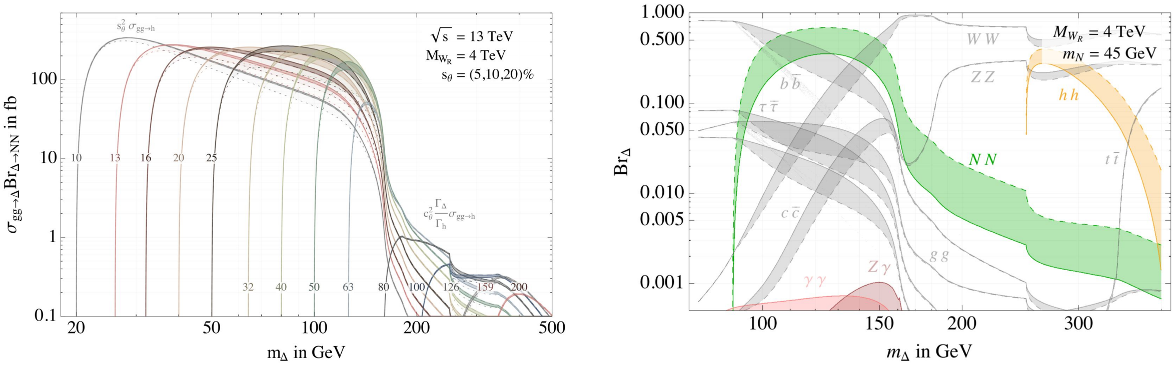

Figure 1.9: Left: production cross-section $\sigma_{gg\to\Delta} \cdot \mathrm{BR}(\Delta \longrightarrow NN)$ as a function of m_Δ, at $\sqrt{s} = 13\,\mathrm{TeV}$ with $M_{W_R} = 4\,\mathrm{TeV}$ and scalar mixing angle $\sin\theta_0 \equiv s_\theta = (5, 10, 20)\%$. Each curve corresponds to a different value of m_N. Right: branching ratios for neutral scalar Δ decays as a function of its mass m_Δ, for fixed $M_{W_R} = 4\,\mathrm{TeV}$ and $m_N = 45\,\mathrm{GeV}$. The decay channels into SM particles ($b\bar{b}$, $\tau\bar{\tau}$, WW, ZZ, gg, $\gamma\gamma$, $Z\gamma$, hh, $t\bar{t}$, $c\bar{c}$) are shown in grey, while the $\Delta \longrightarrow NN$ channel is highlighted in green. The coloured bands correspond to the uncertainty on the scalar mixing angle $\sin\theta$. The $\Delta \longrightarrow NN$ branching ratio is dominant in the intermediate mass range at approximately $110 - 280\,\mathrm{GeV}$ [50].

An additional distinctive feature of LRSM neutrinos, is also given by their long decay lengths, which for low N mass can be written as

$$(c\tau_N^0)^{-1} \simeq \frac{G_F^2 m_N^5}{16\pi^3} \left(\frac{M_W}{M_{W_R}}\right)^4 \tag{1.41}$$

This can vary from millimeter (prompt signatures) to several meters (displaced vertices). In this framework, the transverse displacement l (Fig. 1.10) is useful to distinguish between these scenarios: specifically, for $m_{W_R} = 4\,\mathrm{TeV}$ the signal is predominantly prompt.

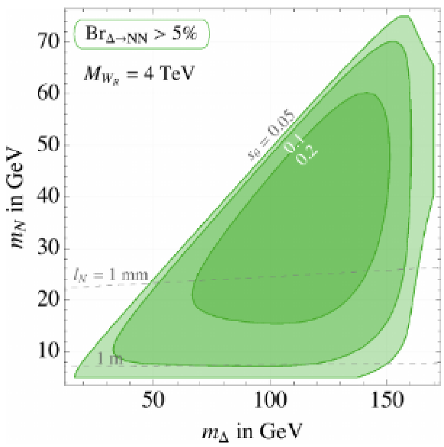

Figure 1.10: Parameter space in the (m_Δ, m_N) plane where $\mathrm{BR}(\Delta \longrightarrow NN) > 5\%$, for $M_{W_R} = 4\,\mathrm{TeV}$ and three values of the scalar mixing angle $s\theta_0 = 0.05,\ 0.1,\ 0.2$. Dashed lines indicate fixed values of the heavy-neutrino decay length in the lab frame, $l_N = 1\mathrm{mm}$ and $l_N = 1\mathrm{m}$ [50].

Two final remarks can be made regarding this process. First, to provide a concrete theoretical estimate, for a 13 TeV run at LHC with 100 fb^{-1} luminosity, considering a mixing angle $\theta \simeq 10\%$ and $m_N = 40$ GeV, together with the known cross section $\sigma(gg \to h) = 43.9$ pb and $\mathrm{BR}(b\bar{b}) = 57\%$, 500 events of $h \to NN$ are expected [43].

Second, this channel is complementary to the traditional neutrinoless double beta decay ($0\nu2\beta$) which is usually considered for BSM neutrino studies [52], with the (crucial) difference that while $0\nu2\beta$ can probe LNV at low energies, $h \to NN \to 2l^{\pm}4j$ can be studied at LHC energies.

1.10.3 Searches at colliders

For LRSM, KS process [53] signatures have been searched for by ATLAS and CMS, using data at $\sqrt{s} = 7$, 8 and 13 TeV [46, 47, 48, 49]. CMS has extended the search to hadronic $\tau\tau jj$ final states [54, 55] and to N production from Z_R decays [56].

The channel studied in this thesis has never been searched for at any collider. It probes the LRSM scalar sector through Δ_R^0 and is complementary to the KS process, since it is specifically optimised for $m_N \lesssim 100$ GeV, where the KS process loses sensitivity.

In the future, the High-Luminosity LHC (HL-LHC), expected to collect a total integrated luminosity of 3 ab^{-1} at $\sqrt{s} = 14$ TeV, will extend the sensitivity of all the searches described above [57].

Beyond the LHC, the Future Circular Collider (FCC) programme at CERN represents a step forward in the exploration of the LRSM parameter space [58]. The first stage, FCC-ee, will operate as an electron-positron collider at centre-of-mass energies ranging from the Z peak ($\sqrt{s} \simeq 91$ GeV) to above the WW threshold, producing approximately 10^{13} Z bosons. Displaced-vertex searches at the Z peak will provide the strongest sensitivity in the low-mass regime, probing total light-heavy-neutrino mixing parameters down to $|\theta|^2 \simeq 10^{-11}$ for $m_N < 100$ GeV [59], several orders of magnitude beyond current limits.

The second stage, FCC-hh, will operate as a proton-proton collider at $\sqrt{s} = 100$ TeV with a target integrated luminosity of 20 ab^{-1}. In the LRSM framework, the extended centre-of-mass energy will push the direct reach on the W_R mass well beyond the LHC limits, while for $m_N > 200$ GeV, lepton-flavour-violating dilepton-dijet final states will probe light-heavy-neutrino mixings down to approximately 10^{-5}. For $m_N < 100$ GeV, displaced-vertex searches will reach $|V_{\alpha N}|^2 \simeq 10^{-11}$, an improvement of six orders of magnitude with respect to current bounds [58, 60]. The process studied in this thesis will also benefit from the FCC-hh environment, thanks to the much larger gluon-gluon fusion cross-section at 100 TeV and to the increased luminosity, that will provide event yields several orders of magnitude larger than at the LHC.

Finally, FCC-eh, combining a 60 GeV electron beam with the 50 TeV FCC-hh proton beam at $\sqrt{s} \simeq 3.5$ TeV, will offer a cleaner environment than pure proton-proton collisions.

The complementarity between FCC-ee, FCC-hh and FCC-eh will enable a comprehensive scan of the LRSM parameter space across many orders of magnitude in both mass and coupling, with the potential to either discover or conclusively exclude a large fraction of the theoretically motivated parameter space.

Chapter 2

The ATLAS Experiment at LHC

The Large Hadron Collider at CERN (Conseil Européen pour la Recherche Nucléaire), is the world's most powerful particle accelerator and collider. It was built to address some of the most challenging, unanswered questions in particle physics and since becoming operational, it has delivered an unprecedented amount of data, enabling major progress in high-energy physics research.

In this chapter, the experimental foundations for the analyses presented in this thesis are given. As a first thing, a description of the LHC, its operating principles and the key parameters that characterise its performance are considered. Then, a detailed description of the ATLAS (A Toroidal LHC ApparatuS) detector is done, considering each of its subsystems and the roles they play in reconstructing the products of high-energy proton-proton (pp) collisions.

2.1 The Large Hadron Collider

The LHC is located underground, near Geneva, Switzerland, in the tunnels that once hosted the Large Electron-Positron Collider (LEP) [61]. The main ring has a circular shape (26.7 km in circumference [62]) and particles (both protons and heavy ions) can circulate and collide inside of it, after being accelerated up to energies of the TeV scale.

Its construction was completed in 2008, it entered physics operations in 2010 and then, went through different running periods: **Run 1** (2010–2013), colliding protons at beam energies of 3.5 – 4 TeV [63], corresponding to centre-of-mass energies of $\sqrt{s}$ = 7 TeV and $\sqrt{s}$ = 8 TeV, **Run 2** (2015-2018), operating with protons at beam energies of 6.5 TeV [64], corresponding to centre-of-mass energies of $\sqrt{s}$ = 13 TeV and **Run 3** (from 2022 until June 2026), exploiting a beam energy of 6.8 TeV [65], corresponding to centre-of-mass energies of $\sqrt{s}$ = 13.5 TeV. Each LHC Run was followed by a **Long Shutdown** period, Long Shutdown 1, 2 and 3 (LS1, LS2, LS3), during which repairs and upgrades to both LHC and experiments were performed. After LS3, the HL-LHC project, expected in the mid-2030s, should become operational.

At the LHC, protons are divided in bunches separated by a bunch spacing of 25 ns (corresponding to a collision frequency of f = 40 MHz), containing about 10^{11} protons each [66]. The injected protons are sent through a series of accelerators before reaching the main ring (Fig. 2.1).

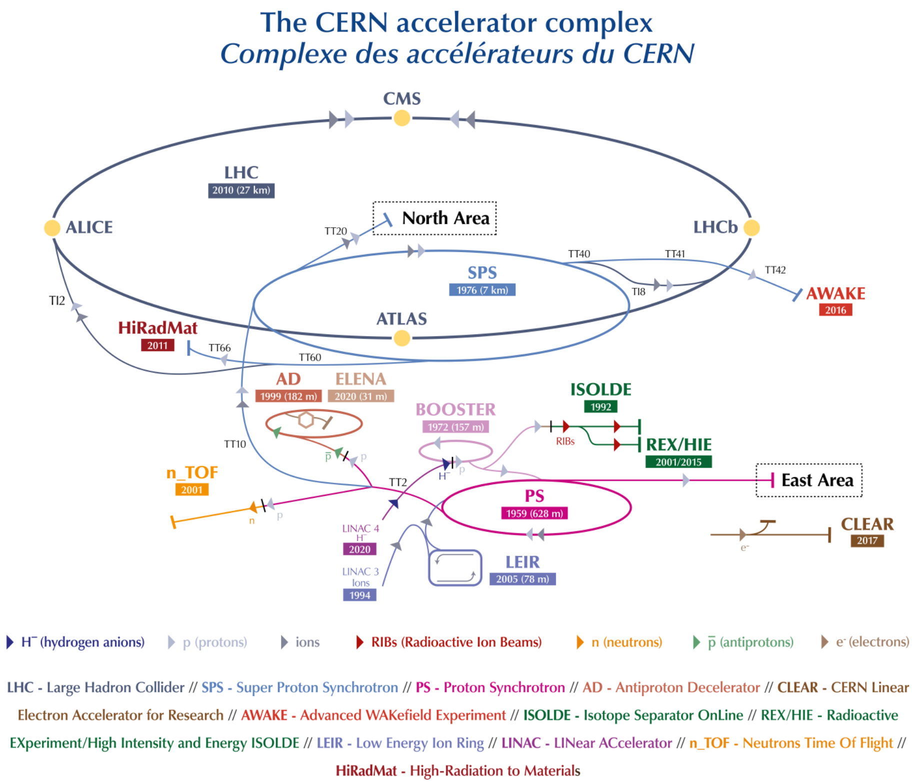

Figure 2.1: LHC chain of acceleration: LHC is the big dark blue ring, anticipated by a chain of particle accelerators. Particles are boosted throughout the chain, before being injected into the main ring, in which they reach the highest achievable energy [67].

The acceleration chain begins when the protons are extracted from hydrogen gas and are subsequently accelerated up to 160 MeV with a linear accelerator, LINAC 4 (since 2020), that prepares them to enter the Proton Synchrotron Booster (BOOSTER) circular accelerator. In here, they reach an energy of 2 GeV and are focused, through a magnet deflector, directly into the Proton Synchrotron (PS), the oldest synchrotron circular accelerator at CERN, and into the Super Proton Synchrotron (SPS), afterwards. The SPS represents the final stage of the injection chain, in which protons are accelerated up to 450 GeV. After that, the beams enter the LHC, one circulating clockwise and the other anti-clockwise, and after approximately 20 minutes, each beam reaches the final energy of 6.5 TeV. Notice that, at LHC both protons and ions can be collided, however ions follow a slightly different path with respect to protons.

At this point, when the proton bunches reach the highest achievable energy, the two beams are squeezed using magnets and can collide at the four Interaction Points (IPs), where the four main LHC experiments are located:

- **ALICE** [68] (A Large Ion Collider Experiment): dedicated to heavy-ion physics, mainly focusing on Pb-Pb collisions. It is designed to study the physics of Quark-Gluon Plasma (QGP)[1], produced under controlled conditions;

[1]The QGP is a state of matter which is believed to have filled the Universe shortly after the Big Bang, in which quarks and gluons are no longer confined but exist in a deconfined, strongly interacting medium.

- **ATLAS** (A Toroidal LHC ApparatuS) and **CMS** [69] (Compact Muon Solenoid): nearly hermetic, general-purpose experiments that share very similar physics programs, but with some differences in the designs and magnetic systems;
- **LHCb** [70] (Large Hadron Collider beauty): focuses on heavy-flavour physics, which aims to study CP violation and rare decays of beauty and charm hadrons. Differently from ATLAS and CMS, it exploits an asymmetric design to detect mainly forward-produced particles.

2.1.1 Key parameters for collider physics experiments

In particle physics, new physics can be searched for through two complementary strategies: direct observation of new particles, which requires sufficiently high centre-of-mass energy to allow their production, or indirect discovery, which exploits deviations from the predictions of known phenomena. In both cases, high energy and high luminosity are required.

The energy reach of an experiment is usually determined by the design of the experimental system itself: fixed-target experiments, for example, where a single beam is shot at a stationary target, achieve a lower energy compared to collider experiments, where two beams of accelerated particles are brought into collision [4]. In the LHC case, circular collider technology is exploited, enabling for the reach of the highest achievable energy.

Luminosity is used as a unit of measure for the rate of produced events and must be carefully managed, as a too high interaction rate can introduce complications such as a too high pile-up. However, the higher the luminosity, and the longer the machine can run, the more data can be acquired.

Overall, the physics potential of a collider experiment is shaped by a set of important parameters that take into consideration energy reach, beam conditions and detector response, with centre-of-mass energy and luminosity representing the two most critical quantities.

Centre-of-mass energy

In colliders, the centre-of-mass energy $\sqrt{s}$ is a fundamental quantity which fixes the maximum invariant mass that can be produced in a collision, thus defining the mass reach for new particles. In the case of two beams colliding with beam energies E_1 and E_2, the Lorentz-invariant quantity $s = E_1 + E_2$, for example.

In pp collisions, since protons are composite objects made of partons (gluons and quarks), another relevant quantity is the partonic centre-of-mass energy $\hat{s}$. Each parton carries a fraction x of the proton's momentum and the energy associated to each parton is

$$\hat{s} = x_1 x_2 s \tag{2.1}$$

where x_1 and x_2 are the momentum fractions of the two interacting partons. The probability to find a parton carrying that specific fraction of momentum in the colliding protons is given by Parton Distribution Functions (PDFs).

Luminosity

The luminosity is also a fundamental parameter of a collider and is usually measured in units of inverse barns (b^{-1}), where $1\,\mathrm{b} = 10^{-28}\,\mathrm{m}^2$. Luminosity needs to be distinguished between

Instantaneous Luminosity ($\mathcal{L}$), associated to the event rate and *Integrated Luminosity* (L), related to the total number of events which occurred. For a certain process with cross section σ, the event rate is

$$\frac{dN}{dt} = \mathcal{L} \cdot \sigma. \tag{2.2}$$

where the instantaneous luminosity can be expressed, assuming a Gaussian profile of the beams and head-on collisions, as a function of different beam parameters

$$\mathcal{L} = \frac{N^2\, n_b\, f_{\rm rev}\, \gamma}{4\pi\, \varepsilon_n\, \beta^*} F, \tag{2.3}$$

where N is the number of protons per bunch, n_b is the number of bunches per beam, $f_{\rm rev}$ is the revolution frequency, ε_n is the normalised transverse beam emittance, β^* is the size of the beam at the interaction point, the Lorentz factor γ is related to the fact that $\mathcal{L}$ increases with beam energy and finally F is a geometric factor accounting for the luminosity reduction due to the crossing angle and the bunch length. Real parameters for LHC are $N \simeq 1.1 - 2.3 \times 10^{11}$, n_b up to 2808, $f_{\rm rev} \simeq 11.245\,\text{kHz}$, $\varepsilon_n \simeq 1.0 - 3.75\,\mu\text{m}$, β^* can vary from some cm to km and $F \simeq 0.3 - 1$.
Given $\mathcal{L}$, the integrated luminosity can be computed by integrating over time

$$L = \int \mathcal{L}\, dt \tag{2.4}$$

In Run 2 of the LHC, for example, the ATLAS experiment collected an integrated luminosity (Fig. 2.2) of approximately $L \simeq 140\,\text{fb}^{-1}$ at $\sqrt{s} = 13\,\text{TeV}$, providing a huge statistical sample for precision measurements and searches for rare processes.

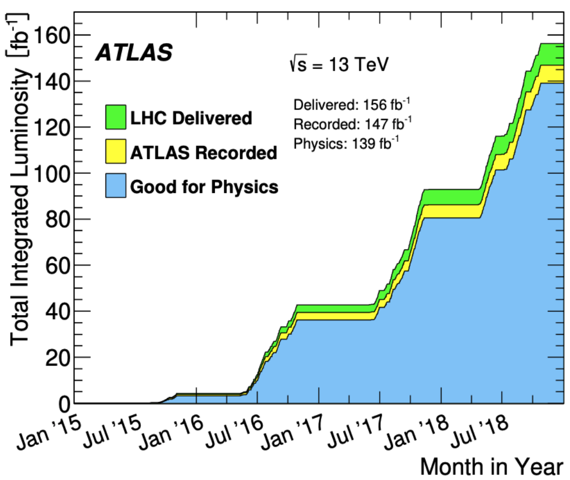

Figure 2.2: Integrated luminosity recorded (yellow area) and delivered (green area) by ATLAS detector in Run 2 (2015-2018) during pp collision data-taking at $\sqrt{s} = 13\,\text{TeV}$. The cumulative integrated luminosity certified for physics analysis for ATLAS experiment is also shown (light blue area) [71].

Pile-up

Luminosity is related to a phenomenon known as pile-up (μ) which represents the number of simultaneous interactions per bunch crossing. A high value of μ ($\mu \gg 60$) can degrade the performance of the ATLAS sub-detectors and affect the precision of the object reconstruction algorithms. For this reason, different complex techniques are used during particle reconstruction to reduce these effects, both in data and Monte Carlo simulation.

LHC operations achieved an instantaneous luminosity of $\mathcal{L} \simeq 2.0 \times 10^{34}\,\mathrm{cm}^{-2}\,\mathrm{s}^{-1}$ [72] so, in this framework, each bunch crossing produced not one but many pp interactions simultaneously, leading to overlapping signals in addition to the initial collision of interest. The average pile-up can be expressed as

$$\langle\mu\rangle = \mathcal{L}\frac{\sigma_{pp}}{f_{\mathrm{rev}}\, n_b} \tag{2.5}$$

where $\sigma_{pp} \simeq 80\,\mathrm{mb}$ is the inelastic pp cross-section. During Run 2, ATLAS acquired data at $\langle\mu\rangle \simeq 30$, which was then increased to $\langle\mu\rangle \simeq 60$ in Run 3.

2.2 The ATLAS Experiment

ATLAS (Fig. 2.3) is a multi-purpose detector [73], placed approximately 100 m underground at Point-1 of the LHC ring.

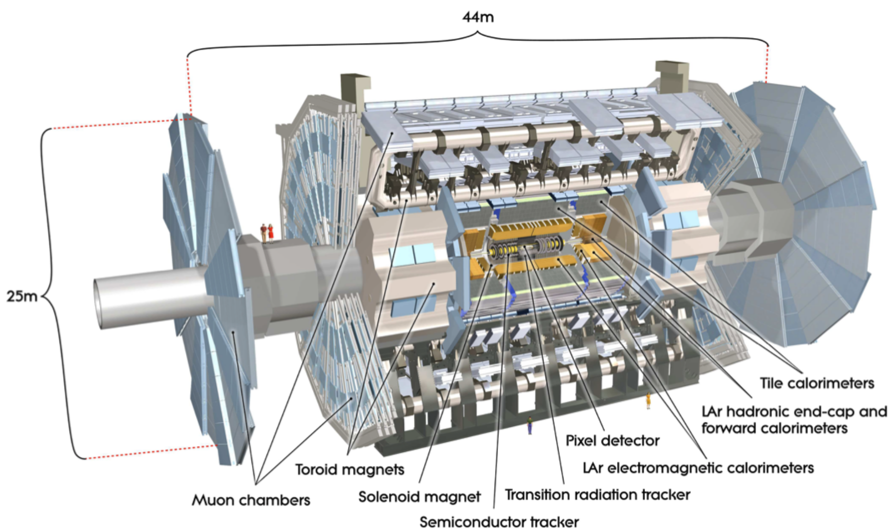

Figure 2.3: ATLAS detector, cut-away view [73]: the detector is 25 m in height and 44 m in length, weighting approximately 7000 tonnes.

It has a cylindrical geometry (25 m high and 44 m long), providing an almost full 4π angular coverage for particles produced in LHC collisions. Its coordinate system (Fig. 2.4) is defined by placing the z-axis along the beam pipe, the x-axis pointing towards the centre of the LHC ring and the y-axis pointing upward. The $x - y$ plane is known as the transverse plane (to the z-axis).

In this system, the azimuthal angle $\phi = \arctan(\frac{y}{x})$ $(0 < \phi < 2\pi)$ is measured around the beam axis (Fig. 2.4) and the polar angle $\theta = \arctan\left(\frac{\sqrt{x^2+y^2}}{z}\right)$ $(0 < \theta < \pi)$ is measured from the positive z-axis (Fig. 2.5). Given this, $\theta = 0$ corresponds to the motion along $+z$-axis and $\theta = \pi$ corresponds to the motion along $-z$-axis. A very useful quantity which is computed usually is the pseudorapidity $\eta = -\ln\tan(\frac{\theta}{2})$, preferred over polar angle since differences in η are Lorentz-invariant under boosts along the beam axis and most physics objects are distributed approximately uniformly in η.

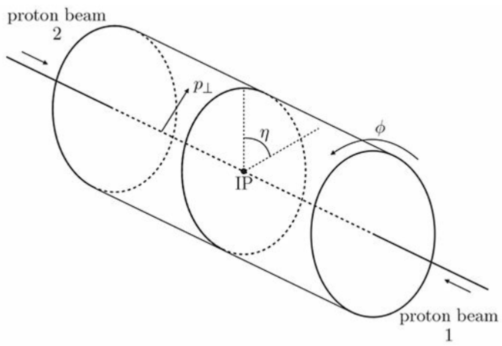

Figure 2.4: Schematic illustration of ATLAS coordinate system, to first approximation: the collision point of the two beams 1 and 2 is denoted as IP and azimuthal angle ϕ, pseudorapidity η and transverse momentum $p_\perp$ are highlighted [66].

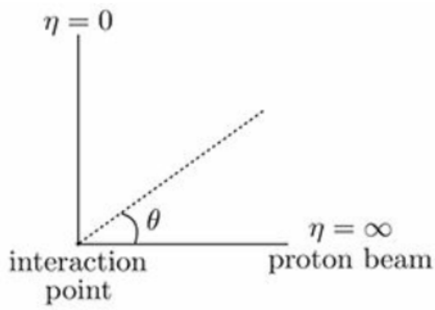

Figure 2.5: Illustration of the polar angle in relation with η: $\eta = 0$ for central collisions, perpendicular to the beam at the IP and $\eta = \pm\infty$ along the proton beams where $\theta = 0, \pm\pi$ [66].

The ATLAS detector can be divided into three main parts:

- **Inner Detector**: for charged-particles tracking (Sec. 2.2.2);
- **Calorimeters**: for energy measurements (Sec. 2.2.3);
- **Muon System**: for muon tracking (Sec. 2.2.4).

During LS3, the ATLAS detector will be upgraded for HL-LHC and the major upgrades will involve a new Inner Detector (ITk) made of all silicon, up to $|\eta| = 4$, to face the tougher radiation environment and the higher $\mu \simeq 140$. Other upgrades will involve muon chambers, trigger and Data Acquisition systems and new electronics [74].

2.2.1 ATLAS Magnetic System

The subsystems mentioned above are embedded into two magnetic field systems:

- **Central Solenoid**: is a thin superconducting solenoid, 5.8 m long and 2.46 m in diameter, providing a 2 T axial field inside the Inner Detoector;
- Toroidal magnetic system: composed of a **Barrel Toroid**, made of eight superconducting coils arranged symmetrically around the beam axis, providing a field of approximately 0.5 – 1 T in the barrel muon region and two smaller **Endcap Toroids** at each end of the barrel, providing the field for the endcap muon spectrometer.

The presence of a magnetic field is fundamental to obtain particles' charge and momentum information, using

$$\rho = \frac{|\vec{p}|}{q|\vec{B}|} \tag{2.6}$$

Where ρ is the curvature radius, q is the charge, p is the momentum and B is the magnetic field.

2.2.2 Inner Detector

The Inner Detector (ID) (Fig. 2.6) is the main tracking device in ATLAS and also the closest to the IP. It is immersed in a 2 T magnetic field, produced by the central solenoid which bends the trajectories of charged particles in the transverse plane. Thanks to this characteristic, by measuring the curvature of each track, the transverse momentum p_T and the charge sign of particles can be determined, using (Eq. 2.6). The ID covers the pseudorapidity range $|\eta| < 2.5$ and is designed to provide excellent spatial resolution using fine granularity subdetectors, enabling the reconstruction of primary and secondary vertices. Specifically, the ID is composed of three sub-detectors: the high-resolution silicon Pixel detector, the Semiconductor Tracker (SCT) [75] and the Transition Radiation Tracker (TRT) [76].

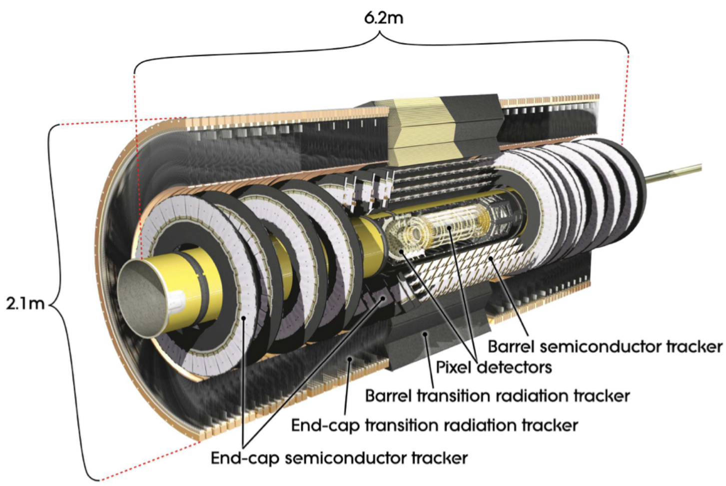

Figure 2.6: ATLAS ID: composed by the silicon Pixel detector, the Semiconductor Trackers and the Transition Radiation Tracker. Provides a really high-precision charged-particle track reconstruction [73].

Pixel Detector

The Pixel Detector is the innermost component of the ID. Among the ID-sub-systems it has the highest granularity and thus the highest precision for the interaction vertex reconstruction. It consists of multiple concentric cylindrical layers in the barrel region and disk-shaped layers in the endcaps.

The innermost layer is called Insertable B-Layer (IBL) [77] and was added during LS1. It is located at a radius of 33.25 mm from the beam axis and uses a new generation of silicon pixel sensors, which improve the impact parameter resolution, consequently improving secondary vertices identification. The other three layers of this detector are more distant from the beam line, respectively at radii of approximately 50.5 mm, 88.5 mm and 122.5 mm.

Overall, the Pixel Detector contains 92 million readout channels, providing a very fine granularity needed to separate tracks in the dense environment of LHC collisions.

Semiconductor Tracker

The SCT is a silicon micro-strips tracking detector that is extended in the region between approximately 30 cm and 52 cm from the beam axis. It is composed of four cylindrical barrel layers and two endcaps composed of nine disks each [75] and was designed to provide precise tracking information. In the barrel region, each track crosses eight strips layers (corresponding to four space-points) with the strips placed at a distance of 80 μm (between the centres of adjacent strips), resulting in a spatial resolution of approximately 17 μm in the transverse plane and 580 μm in the longitudinal one. In total, the SCT consists of about 6.3 million readout channels.

Transition Radiation Tracker

The TRT is the outermost component of the ID and differently from the other two detection systems, it is made of several layers of gaseous straw tubes. These are filled with a Xe-based gas mixture, specifically 70% Xe, 27% CO_2, 3% O_2, and are placed parallel to the beam axis in the barrel region, while in the end-cap region they are arranged radially in wheels. This detector has two main objectives: to provide a large number of additional track-position measurements, approximately 36 per track, improving the overall track momentum resolution (it provides only transversal plane spatial information, with an intrinsic accuracy of 130 μm per straw) and to detect *Transition Radiation*[2]. The intensity of this type of radiation is related to the Lorentz factor γ of the particle: a larger emission is therefore expected for light particles (like electrons) than for heavier ones (like pions), assuming the same momentum. In this way, it is possible to perform a very effective electron identification.

2.2.3 Calorimeters: ECAL and HCAL

The calorimeter system (Fig. 2.7) surrounds the ID covering the pseudorapidity range $|\eta| < 4.9$ and is able to perform energy and position measurements for electrons, photons and

[2]Transition Radiation is emitted when relativistic charged particles cross interfaces between two materials which have different dielectric constants.

hadrons, by inducing and measuring electromagnetic[3] (EM) or hadronic[4] showers. To make sure to have a sufficient containment of showers and to minimize the punch-through into the muon system, calorimeters need to be sufficiently thick in terms of radiation lengths (X_0 for EM showers and λ for hadronic ones).

Two different types of calorimeters can be distinguished: the Electromagnetic CALorimeter (ECAL) [79], which has a very fine granularity and is able to perform precise measurements of the EM showers energy and position, and the Hadronic CALorimeter (HCAL) [79], which instead has a coarser granularity and it is used mainly for jet reconstruction and Missing Transverse Energy (MET) measurements.

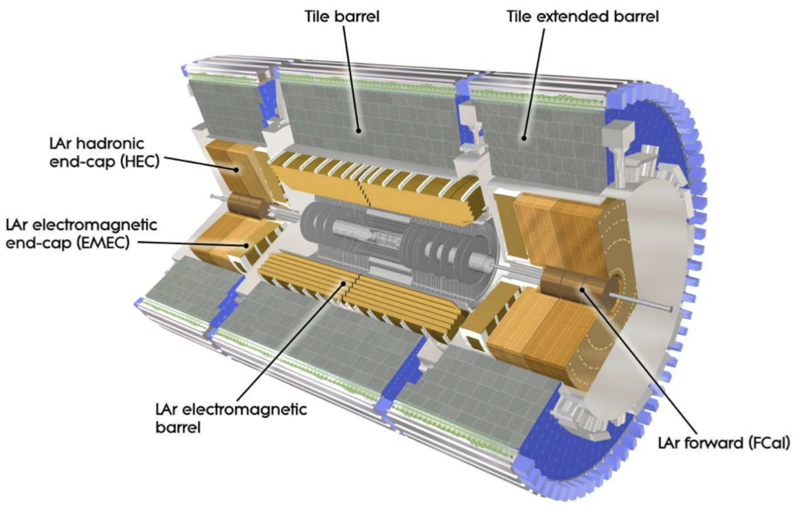

Figure 2.7: ATLAS calorimeters: the two Electromagnetic and Hadronic calorimeters, respectively segmented in different sub-detectors, can be recognized [73].

Electromagnetic Calorimeter (ECAL)

Is a Lead-Liquid-Argon (LAr) sampling calorimeter that is divided into a barrel component, covering $|\eta| < 1.475$ and two endcap components covering $1.375 < |\eta| < 3.2$. It has a total thickness in the barrel of more than 22 X_0 and of more than 24 X_0 in the endcaps, resulting in a full containment of electromagnetic showers up to some TeV. Its working principle is that when a charged particle passes through the LAr (kept at cryogenic temperature of 88 K using large cryostats), it ionises the medium and the resulting ionisation current is collected on the electrodes.

The ECAL is segmented into three longitudinal layers:

- **Layer 1**: has a very fine segmentation in η ($\Delta\eta = 0.003$), which enables precise measurements of shower width and good discrimination between photons and π^0 decays;

[3]Electromagnetic showers are cascades of secondary photons, electrons and positrons produced through Bremsstrahlung and pair production, after the interaction of primary photons, electrons or positrons with matter [78].

[4]Hadronic showers are cascades of secondary hadrons, initiated when a primary hadron undergoes nuclear interactions in a dense material [78].

- **Layer 2**: is the main sampling layer and contains most of the shower energy;
- **Layer 3**: has a less fine segmentation and is used to measure the tails of the showers to correct energy leakage.

The energy resolution can be parametrised as [80]

$$\frac{\sigma_E}{E} = \frac{a}{\sqrt{E}} \oplus \frac{b}{E} \oplus c, \tag{2.7}$$

where a is the stochastic term related to shower fluctuations, b is the noise term and c is the constant term. The numerical values for the coefficients are derived from test-beam measurements and detector performance studies.

Hadronic Calorimeter (HCAL)

It is constructed all around the ECAL and it is designed to contain and measure the energy of hadronic showers. This second calorimeter is composed of three distinct sub-detectors exploiting different technologies:

- **Tile Calorimeter**: is a sampling calorimeter covering the central region $0.8 < |\eta| < 1.7$. It uses steel as the absorber and plastic scintillating tiles as the active medium. Its working principle is that scintillation light is collected by wavelength-shifting fibres and consequently read out by PhotoMultiplier Tubes (PMTs). Overall, it provides a total depth of approximately 7.4 nuclear interaction lengths (λ), resulting in a good containment of hadronic showers;
- **LAr Hadronic Endcap Calorimeter (HEC)**: covers the range $1.5 < |\eta| < 3.2$ and uses copper plates as absorber with LAr as the active medium, sharing cryostats with the ECAL endcaps;
- **LAr Forward Calorimeter (FCal)**: is the closest to the beam axis, where particle fluxes are the highest, and covers the most forward region in the range $3.1 < |\eta| < 4.9$ [81]. It uses copper and tungsten absorbers with LAr as the active medium and provides both electromagnetic and hadronic measurements.

2.2.4 Muon System

Since muons are the only charged particles that can escape the full calorimetric system, a Muon Spectrometer (MS) (Fig. 2.8) is needed to cover the outermost part of ATLAS detector, to identify muons and measure their momenta [82]. It is divided into three regions, one barrel and two endcaps, and it is designed to be sensitive to the range of pseudorapidity $|\eta| < 2.7$ (respectively $|\eta| < 1.2$ for the barrel region and $1 < |\eta| < 2.7$ for the endcaps). To bend muon tracks and recover their momenta, it exploits the toroidal magnetic field provided by three superconducting toroids (one barrel and two endcap toroids).

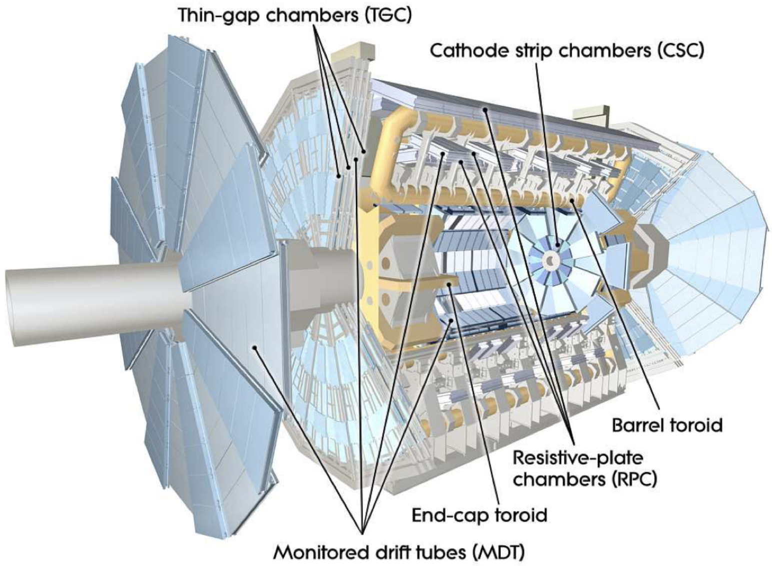

Figure 2.8: ATLAS Muon System: the barrel and endcap toroids, together with the four muon detector technologies can be recognised [73]

The detector technologies used in the MS are of four types:

- **Monitored Drift Tubes (MDTs)**: are aluminium drift tubes with a diameter of 3 cm assembled in multiple layers forming MDT chambers, filled with a gas mixture of 93% Ar and 7% CO_2. These precision tracking devices, covering most of the $|\eta| < 2.7$ range, are able to provide a single-hit resolution of approximately 80 μm;
- **Cathode Strip Chambers** (CSCs): are Multi-Wire Proportional Chambers (MWPCs) with cathodes segmented into strips [73], covering the pseudorapidity range $2.0 < |\eta| < 2.7$, reaching a spatial resolution of the order of 50 μm;
- **Resistive Plate Chambers (RPCs)**: are gaseous detectors used in the barrel region ($|\eta| < 1.05$), able to provide a fast trigger signal for Level-1 muon trigger with a time resolution better than 2 ns;
- **Thin Gap Chambers (TGCs)**: gaseous detectors used in the endcap region ($1.05 < |\eta| < 2.4$), providing fast bunch-crossing identification for the Level-1 muon trigger, as well as a measurement of the muon ϕ coordinate in the non-bending plane;

2.3 Trigger and Data Acquisition (TDAQ)

An important aspect to be considered is that at LHC designed luminosity, *pp* interactions occur at a rate which is much higher with respect to the rate at which events can be fully reconstructed and saved permanently. The Trigger and Data Acquisition (TDAQ) systems (Fig. 2.9) are needed for selecting and managing these huge amount of data.

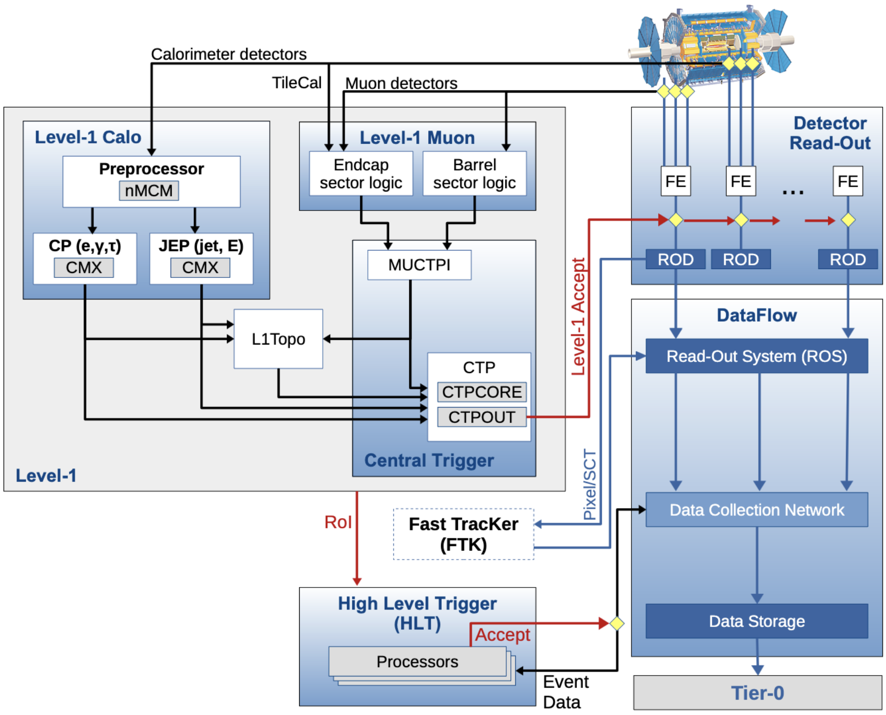

Figure 2.9: ATLAS Trigger and Data Acquisition System in Run 2: the final L1 decision is due to the CTP, combining inputs from the calorimeter and muon trigger systems and is used as the input for the HLT [83].

The Data Acquisition (DAQ) is able to collect data from detector read-out, convert them into digital format and finally record them, for offline analyses.

The Trigger is responsible for real-time selection of all the potentially interesting events (for example high p_T leptons, photons and jets, τ from hadronic decays and large missing transverse energy [84]). The ATLAS trigger system works in two complex stages:

- **Level-1 Trigger (L1)**: is a hardware-based trigger able to reduce the event rate from 40 MHz to approximately 100 kHz within 2.5 μs. The selection is done with dedicated trigger chambers in the barrel (RPC) and end-cap (TGC) regions, for muons, and with reduced-granularity information from the calorimeters, for electrons. What remains from these selections is then processed by the Central Trigger Processor (CTP). After passing this first step, the events are buffered in the Read-Out System (ROS) and then processed by the High Level Trigger;

- **High-Level Trigger (HLT)**: is a computer farm performing software-based event selection, receiving Region-of-Interest (ROI)[5] information from L1 and applying more refined reconstruction algorithms, reducing the rate to approximately 1 kHz.

After the HLT event selection, data are transferred to be stored locally at the experimental site

[5]The Regions of Interest (ROIs) give the η and ϕ coordinates of the interesting event, recorded by the L1 and then are used as the input for the HLT.

and then exported to the Tier-0[6] facility at CERN computing centre, for offline reconstruction [86].

The full set of selection criteria used in a certain data-taking period is organised into the **Trigger Menu**. Each entry in the menu is a **Trigger Chain**, a sequence of L1 seeds and HLT algorithms that must all be satisfied for an event to be recorded, under that particular chain. Chains are designed to target specific physics signatures (for example, a single high-p_T electron, a pair of muons, or large missing transverse energy). Since a given event could satisfy multiple chains simultaneously, the trigger menu is structured with pre-scale factors and logical OR combinations, to balance physics coverage against bandwidth and storage constraints.

This trigger selection is a fundamental step in the research process, as it determines the possibilities and sensitivity of the analyses.

[6]The Tier-0 receives ”raw” data in “byte-stream” format from the TDAQ system and performs fast processing and redistribution of data to Tier-1 centres worldwide [85].

Chapter 3

Probing Neutrino Mass Generation at LHC

This chapter describes the experimental framework underlying the search for LRSM heavy-neutrinos at the ATLAS experiment and is divided in two parts. In the first one, the simulation chain that produces the MC samples used in the analysis is outlined, from matrix element generation and parton showering, through detector simulation (Sec. 3.1), up to the reconstruction of physics objects (Sec. 3.1.1) and the derivation of truth-level DAOD files (Sec. 3.1.2). The ATLAS offline analysis framework is then described (Sec. 3.1.3).

In the second part, the baseline analysis strategy for the $gg \to h/\Delta \to NN \to 2l^{\pm}4j$ process studied in this work is presented (Sec. 3.2), covering trigger selections, object definitions, the definition of signal, control and validation regions, background estimation methods and the statistical procedure used for signal extraction, together with the expected sensitivity of the baseline search that motivates the optimisation work presented in the following chapters.

3.1 Monte Carlo simulation

The production of simulated MC samples follows different steps [87]:

- **Matrix element calculation**: based on QED/QCD calculation, consists of sampling single events from the matrix element of the hard scatter process. This step can be very fast or very time-consuming, depending on the complexity of the calculations required, and produces a list of high-momentum (hard) partons.

- **Parton shower and hadronization**: starting from the partons from the hard scatter, this consists in the calculation of the QCD processes happening at low energy scales, up to hadronization (production of hadrons which do not carry a color charge). The two main phenomenological models used are the Lund string model and the cluster fragmentation model. This step yields a list of particles which have a lifetime sufficiently long to enter into the detector, therefore called *stable*.

- **Detector simulation and pile-up**: consists in the simulation of the interaction of stable particles inside the detector. It is a very complex and computationally-expensive part of the MC and its output is a list of energy deposits in the ATLAS sub-detectors. The detector response needs to be additionally adjusted considering pile-up, so also these interactions are independently simulated;

- **Digitisation**: consists of converting the energy deposits of the simulations found previously into digitised signals, considering also the information from pile-up interactions.

The first two steps of the chain are collectively considered as the *event generation* and produce **truth** files. These files contain the kinematics of all simulated particles as produced by the generator, before any detector simulation or reconstruction is applied. In particular the truth-level information contains the nature, the four-momentum, the production vertex and the daughters of the simulated particles. The term "truth" is used in contrast to "reconstructed", which refers to what the detector would actually measure. The most used generator in this framework is **Pythia8** [88], handling Leading-Order (LO) matrix element calculation, initial- and final-state parton showers, hadronisation (via the Lund string model) and multiple parton interactions. In the case of this work instead, the matrix elements are computed by **MadGraph5_aMC@NLO** [89] that exploits a BSM model `mlrsm-nu-loop`, encoded in the Universal FeynRules Output (UFO) format [90]; then Pythia 8 is used for both showering and hadronisation.

The *detector simulation* is usually done using the **Geant4** [91] toolkit. After that, *digitisation* of the energy deposited in the each sub-detectors is done, producing digits written in Raw Data Objects (RDOs).

For the truth-level validation algorithm discussed in this thesis, the detector simulation step is skipped, so the analysis works directly on the generator-level truth files.

3.1.1 Reconstruction of physical objects

After detector simulation and digitisation, a series of algorithms is needed for the reconstruction of the digital signals into physics objects, like jets, muons,..:

- **Tracks and vertices** [92]: charged-particle tracks are reconstructed in the ID with an *inside-out*[1] algorithm, exploiting the hits recorded in each subdetector (Sec. 2.2.2). The process begins with seed-finding, where triplets of space-points from pixel and silicon detectors are combined to form seeds compatible with a helical track model. Each seed defines a candidate trajectory, which is then extended through the detector by a Kalman filter[2] that incorporates compatible space-points from successive layers. Candidates surviving quality selections are refitted with a global track fit accounting for material effects. Primary vertices are reconstructed by finding the position that best fits the set of tracks compatible with the interaction point, using an iterative fitting procedure.

- **Electrons and photons** [94]: are reconstructed from ECAL (Sec. 2.2.3) energy deposits matched to ID tracks. First, topological clusters (*topo-clusters*[3]) are built and used as

[1] The inside-out algorithm starts from seed candidates in the innermost layers of the detector and propagates outward, progressively adding compatible hits. This is complemented by an *outside-in* algorithm, which seeds from the outermost layers and works inward, recovering tracks missed by the primary pass.

[2] The Kalman filter is a recursive algorithm that estimates the track parameters by combining a prediction step, based on the propagation of the current state to the next detector layer, with an update step, where the prediction is corrected using the newly measured hit. It also accounts for material effects such as energy loss and multiple scattering at each step [93].

[3] Topo-clusters are 3D clusters of calorimeter cells, grouped according to their energy deposit significance with respect to the noise level. The shape and size of the cluster depend on the topology of the shower [95].

seeds to form *superclusters*, which also recover energy lost due to Bremsstrahlung radiation (for electrons) and interactions with detector material (for photons). Simultaneously, ID tracks are refitted accounting for these energy losses and for photon pair production, and are then matched to the superclusters. Electrons are identified as superclusters matched to at least one ID track, while photons are either matched to a conversion vertex (from $\gamma \to e^+e^-$ pair production) without a prompt ID track, or left unmatched to any ID track (unconverted photons).

- **Muons** [96]: are reconstructed independently in the ID and the MS and then combined into a global muon candidate. Several reconstruction types are defined: *Combined* (CB) muons are obtained from a global fit of ID and MS tracks, also accounting for energy loss in the calorimeters; *Segment-Tagged* (ST) muons are typically low-p_T muons for which a full MS track cannot be reconstructed and are instead formed from an ID track matched to at least one MS track segment; *Calorimeter-Tagged* (CT) muons are formed from ID tracks matched to calorimeter energy deposits consistent with a minimum ionising particle; *Inside-Out* (IO) muons are obtained by extrapolating ID tracks into the MS and fitting them with loosely associated MS hits, without requiring a full MS track; finally, *Muon-Spectrometer Extrapolated* (ME) muons are standalone MS tracks extrapolated to the beamline, extending the muon acceptance beyond the ID coverage.

- **Jets** [97]: are reconstructed through the anti-k_t [98] jet algorithm with a radius parameter $R = 0.4$, implemented in the FastJet package [99]. The algorithm takes as input a system of topo-clusters and tracks, called Particle Flow Objects (PFOs). For each pair of input objects i and j, the distance $d_{ij} = \min(k_{ti}^{-2}, k_{tj}^{-2})\frac{\Delta_{ij}^2}{R^2}$ is computed, where k_{ti} is the transverse momentum of object i and $\Delta_{ij}^2 = (\eta_i - \eta_j)^2 + (\phi_i - \phi_j)^2$ is the squared angular distance. This is compared with the beam distance $d_{iB} = k_{ti}^{-2}$: at each iteration, if $d_{ij} < d_{iB}$, objects i and j are merged into a single pseudojet, otherwise, i is promoted to a final jet and removed from the list. This procedure continues until all input objects are clustered, producing jets with conical shapes whose boundaries are stable against soft and collinear emissions.

- **Missing transverse energy** (E_T^{miss}) [100]: is the magnitude of the negative vector sum of the transverse momenta of all reconstructed objects. It is composed of two terms: a *hard* term, accounting for the transverse momenta of fully reconstructed and calibrated hard objects (electrons, muons, jets, etc.) and a *soft* term, built from ID tracks associated with the hard scatter vertex but not with any hard object. The E_T^{miss} is therefore defined as $\vec{E}_T^{miss} = -\left(\sum_{hard} \vec{p}_T + \sum_{soft} \vec{p}_T\right)$ and its magnitude $E_T^{miss} = |\vec{E}_T^{miss}|$ provides a measure of the total transverse momentum carried away by undetected particles, such as neutrinos.

3.1.2 TRUTH derivation

After passing through the reconstruction algorithms, the output files produced in the Analysis Object Data (AOD) format are subsequently reduced into a Derived AOD (DAOD) format. In the case of TRUTH derivations [87], the DAOD files contain only truth-level information (the kinematics of simulated particles before the addition of any detector simulation) for all events. Three formats of TRUTH derivations are available:

- `TRUTH0`: is a copy of the event file in xAOD[4] format;
- `TRUTH1`: is the most heavy format which contains the full truth record;
- `TRUTH3`: is lighter with respect to the previous cases since it contains just the most relevant truth information.

The truth-level validation performed in this thesis operates on `TRUTH3` DAODs and characterises the generator-level properties of LRSM heavy-neutrino signal samples.

3.1.3 Analysis framework

ATLAS offline analysis is based on **Athena** framework, written in C++ and built with *Gaudi* architecture[5][102]. Athena jobs are built around a chain of algorithms, based on three main methods: `initialize()`, called once at the beginning of the job, immediately after the configuration, `execute()`, that runs once per event and `finalize()`, called after the last job [87]. A lot of physics analyses are also done using a lighter environment which is called **AnalysisBase**. This uses only packages needed to read DAOD files and to run algorithms for the analysis, which are implemented with the same `initialize()`, `execute()` and `finalize()` as in the Athena counterpart. Within AnalysisBase, the processing of events is done through the **EventLoop** (EL) framework. In this context, `evtStore()->retrieve()` is used to retrieved physics objects from the event store and additionally, the so called *Combined Performance* (CP) tools can be used to apply calibration corrections, efficiency scale factors and systematic uncertainties for each object type (electrons, muons, jets, etc.). At truth-level, as in the validation algorithm presented in this work, CP corrections are not applied. The components of the data and simulation processing chain are summarised in Fig. 3.1.

```
pp collision / Event Generator (Pythia, MadGraph)
↓
Detector Simulation / Geant4
↓
Reconstruction → AOD
↓
Derivation → DAOD (TRUTH1, TRUTH3, ...)
↓
EventLoop / AnalysisBase
↓
Statistical Analysis
```

Figure 3.1: Schematic of the ATLAS data and simulation processing chain.

[4]Both AOD and DAOD files are stored using the xAOD data model, the ROOT-based event data format adopted by ATLAS since Run 2, which provides a representation of reconstructed and truth-level objects [101].

[5]Gaudi is a software package used to build data processing applications for High-Energy Physics experiments.

The truth-level MC validation algorithm presented in the next chapter operates at the EventLoop stage, reading DAOD inputs and producing ROOT output for offline analysis.

3.2 Baseline analysis strategy

This section describes the analysis strategy of the baseline search for the process $gg \to h/\Delta \to NN \to 2l^{\pm}4j$ (Sec. 1.10.2) at $\sqrt{s}$ = 13,TeV, on which the work presented in this thesis builds. To the best of our knowledge, this represents the first dedicated study of this signal topology in a collider experiment.

The signal mass points investigated are chosen to maximise the BR for $\Delta \to NN$ and the production cross-section for $gg \to \Delta$ (Fig. 1.9, left), while avoiding contamination from the $\Delta \to ZZ$ and $\Delta \to WW$ channels (Fig. 1.9, right).

The adopted analysis strategy only considers *prompt* objects ($c\tau$ < 3 mm, Fig. 3.2), since heavy-neutrinos with a decay length exceeding 3 mm produce displaced vertices, which are not reconstructed by the methods described in this work. The signal mass hypotheses are therefore restricted accordingly to the region of the (m_N, m_Δ) parameter space where the N decay is mostly prompt (Fig. 1.10).

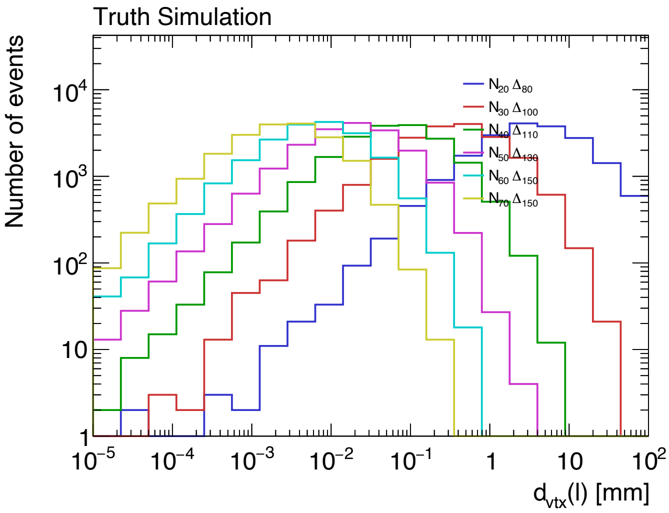

Figure 3.2: Distribution of the transverse decay length $d_{\text{vtx}}(l)$ of the heavy-neutrino at truth-level, for the six signal mass hypotheses considered in the analysis.

The bulk of the distributions lies well below the 3 mm prompt-decay threshold, confirming that the selected mass points are compatible with a prompt analysis.

Overall, this strategy ensures that the analysis targets the most experimentally accessible region of the LRSM scalar sector at LHC energies.

3.2.1 Trigger selection and object definition

To select interesting events, unprescaled[6] dilepton triggers (Tab. 5.1), requiring pairs of same- or mixed-flavour charged leptons (ee, $\mu\mu$, or $e\mu$) are used [103, 104]. Two lepton selection working points are defined: *tight* leptons (selected with stringent criteria of background rejection) are considered signal candidates while *loose* leptons (selected with less stringent background rejection criteria), mostly non-prompt, are used to estimate reducible backgrounds. Signal electrons and muons must also satisfy specific conditions for the p_{T} (that needs to be greater then 17 GeV for electrons and greater then 22 GeV for muons), $|\eta|$ and isolation. These thresholds represent the primary bottleneck for the signal efficiency, since the final-state leptons in the LRSM signal tend to have a soft transverse momenta, particularly at low masses (m_N, m_Δ) (See Fig. 4.1).

Table 3.1: Summary of the unprescaled dilepton triggers used in the analysis, divided per year. The lepton p_T threshold in GeV is indicated in the trigger name after the `e` and `mu` characters, for electrons and muons respectively [103, 104].

	2015	**2016**	**2017–2018**
ee	`HLT_2e12_lhloose_L12EM10VH`	`HLT_2e17_lhvloose_nod0`	`HLT_2e17_lhvloose_nod0_L12EM15VHI` or `HLT_2e24_lhvloose_nod0`
$e\mu$	`HLT_e17_lhloose_mu14`	`HLT_e17_lhloose_nod0_mu14`	`HLT_e17_lhloose_nod0_mu14`
$\mu\mu$	`HLT_mu18_mu8noL1`	`HLT_mu22_mu8noL1`	`HLT_mu22_mu8noL1`

To suppress the dominant Drell-Yan (DY) background, the final state leptons are further selected based on their electric charge, which has to be equal for the two objects (SS leptons).

Jets instead are reconstructed with the anti-k_t algorithm ($R = 0.4$, `AntiKt4EMPFlow`) and required to have $p_{\mathrm{T}} > 20$ GeV and $|\eta| < 2.5$. An overlap removal procedure also resolves ambiguities between reconstructed electrons, muons and jets.

3.2.2 Analysis regions

Selected events are categorised into mutually exclusive *analysis regions*: **Signal Regions** (SRs) maximise the probability of selecting signal events, **Control Regions** (CRs) constrain the background Normalisation Factors (NFs) as free parameters in the likelihood fit and **Validation Regions** (VRs) which perform cross-check background estimates without entering the fit. The optimisation of the SRs is performed by maximising the expected signal significance [105], defined as

$$\mathcal{S} = \sqrt{2\left[(S+B)\ln\left(1+\frac{S}{B}\right) - S\right]}, \tag{3.1}$$

where S is the number of signal events and B represents the total contribution from background events. In the limit for $S \ll B$, Eq. 3.1 reduces to $S/\sqrt{B}$.

[6] A trigger is called unprescaled when every event satisfying the trigger condition is recorded, in contrast to prescaled triggers, where only a fraction of events is kept, in order to reduce the data acquisition rate.

The first analysis strategy is cut-based, where signal events are selected by applying constraints on the values of the kinematic variables characteristic of each event. As a step further, a new method involving Machine Learning (ML) is used to enhance the signal-background separation.

Cut-based signal regions

Three SRs are defined by requiring exactly two SS light leptons and a fixed jet multiplicity: **SR2J** (with number of jets $N_{\text{jets}} = 2$), **SR3J** ($N_{\text{jets}} = 3$) and **SR4J** ($N_{\text{jets}} = 4$). In these regions, the dilepton invariant mass $m_{ll} < 80\,\text{GeV}$ (to suppress Z-peak background from charge misidentification), $E_{\text{T}}^{\text{miss}} < 150\,\text{GeV}$ (exploiting the absence of SM neutrinos in the signal) and upper bounds on the leading and sub-leading lepton $p_T < 100, 150\,\text{GeV}$ respectively are required. In SR4J, an additional variable $\Delta(m_{ljj})_{\text{min}}$ is introduced: for each lepton, the minimum difference among all two-jet invariant mass combinations is computed and a cut $\Delta(m_{ljj})_{\text{min}} < 60\,\text{GeV}$ is applied to exploit the expectation that leptons and jets from the same N decay have a small (almost zero) invariant mass difference.

Dedicated CRs and VRs are instead defined for the three dominant backgrounds:

- The DY CR (DYCR) requires OS leptons with $80 < m_{ll} < 120\,\text{GeV}$ and at least two jets;
- The diboson CR (DBCR) requires SS leptons with $200 < m_{ll} < 300\,\text{GeV}$, at most three jets and $E_{\text{T}}^{\text{miss}} > 30\,\text{GeV}$;
- The top CR (TopCR) requires OS leptons with $130 < m_{ll} < 300\,\text{GeV}$ and at least two b-tagged jets[7].

Dedicated validation regions (VRs) are defined with selections analogous to the corresponding CRs, but with modified dilepton invariant mass requirements to ensure orthogonality with both the SRs and CRs, while ensuring that the targeted background remains the dominant contribution. Specifically:

- The DY VR (DYVR) requires OS leptons with $120 < m_{ll} < 1000\,\text{GeV}$;
- The diboson VR (DBVR) requires SS leptons with $300 < m_{ll} < 600\,\text{GeV}$ and $E_{\text{T}}^{\text{miss}} > 30\,\text{GeV}$;
- The top VR (TopVR) requires OS leptons with $300 < m_{ll} < 1500\,\text{GeV}$ and at least two b-tagged jets.

This cut-based approach yields very low signal significance across all distributions and variables, thus motivating the introduction of a multivariate technique to discriminate between signal and background.

[7] A b-tagged jet is a jet identified as likely originating from the hadronisation of a b-quark, using dedicated multivariate algorithms that exploit the characteristic features of b-hadron decays: a displaced secondary vertex, a relatively long decay length ($c\tau \simeq 450\,\mu\text{m}$), and the presence of tracks with large impact parameters with respect to the primary vertex [106].

Multivariate analysis regions

A parametrised Multi-Layer Perceptron (MLP) neural network is trained simultaneously on all signal mass points, taking (m_N, m_Δ) as additional inputs to ensure continuous interpolation across the parameter space. The architecture consists of four hidden layers of width 256 with Rectified Linear Unit (ReLU) [107] as activation function[8]. Each node applies a non-linear activation function to a weighted sum of its inputs and the weights are optimised during training by minimising the loss function via back propagation. A neural network architecture and the most common activation functions are shown in Fig. 3.3 as an example.

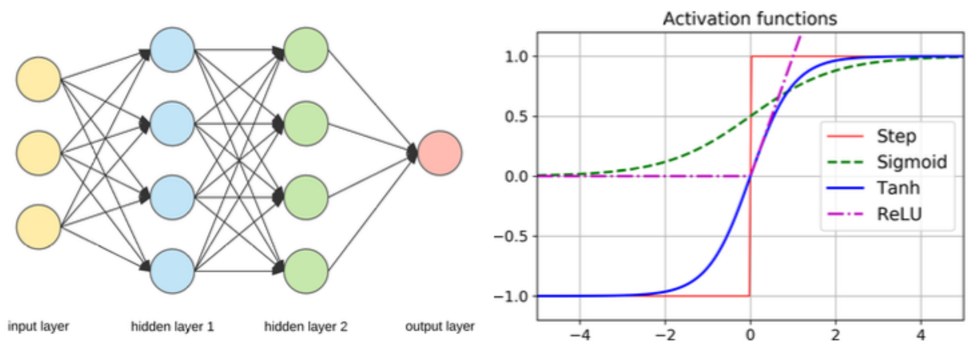

Figure 3.3: Left: schematic representation of a fully-connected neural network, consisting of an input layer, two hidden layers and an output layer with a single neuron for binary classification. Right: common activation functions used in neural networks, illustrating their different behaviours in the positive and negative input domains [108].

The chosen loss function is instead represented by the Binary Cross-Entropy loss [107], that is minimised to obtain well-calibrated posterior probabilities for the signal. Its input features include the p_T, η, ϕ, invariant masses and angular separations of the reconstructed leptons and jets, as well as event-level quantities and $E_{\mathrm{T}}^{\mathrm{miss}}$.

The ML score (a value in $[0, 1]$ interpretable as a signal probability) is used to define analysis regions: SRs require ML score > 0.8, CRs require ML score < 0.4 and VRs occupy the intermediate range $[0.4, 0.8]$. The $m_{ll} < 80\,\mathrm{GeV}$ requirement is retained in the SRs to suppress the Z-peak. The selection criteria for all multivariate analysis regions are summarised in Table 3.2.

Table 3.2: Selection criteria for the multivariate analysis regions, defined on the basis of the ML score, the number of jets, the number of b-tagged jets, the lepton charge combination and the dilepton invariant mass m_{ll}. Exactly two leptons are required in all regions.

Quantity	MLSR2J	MLSR3J	MLSR4J	MLTopCR	MLDBCR	MLDYCR	MLTopVR	MLDBVR	MLDYVR
$N_{b\text{-jets}}$	0	0	0	≥2	0	0	≥2	0	0
Charge	SS	SS	SS	OS	SS	OS	OS	SS	OS
N_{jets}	=2	=3	=4	≥2	<3	≥2	–	<3	≥2
$m_{\ell\ell}$ [GeV]	≤80	≤80	≤80	>200	>200	>80	–	>200	>80
ML score	>0.8	>0.8	>0.8	<0.4	<0.4	<0.4	[0.4,0.8]	[0.4,0.8]	[0.4,0.8]

[8]Is a non-negative activation function defined as $f(x) = \max(0, x)$, that is applied after each hidden layer.

3.2.3 Background estimation

Backgrounds are classified as *irreducible* (prompt leptons from SM processes, estimated from MC simulation with NFs floated in the fit) and *reducible* (misidentified or non-prompt leptons, estimated with data-driven methods).

Electron charge misidentification consists in hard Bremsstrahlung followed by asymmetric photon conversion, *trident events* (Fig. 3.4, right) or incomplete track reconstruction, *stiff tracks* (Fig. 3.4, left) that can flip the reconstructed charge of prompt electrons.

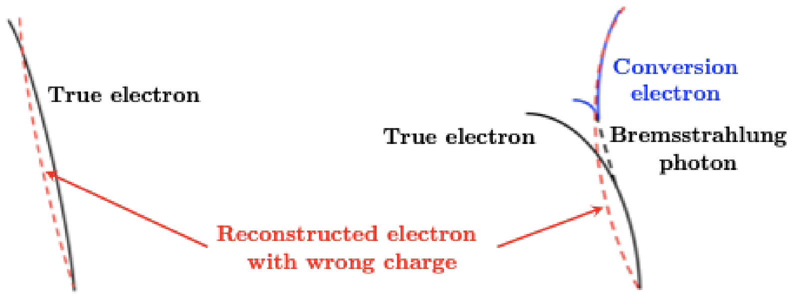

Figure 3.4: Left: a stiff track, where incomplete reconstruction of a high-curvature track leads to an incorrect charge assignment. Right: a trident event, where hard Bremsstrahlung followed by asymmetric photon conversion produces an additional electron of opposite charge that is reconstructed instead of the original.

Fake and **non-prompt leptons** involve events with at least one fake or non-prompt lepton (Fig. 3.5). Non-prompt lepton originating from a Secondary Vertex (SV), such as an in-flight decay of a b- or c-hadron for example, a jet misidentified as a lepton, or an electron from photon conversion, which is incorrectly associated to the primary vertex and selected as a fake lepton, represent the dominant irreducible background.

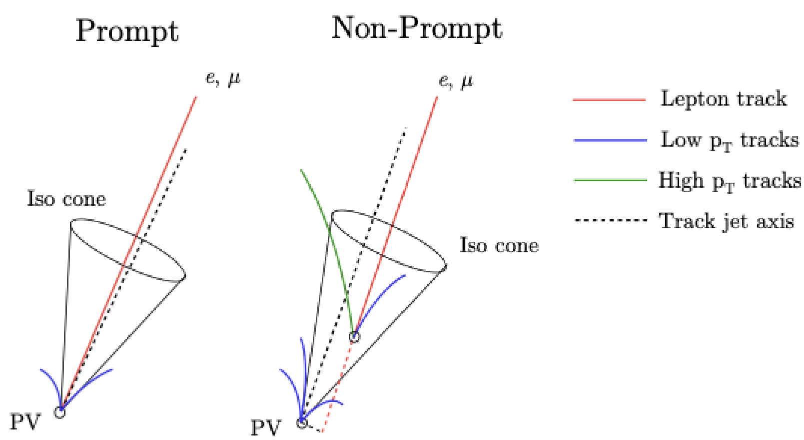

Figure 3.5: Illustration of prompt and non-prompt lepton production at a hadron collider. Left: a prompt lepton produced directly at the Primary Vertex (PV) from a hard scatter process. Right: a non-prompt lepton originating from a SV.

3.2.4 Statistical analysis

Signal extraction is performed with a binned profile likelihood fit implemented in the **TRExFitter** framework [109], which interfaces with ROOT, RooFit [110] and RooStats [111]. The likelihood function takes the form

$$\mathcal{L}(\mu, \alpha, \gamma, \tau) = \mathcal{L}_{\text{phys}}(\mu, \alpha, \gamma, \tau) \cdot \mathcal{L}_{\text{aux}}(\alpha) \cdot \mathcal{L}_{\text{stat}}(\gamma), \tag{3.2}$$

where μ is the signal strength (the parameter of interest), α are Nuisance Parameters (NPs) encoding experimental and theoretical uncertainties, γ account for per-bin MC statistical uncertainties and τ are unconstrained normalisation parameters for the dominant backgrounds. $\mathcal{L}_{\text{phys}}$ is a product of Poisson terms over all bins and regions; $\mathcal{L}_{\text{aux}}$ constrains the NPs with Gaussian auxiliary terms; $\mathcal{L}_{\text{stat}}$ accounts for limited MC statistics with Poisson terms.

The fit proceeds in two stages: first, a *background-only fit* is performed simultaneously in all CRs, with the DY, diboson and $t\bar{t}$ NFs left free to float; the resulting NFs are then tested in the VRs. Second, an *exclusion fit* is performed independently for each (m_N, m_Δ) signal mass hypothesis, using the ML score distribution as the discriminating variable. Upper limits at 95% CL are set with the CL$_s$ method [112] using the profile likelihood ratio as test-statistic and the asymptotic approximation.

3.2.5 Baseline sensitivity and motivation for further optimisation

The expected 95% CL exclusion limits obtained with the baseline analysis strategy, including statistical uncertainties only, are shown in Fig. 3.6.

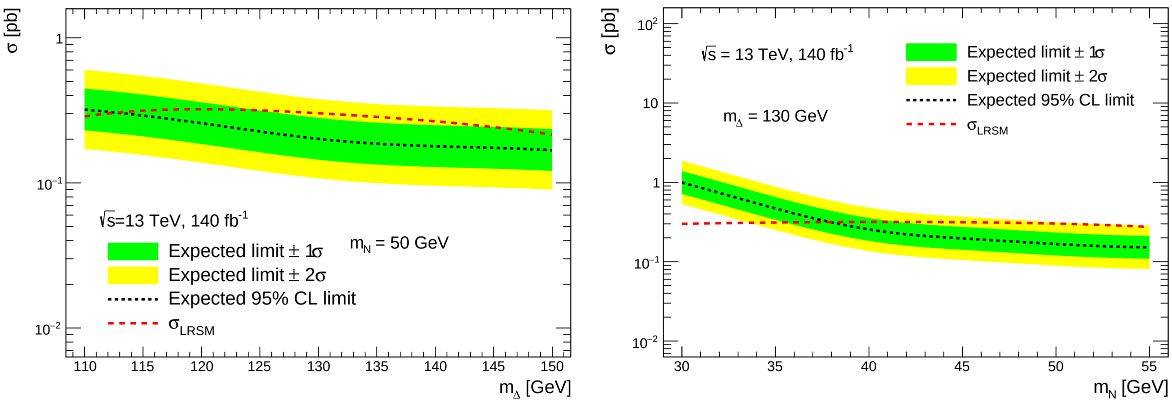

(a) Exclusion plot shown as a function of m_Δ, with m_N fixed at 50 GeV.

(b) Exclusion plot shown as a function of m_N, with m_Δ fixed at 130 GeV.

Figure 3.6: Expected 95% CL exclusion limit from the baseline analysis for the LRSM-allowed process studied in this thesis, with the corresponding one- and two-standard-deviation uncertainty bands derived from a statistical-only fit. The theoretical signal cross-section prediction, given by the N3LO calculation, is shown as the red dotted line.

In Fig. 3.6a, the limit is nearly flat across the scanned range, indicating little sensitivity dependence on the scalar triplet mass in this region.

Across the full mass range, the expected limit lies very close to the theoretical LRSM cross-section prediction, without falling below it. This (almost) overlap between the two curves implies that no mass point can be excluded at 95% CL. To establish a meaningful exclusion, the expected limit must lie sufficiently below the LRSM theoretical cross-section.

The analysis strategy developed in this work therefore aims to increase the sensitivity of the search, reducing the expected limit relative to the theoretical prediction and extending the accessible region of parameter space.

Chapter 4

Truth-level MC validation

Starting from the results of the baseline analysis described in Sec. 3.2, the work of this thesis is aimed at improving the sensitivity by investigating alternative event selection strategies.

The optimisation strategy is structured in three steps, each building on the previous:

1. **Truth-level MC validation** (Chap. 4): characterisation of the signal kinematic properties at generator-level, as a necessary first step before any selection optimisation;

2. **Alternative selection strategies and scale factors computation** (Sec. 5.1): systematic study of event yields varying the lepton and jet p_{T} thresholds, quantifying for each selection variation the relative increase in signal and background yields, in order to identify selections for which the signal increases more than the background;

3. **Expected signal strength estimation** (Sec. 5.2): statistical fit procedure to assess the improvement in sensitivity relative to the baseline analysis strategy.

The signal MC simulated events are analysed at truth-level, before the introduction of particles' interaction with the detector, to validate the MadGraph5_aMC@NLO [89] model and study the kinematic of signal events. The target of this analysis is the BSM decay chain depicted in Fig. 1.7, involving LRSM heavy Majorana neutrinos, and the final-state under study is composed by two charged leptons and four quarks (which hadronise into four jets). This process is characterised by the presence of SS leptons in the final-state (in 50% of the events) and no missing transverse energy from SM neutrinos, making it an experimentally distinctive topology. However, a key challenge in this channel is the softness of the final-state objects: both the charged leptons (Fig. 4.1a) and the jets (Fig. 4.1b) carry transverse momenta $p_{\mathrm{T}} \in [0, 20]$ GeV for many signal benchmark points, making the signal to background discrimination a non-trivial task. The Jet Energy Resolution (JER[1]) is also studied as a function of jet p_{T} to quantify the degradation in resolution at low transverse momenta, which also affects the discriminating power of cut-based variables.

The truth-level study is performed across multiple signal mass points, varying both m_N and m_Δ, in order to understand the kinematic regime the analysis is sensitive to. The analyses presented in the first part of the chapter are done exploiting six different samples with 10000 generated events each, for six different mass hypotheses for the heavy-neutrinos N_i and Δ, as

[1]The JER is defined as the relative width of the jet energy (or p_{T}) response distribution, $\sigma(p_{\mathrm{T}})/p_{\mathrm{T}}$ and quantifies the precision with which the jet energy is measured.

can be observed in the legends of the plots. Then, the number of generated events is increased to 100000, focusing on a single benchmark mass point ($m_N = 50\,\text{GeV}$, $m_\Delta = 130\,\text{GeV}$) as a reference; the study is subsequently extended to additional mass points in Chap. 5.

The results of this truth-level study provide the foundation for understanding the expected signal yield and kinematic properties in the ongoing search for LRSM heavy-neutrinos described in Sec. 3.2, with the aim of finding ways to improve the achieved significance.

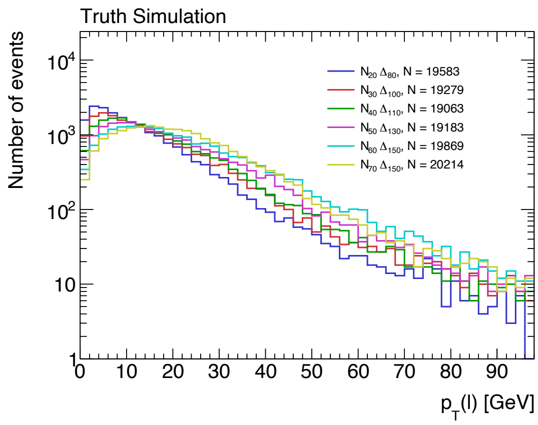

(a) Leptons p_{T} distribution

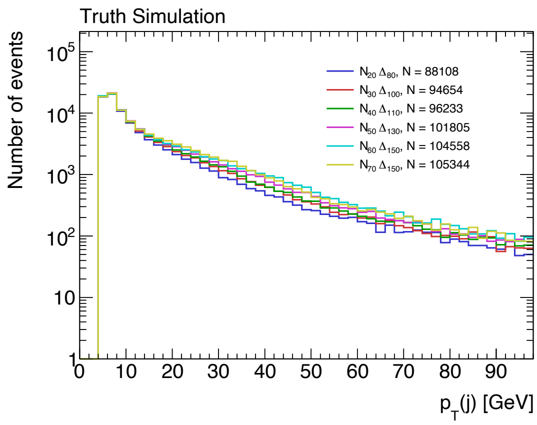

(b) Jet p_{T} distribution

Figure 4.1: Transverse momentum distributions of the final-state charged leptons (a) and jets (b) for the signal sample. Both objects are predominantly produced with low transverse momentum, with a large fraction populating the region below 20 GeV, highlighting the soft nature of the signal topology.

4.1 Validation algorithm

The validation algorithm processes xAOD truth-particle containers and truth-jets event by event. It has got some configurable properties, above which, the PDG-ID of the BSM particles involved in the process under study, like the Δ mediator and the three heavy-neutrinos N_1, N_2, N_3, which are assumed to be mass-degenerate within the same lepton flavour and are therefore treated equivalently throughout the analysis.

4.1.1 Truth-particles selection

At the beginning of each event, all truth-particles are iterated over and two selection criteria are applied: particles originating from hadron decays and gluons are discarded. These selections are designed to retain only particles from the hard scattering and subsequent decays through EW or BSM processes, also reducing the QCD background.

Any particle whose PDG-ID matches at least one of the configured values, and which has at least one child, is considered as potential signal.

The decay chain is then traversed to identify the heavy-neutrinos arising from the Δ decay, which are selected and classified according to their PDG-ID. These neutrinos are subsequently assigned to three separate vectors, N_1, N_2, and N_3 (PDG-IDs 61, 62, and 63, respectively). Similarly, for the heavy-neutrinos, the algorithm iterates over their children in the decay chain and classifies them by type:

- **Charged leptons**: electrons and muons can be accepted if they are not radiated by photons or produced in τ-decays, while taus can be accepted if they are not originating from a photon, a hadron or a gluon.
- **Quarks**: are accepted only if they are not produced in a gluon decay.

4.1.2 Event selection and observables

The signal signature is the one characterized by two charged leptons and four quarks in the final-state. Events matching this topology are therefore selected, while the hadronization of the quarks into jets is considered later on in the process. The events which are discarded by these selection criteria are of three types (Tab. 4.1): the ones containing zero or two quarks in the final-state (Fig. 4.2a) , the ones containing three or four leptons in the final-state (Fig. 4.2b), or the ones which are not mediated by Δ, but by the SM Higgs.

Table 4.1: Summary of the event classification after applying the selection criteria for a reference mass point $m_N = 50\,\text{GeV}$, $m_\Delta = 130\,\text{GeV}$. The majority of events correspond to the target final-state topology with two charged leptons and four quarks, while the remaining events are rejected either because they do not originate from a Δ decay or because they contain a different final-state particle multiplicity.

Category	**Events**
Total events	100.00%
Without Δ (0 quarks and 0 leptons)	6.12%
With 2 leptons + 4 quarks	89.94%
With leptons $\neq$ 2 or quarks $\neq$ 4, not both 0	3.94%

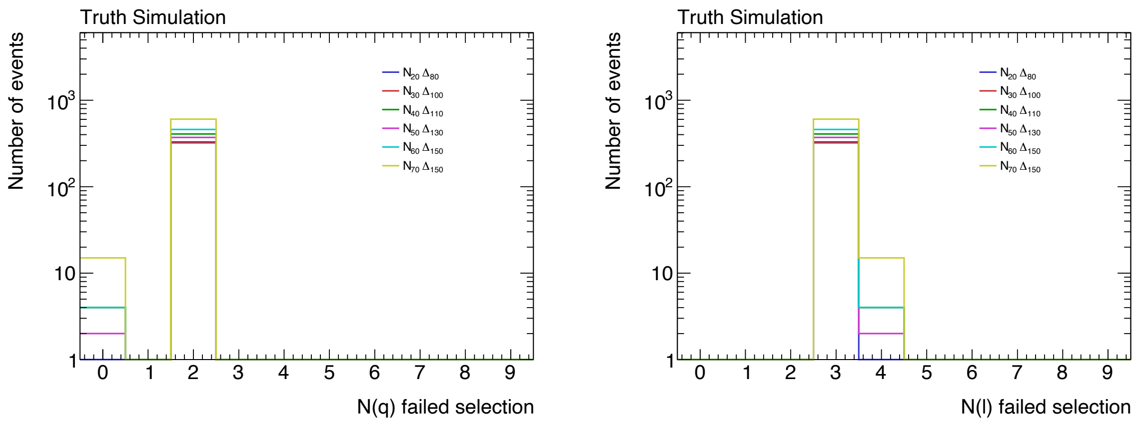

(a) Number of quarks in the events that do not pass the two-lepton and four-quark selection. Most events contain two quarks.

(b) Number of leptons in the events that do not pass the two-lepton and four-quark selection. Most events contain three leptons.

Figure 4.2: Multiplicity of quarks (a) and leptons (b) in events failing the requirement of two leptons and four quarks.

The firsts two cases specifically, come from the fact that the off-shell W_R^* can decay leptonically into a charged-lepton and a (Majorana) neutrino, giving final-states of the type $ll\nu lqq$ or $ll\nu ll\nu$.

For all final-state objects, a set of kinematic observables is evaluated. These include the transverse momentum, pseudorapidity and azimuthal-angle distributions of all charged leptons and quarks originating from heavy-neutrino decays. The invariant masses of the Δ, the heavy-neutrinos and the full Δ decay system are also reconstructed. Furthermore, the analysis considers the $\Delta R = \sqrt{(\Delta\eta)^2 + (\Delta\phi)^2}$ separation between the two leading objects of the same type, the ratio of sub-leading to leading lepton transverse momentum, the jet multiplicity and the ratio of sub-leading to leading jet transverse momentum. The missing transverse energy is included among the studied observables.

The kinematic properties and particle-identification information of all selected objects are retained for subsequent analysis. At the end of the processing, a detailed summary of the event selection is also produced, including the number of events surviving each stage of the selection. The fractions of electrons, muons and taus originating from each of the three heavy-neutrino generations are also computed, providing a consistency check of the generator-level branching fractions.

4.2 Δm_{lqq} observable

At the quark level, a key observable is

$$\Delta m_{lqq} = |m_1 - m_2|, \tag{4.1}$$

where m_1 and m_2 are the invariant masses of the two lqq systems reconstructed from the decay products of the heavy-neutrinos

$$m_1 = \sqrt{(\vec{p}_{l_0} + \vec{p}_{q_A} + \vec{p}_{q_B})^2} \quad \text{and} \quad m_2 = \sqrt{(\vec{p}_{l_1} + \vec{p}_{q_C} + \vec{p}_{q_D})^2} \tag{4.2}$$

with l_0, q_A and q_B originating from the decay of the same heavy-neutrino and similarly l_1, q_C and q_D, originating from the decay of the other heavy-neutrino. In the signal topology under consideration, the two heavy-neutrinos are produced with the same mass and each one decays into a charged lepton and two quarks. Consequently, the invariant masses of the corresponding lqq-systems are expected to reproduce the heavy-neutrino mass, $m_1 \simeq m_2 \simeq m_N$, leading to a Δm_{lqq} distribution strongly peaked at zero.

At reconstruction level, however, quarks are not directly accessible and the observable becomes Δm_{ljj}, computed from reconstructed jets. In the baseline analysis, what is actually evaluated $\Delta(m_{ljj})_{min}$, where the subscript *min* is because for each lepton, the minimum value of $|m_{l_0jj} - m_{l_1jj}|$ over all possible two-jet combinations is taken, in order to reduce the sensitivity to ambiguities in the assignment of the four final-state jets to the two heavy-neutrino decay chains. The corresponding distribution for this observable found in the baseline analysis exhibits a significant broadening well beyond the nominal value, for the mass hypothesis under consideration (Fig. 4.3), in contrast with the expectations.

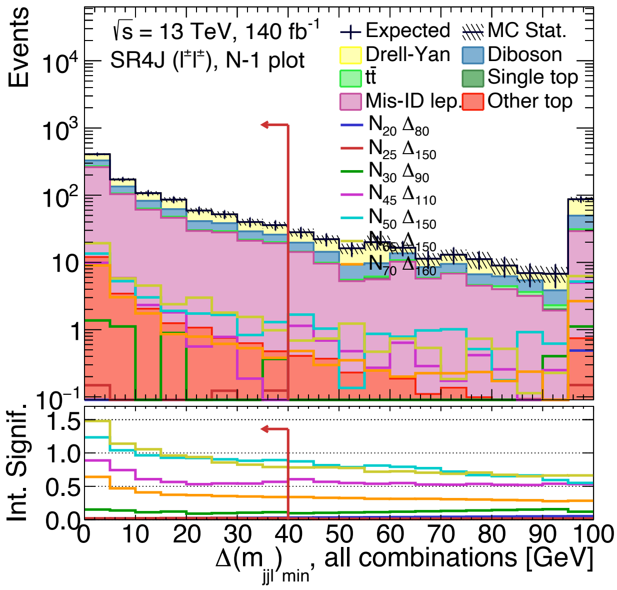

Figure 4.3: Distribution of $\Delta(m_{ljj})_{\min}$ in SR4J (Signal Region with 4 jets present), shown as a N−1 plot with all the baseline selection requirements applied except the cut on this variable itself, using $\sqrt{s} = 13$ TeV data corresponding to 140 fb^{-1}. The lower panel shows the integrated signal significance as a function of the upper cut value.

The significant broadening of the distribution motivates a truth-level investigation to determine whether this effect originates from detector and reconstruction effects or is already present at generator-level. Since this variable plays an important role in the signal selection, it is essential to understand the origin of this behaviour before applying any cut on it. The truth-level study therefore proceeds in two steps: first, Δm_{lqq} is examined at generator-level, where the jet-assignment ambiguity is resolved by matching directly to the truth quarks, considering the decay chain info from MC; then, Δm_{ljj} is studied after truth-jet reconstruction.

4.2.1 Lepton–quark pairing and results

With two leptons and four quarks in the final-state, there exist 6 possibilities to associate the four quarks into pairs, then for each pair there are two ways to assign the two leptons, so this overall gives 12 possible combinations.

For each combination, the invariant masses m_1 and m_2 are computed (Eq. 4.2) and the combination that minimises the Δm is stored as the best pairing (App. A.1). However, since the assignment of leptons and quarks to the correct heavy-neutrino candidate that produced them is not known a priori, a truth-matching procedure is required.

At truth-level, the full decay chain information is avalaible, so it is possible to trace the entire decay chain of every particle in the final-state, to find which heavy-neutrino produced it. This is done by uniquely assigning each lepton and quark to the correct heavy-neutrino which produced them. For each lepton in the event, the parent's PDG-ID is checked recursively, until the PDG-ID of a heavy-neutrino is found. The same procedure is followed also for quarks. Once all the mothers have been found, l_0 is paired with the two quarks that have the same mother as l_0 and the other two quarks are assigned to l_1. To make sure that the correct topology is respected, the event is accepted only if the two leptons have distinct heavy-neutrino ancestors and each one of them is associated to exactly two quarks. The final pairing is therefore:

$$N^{(1)} \longrightarrow l_0 + q_A + q_B, \qquad N^{(2)} \longrightarrow l_1 + q_C + q_D \tag{4.3}$$

The mass difference $\Delta m_{lqq} = |m_1 - m_2|$ is computed for each correctly matched combination and its distribution is shown in Fig. 4.4. For the benchmark mass point $m_N = 50\,\text{GeV}$, $m_\Delta = 130\,\text{GeV}$, for example, the distribution has a Root Mean Square (RMS[2]) of $2.320 \pm 0.017\,\text{GeV}$.

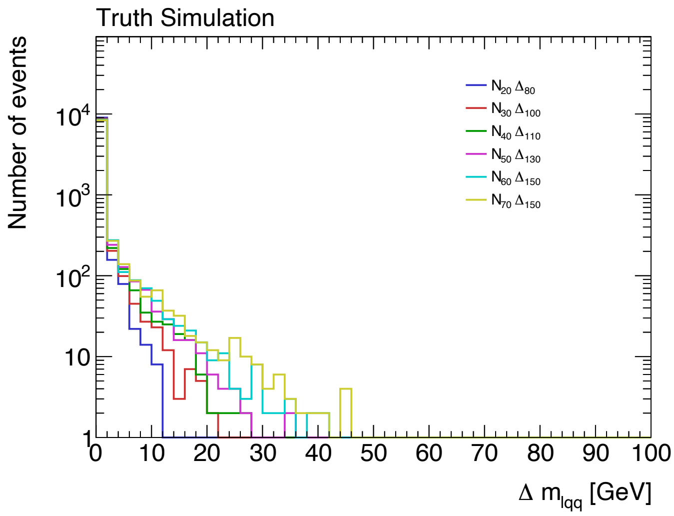

Figure 4.4: Distribution of the mass difference $\Delta m_{lqq} = |m_1 - m_2|$ between the two reconstructed lqq systems in the final-state.

As a validation for the algorithm, the invariant masses for the two heavy-neutrinos $N^{(1)}$ and $N^{(2)}$, reconstructed with the masses of the two systems $l_0 + q_A + q_B$ and $l_1 + q_C + q_D$ are shown in Fig. 4.5a and Fig. 4.5b. For the benchmark mass point $m_N = 50\,\text{GeV}$, $m_\Delta = 130\,\text{GeV}$, for example, the distribution has a Root Mean Square of $29.043 \pm 0.084\,\text{GeV}$.

[2]The RMS is the standard deviation of the distribution and provides a measure of its width, corresponding to the reconstruction resolution for the observable under study.

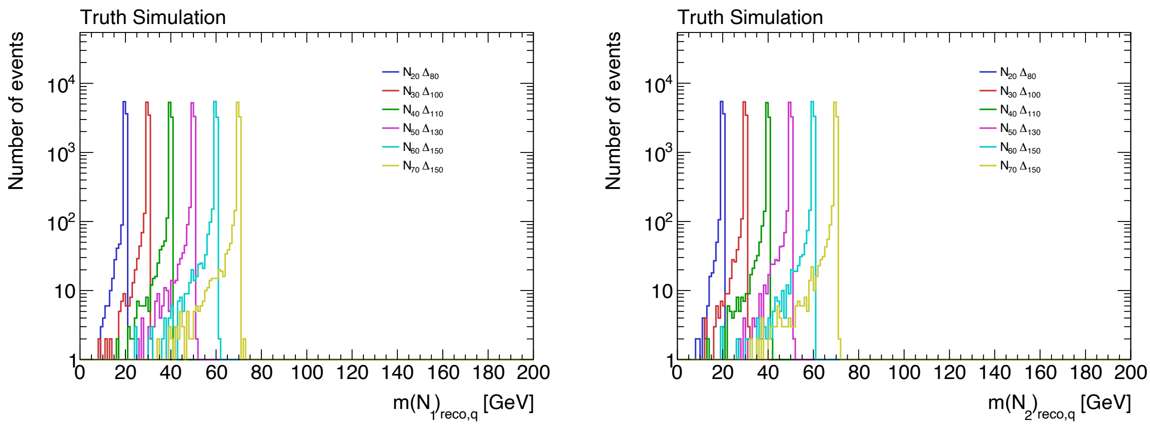

(a) Reconstructed invariant mass distribution of the heavy-neutrino candidate $N^{(1)}$, obtained from the $l_0 q_A q_B$ system.

(b) Reconstructed invariant mass distribution of the heavy-neutrino candidate $N^{(2)}$, obtained from the $l_1 q_C q_D$ system.

Figure 4.5: Reconstructed invariant mass distributions of the two heavy-neutrino candidates.

The tails observed in the distributions arise from effects of the object propagation and selection for the invariant mass reconstruction.

4.3 Δm_{ljj} observable

After the correct lepton-quark pairing is identified, the algorithm associates each of the four quarks with a reconstructed truth-jet, using a geometric matching criterion. When all four quarks are matched, the heavy-neutrino masses are reconstructed using the matched jets, in the same way as before with quarks instead of jets. This time using the jets' four-momenta, the mass difference becomes Δm_{ljj}

$$\Delta m_{ljj} = |m_1 - m_2|, \tag{4.4}$$

between the masses of the two systems $l_0 + j_A + j_B$ and $l_1 + j_C + j_D$.
Jets are matched to quarks by identifying the closest jet in terms of angular distance, defined as

$$\Delta R = \sqrt{(\Delta\eta)^2 + (\Delta\phi)^2} \tag{4.5}$$

The matching is performed sequentially: for each quark, jets are scanned and the closest candidate is selected, while ensuring that each jet can be assigned to at most one quark. A maximum matching criterion of $\Delta R_{\max} = 0.4$ is imposed, consistent with the typical ATLAS jet radius parameter [113]. If no jet within this angular distance is found for a given quark, the entire combination is rejected. Once a jet is assigned to a quark, it is excluded from further assignments to avoid multiple matches.

In addition, a complementary inclusive jet-matching variant is also constructed, in which successful matching requires only that two out of the four quarks need to be matched to jets. This criterion is relevant for signal efficiency studies (Chapter 5). An alternative p_{T}-based jet-matching strategy is also developed alongside the standard ΔR-based approach and is described in App. A.2.

The distribution of Δm_{ljj} is shown in Fig. 4.6. For the benchmark mass point m_N = 50 GeV, m_Δ = 130 GeV, the distribution has a RMS of 10.071 ± 0.227 GeV, that is way larger then the one calculated for Δm_{lqq} in Sec. 4.2.1.

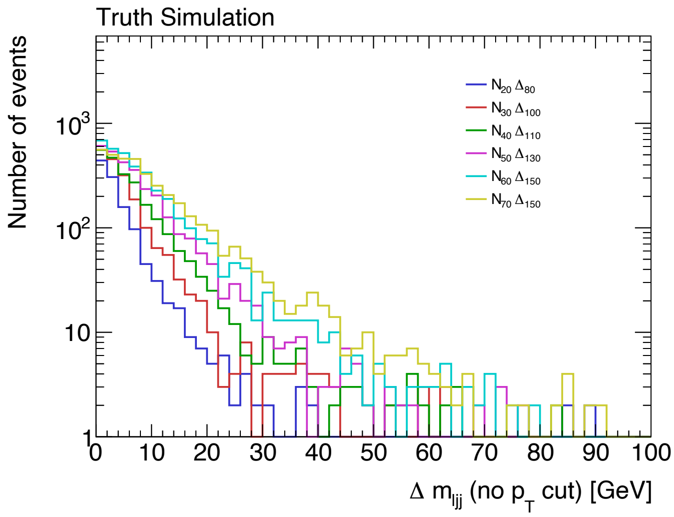

Figure 4.6: Distribution of the mass difference $\Delta m_{ljj} = |m_1 - m_2|$ between the two reconstructed ljj systems in the final-state. No cut on jet transverse momentum was applied. The observable quantifies the consistency of the reconstruction with the hypothesis of two equal-mass heavy-neutrinos.

The distributions of the invariant masses of $N^{(1)}$ (Fig. 4.7a) and $N^{(2)}$ (Fig. 4.7b) reconstructed with the masses of the two systems $l_0 + j_A + j_B$ and $l_1 + j_C + j_D$ are again used as a validation of the algorithm.

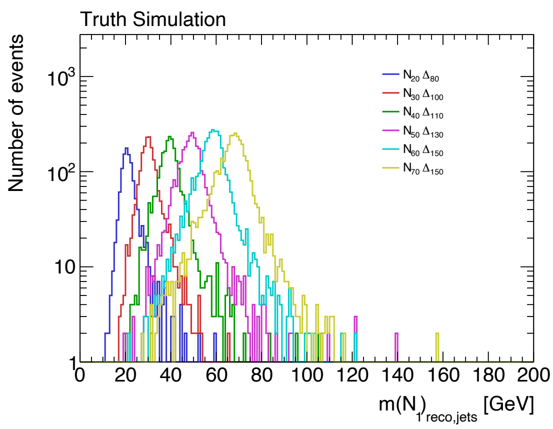

(a) Reconstructed invariant mass distribution of the first heavy-neutrino candidate $N^{(1)}$, obtained from the $l_1 j_A j_B$ system.

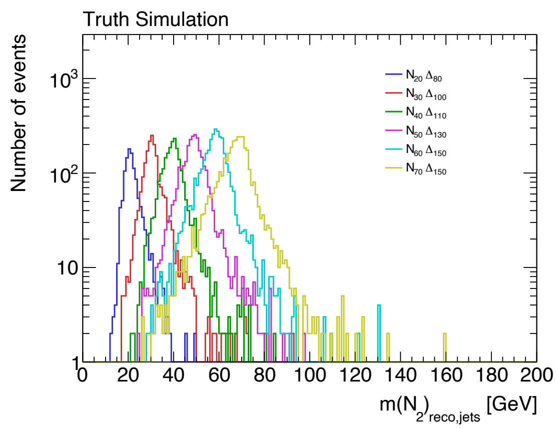

(b) Reconstructed invariant mass distribution of the second heavy-neutrino candidate $N^{(2)}$, obtained from the $l_2 j_C j_D$ system.

Figure 4.7: Reconstructed invariant mass distributions of the two heavy-neutrino candidates using the jet-based reconstruction.

The reconstructed masses are smeared with respect to the case of quarks, as expected, since jet reconstruction inevitably incorporates contributions from additional particles.

4.4 Angular distributions and momentum studies for lepton, quark and jet pairings

For the best pairing found by the matching algorithm, several diagnostic quantities are computed to characterise the quality of the truth-level associations and to understand the kinematic properties of the signal decay products. The studies presented in this section are performed on the benchmark mass point $m_N = 50$ GeV and $m_\Delta = 130$ GeV, for which 100000 events are generated. The results for the other mass points are similar.

The angular distance (ΔR) between the two final-state leptons (Fig. 4.8) is peaked approximately at π, meaning that the majority of leptons are produced back-to-back.

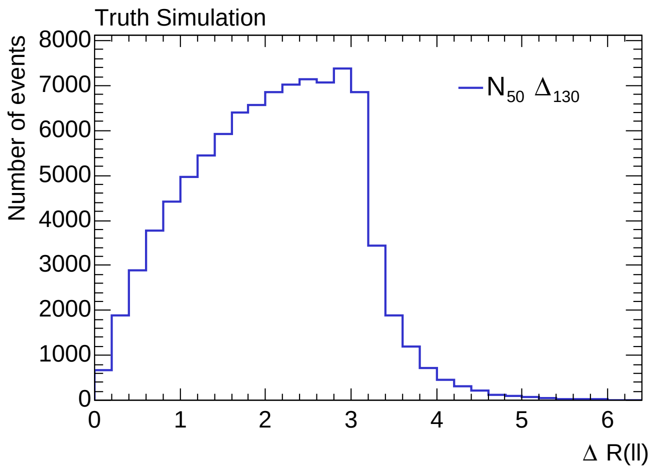

Figure 4.8: Angular distance distribution between the two charged leptons for the benchmark mass point $m_N = 50$ GeV, $m_\Delta = 130$ GeV.

The angular distance between leptons and their associated quarks and jets is also examined for the events passing both the selection of exactly two charged leptons and four quarks and the matching procedure. *Correct* pairings, in which the lepton and the quarks share the same mother particle N, and *wrong* pairings, in which they originate from different N decays are distinguished. The comparison of $\Delta R(l, q)$ (Fig. 4.9a) and $\Delta R(l, \text{jet})$ (Fig. 4.9b) for correct versus wrong pairings validates the matching procedure: correctly associated objects are expected to have smaller angular separations due to their common origin in the same boosted decay system, while incorrect pairings are largely uncorrelated and therefore populate a broader ΔR spectrum.

Specifically, the $\Delta R(l, q)$ distribution is broad and peaks around $\Delta R \simeq 1.5$, confirming that quarks and leptons from the same N decay are not collimated. This is a direct consequence of the isotropic decay topology of a relatively light N produced nearly at rest in the Δ frame: the daughter particles are emitted back-to-back rather than collimated into a single jet-like object.

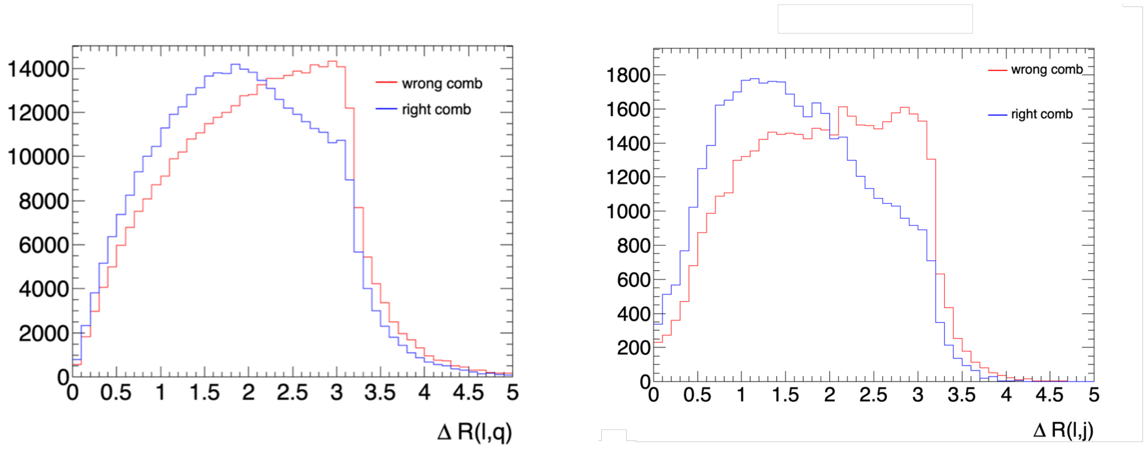

(a) Distribution of $\Delta R(l,q)$ between leptons and their associated quarks for correct (blue) and wrong (red) pairings. No lepton's transverse-momentum cut was applied.

(b) Distribution of $\Delta R(l,\text{jet})$ between leptons and their associated jets for correct (blue) and wrong (red) pairings. No lepton's transverse-momentum cut was applied.

Figure 4.9: Comparison of ΔR distributions for correct and wrong pairings.

As expected, correct pairings peak at lower ΔR values, however, both distributions show a not negligible overlap across the full ΔR range. This overlap implies that $\Delta R(l,q)$ and $\Delta R(l,\text{jet})$ are not suitable as cut-based discriminating variables in a cut-and-count signal region definition, since any threshold would either remove a large fraction of signal events or retain a significant number of wrong pairings. These quantities may however provide discriminating power as input features to the multivariate classifier, where their information can be exploited in combination with other observables.

For each matched quark-jet pair, three more quantities are computed:

- The angular separation $\Delta R(q,\text{jet})$ (Sec. 4.4.1);
- The absolute transverse-momentum difference $\Delta p_{\mathrm{T}} = p_{\mathrm{T}}^{jet} - p_{\mathrm{T}}^{q}$ (Sec. 4.11)
- The relative transverse-momentum difference $\Delta p_{\mathrm{T,rel}} = \frac{(p_{\mathrm{T}}^{jet} - p_{\mathrm{T}}^{q})}{p_{\mathrm{T}}^{q}}$ (Sec. 4.4.3).

These quantities can be used to probe the quality of the jet reconstruction, Jet Energy Scale (JES) and JER at truth-level.

4.4.1 ΔR between truth-quarks and truth-jets

The angular separation $\Delta R(q,\text{jet})$ between each truth-quark and its matched jet (Fig. 4.10) is studied with two different p_{T} thresholds on the matched jets: no p_{T} cut, and $p_{\mathrm{T}}^{\text{jet}} > 20\,\text{GeV}$, for the events passing both the selection of exactly two charged leptons and four quarks and the matching procedure.

The distribution is peaked at small values ($\Delta R \lesssim 0.1$) in both cases, confirming that the ΔR-based matching correctly associates quarks with the nearest jet. The distribution becomes slightly more peaked when requiring $p_{\mathrm{T}}^{\text{jet}} > 20\,\text{GeV}$, as higher-$p_{\mathrm{T}}$ jets are more collimated and carry a larger fraction of the quark's momentum within the cone of radius $R = 0.4$.

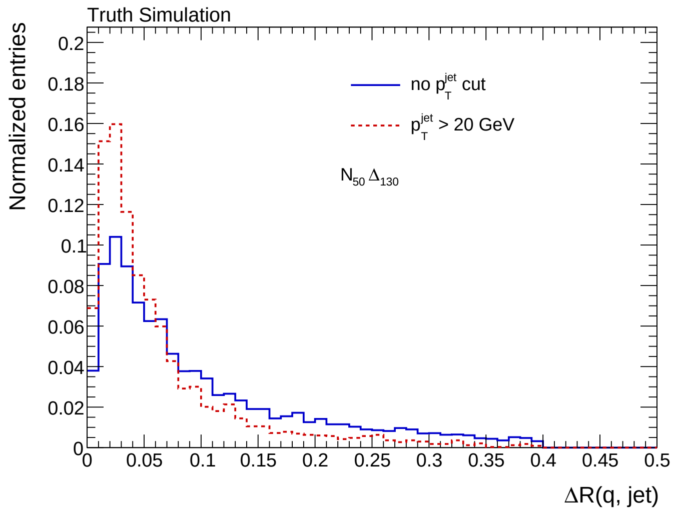

Figure 4.10: Distribution of the angular separation $\Delta R(q, \mathrm{jet})$ between truth-quarks and their matched jets, normalized to unit area, for events passing both the two charged leptons and four quarks selection and jet-matching, for the benchmark mass point $m_N = 50\,\mathrm{GeV}$, $m_\Delta = 130\,\mathrm{GeV}$. The solid blue line shows the distribution with no $p_\mathrm{T}^\mathrm{jet}$ cut, while the dashed red line requires $p_\mathrm{T}^\mathrm{jet} > 20\,\mathrm{GeV}$.

4.4.2 Δp_T between truth-quarks and truth-jets

The transverse-momentum difference $\Delta p_\mathrm{T} = p_\mathrm{T}^\mathrm{jet} - p_\mathrm{T}^q$ between each matched quark-jet pair is shown in Fig. 4.11.

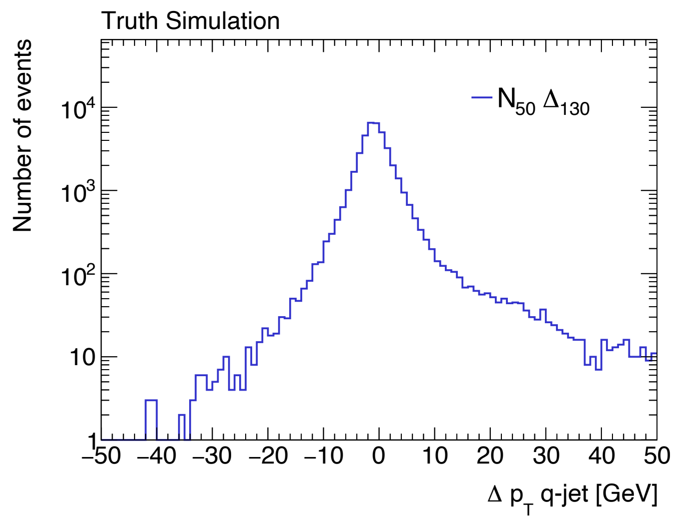

Figure 4.11: Distribution of $\Delta p_\mathrm{T} = p_\mathrm{T}^\mathrm{jet} - p_\mathrm{T}^q$ for matched quark-jet pairs for the benchmark mass point $m_N = 50$,$m_\Delta = 130\,\mathrm{GeV}$, shown in logarithmic scale.

The distribution is centred near zero, with a mean of $\langle \Delta p_\mathrm{T} \rangle \simeq -0.553\,\mathrm{GeV}$. This negative shift is consistent with energy loss outside the jet cone: soft radiation emitted at angles $\Delta R > 0.4$

is not captured by the jet algorithm, so the $p_{\mathrm{T}}^{\mathrm{jet}}$ is systematically lower than the originating quark p_{T}.

4.4.3 Truth-level JER proxy and comparison with ATLAS reco-level results

To characterise the JER at truth level, the relative transverse-momentum difference

$$\Delta p_{\mathrm{T,rel}} = \frac{p_{\mathrm{T}}^{\mathrm{jet}} - p_{\mathrm{T}}^{q}}{p_{\mathrm{T}}^{q}} \tag{4.6}$$

is studied as a function of the quark transverse momentum p_{T}^{q}. The two-dimensional distribution of $\Delta p_{\mathrm{T,rel}}$ versus p_{T}^{q} (Fig. 4.12) shows a strong dependence on p_{T}^{q} at low momenta, with the spread decreasing significantly as p_{T}^{q} increases.

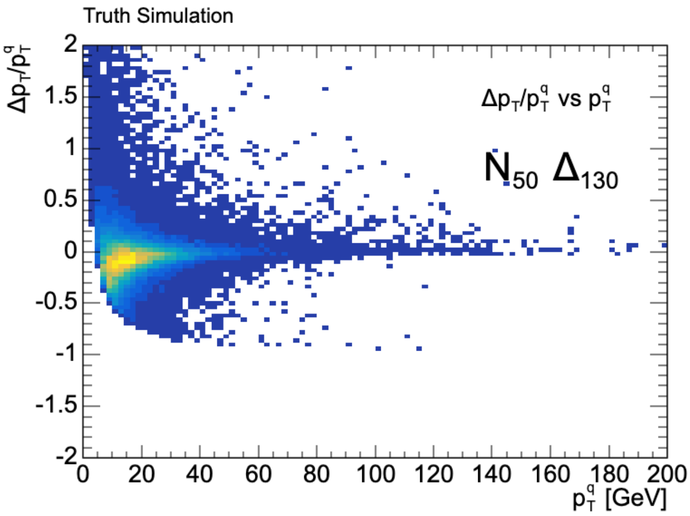

Figure 4.12: Two-dimensional distribution of $\Delta p_{\mathrm{T,rel}} = (p_{\mathrm{T}}^{\mathrm{jet}} - p_{\mathrm{T}}^{q})/p_{\mathrm{T}}^{q}$ as a function of the truth-quark transverse momentum p_{T}^{q}, for the benchmark mass point $m_N = 50\,\mathrm{GeV}$, $m_\Delta = 130\,\mathrm{GeV}$. The colour scale indicates the number of matched quark-jet pairs per bin.

This behaviour is expected: for low-p_{T} quarks, the jet cone of radius $R = 0.4$ captures a larger fraction of soft radiation relative to the quark energy, and detector effects and hadronisation uncertainties are larger, leading to a broader distribution. For higher-p_{T} quarks ($p_{\mathrm{T}}^{q} > 20\,\mathrm{GeV}$), most of the parton energy is contained within the cone and the jet tracks the quark more faithfully.

To extract a quantitative estimate of the JER as a function of p_{T}^{q}, the p_{T}^{q} axis is divided into 10 GeV-wide bins. In each bin, the $\Delta p_{\mathrm{T,rel}}$ distribution is fitted with a Gaussian in the interval $[-1, 1]$. The mean of the Gaussian gives the JES, quantifying the average over- or under-estimation of the quark p_{T} by the reconstructed jet, while the standard deviation σ gives the JER, which measures the fluctuations of the jet response around the mean. The results are summarised in Tab. 4.2 and the σ values as a function of p_{T}^{q} are shown in Fig. 4.13.

Table 4.2: JES (mean) and JER (σ) extracted from Gaussian fits to the $\Delta p_{\mathrm{T,rel}}$ distribution in 10 GeV-wide bins of p_{T}^{q}, for the benchmark mass point $m_N = 50\,\mathrm{GeV}$, $m_\Delta = 130\,\mathrm{GeV}$. The fit is performed over the range $\Delta p_{\mathrm{T,rel}} \in [-1, 1]$. The fit fails for the last bin [90, 100] GeV, which is thus excluded for the JER interpretation.

p_{T}^{q} **bin** [GeV]	**JES (mean)**	**JER** (σ)	**Entries**
[0, 10]	-0.0278 ± 0.0040	0.2076 ± 0.0028	8417
[10, 20]	-0.0955 ± 0.0017	0.2013 ± 0.0018	15921
[20, 30]	-0.0395 ± 0.0016	0.1246 ± 0.0020	7341
[30, 40]	-0.0164 ± 0.0017	0.0906 ± 0.0021	3318
[40, 50]	-0.0002 ± 0.0024	0.0788 ± 0.0028	1381
[50, 60]	$+0.0061 \pm 0.0034$	0.0687 ± 0.0039	660
[60, 70]	$+0.0103 \pm 0.0032$	0.0546 ± 0.0031	372
[70, 80]	$+0.0158 \pm 0.0053$	0.0540 ± 0.0073	218
[80, 90]	$+0.0376 \pm 0.0122$	0.0723 ± 0.0121	131

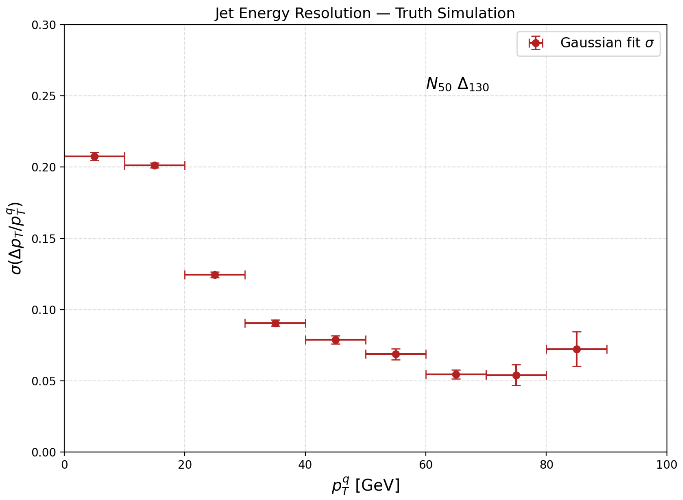

Figure 4.13: Gaussian σ of the $\Delta p_{\mathrm{T,rel}}$ distribution as a function of p_{T}^{q}, extracted from Gaussian fits to vertical slices of the 2D distribution shown in Fig. 4.12, for the benchmark mass point $m_N = 50\,\mathrm{GeV}$, $m_\Delta = 130\,\mathrm{GeV}$. The vertical error bars represent the fit uncertainty on σ.

The negative JES values observed at low p_{T}^{q} confirm that the jet systematically experiments energy loss outside the cone. The JES turns slightly positive at $p_{\mathrm{T}}^{q} > 50\,\mathrm{GeV}$, suggesting that at higher momenta additional soft radiation from the underlying event partially compensates for the out-of-cone losses.

The resolution improves from approximately 20% at $p_{\mathrm{T}}^{q} \simeq 10\,\mathrm{GeV}$ to approximately 5% at $p_{\mathrm{T}}^{q} \simeq 70\,\mathrm{GeV}$, consistent with the expected improvement of jet energy resolution with increasing jet p_{T} [114]. This improvement reflects the better reconstruction quality for higher-p_{T} jets, consistent with the expectation that the anti-k_t jet algorithm with $R = 0.4$ provides a more faithful representation of the originating parton when the quark momentum is large enough that most of the radiation is captured within the cone.

This approximated 20% truth-level p_{T} resolution directly translates into a broadening of the invariant mass difference Δm_{ljj} reconstructed with jets compared to the truth-quark-level quantity, which is indeed observed when comparing the two distributions (Fig. 4.4 and Fig. 4.6). The degradation of the Δm_{ljj} resolution at truth level therefore sets a lower bound on the discriminating power of this variable in the full reconstruction-level analysis and motivates the use of multivariate techniques that can exploit correlated information from multiple observables simultaneously, rather than relying on a single cut on Δm_{ljj}.

The truth-level JER proxy derived here is qualitatively consistent with the ATLAS reconstruction-level JER measurements, which report similar trends of improving resolution with increasing jet p_{T} and a resolution of $O(20\%)$ at low p_{T} [115]. The absolute values differ because the truth-level study does not include detector simulation, pile-up, or in-situ calibration corrections, all of which modify the jet response at reconstruction level.

Chapter 5

Event selection strategies and expected signal strength

The signal truth-level MC studies, described in Chap. 4, allowed the understanding of the limits of the current analysis strategy. A sensitivity study is then carried out to aid an event selection, which enhances the signal selection efficiency. For each selection studied, Scale Factors (SFs) are computed to quantify the expected improvement of the signal selection efficiency (Sec. 5.1). A SF is defined as the ratio of the signal event yield (or background yield) obtained with the proposed selection to that of the baseline analysis described in Sec. 3.2, providing a direct measure of the improvement introduced by each selection configurations. To reproduce the effects of detector resolution at reconstruction level, leptons and jets p_{T} are also smeared according to the ATLAS reconstruction efficiency (Sec. 5.1.4).

The improvement in sensitivity is quantified through the expected signal strength $\hat{\mu}$, estimated with the TRExFitter [109] profile likelihood framework described in Sec. 3.2.4. The expected signal strength is then compared between the proposed selection and the baseline analysis to assess the gain in sensitivity (Sec. 5.2). The aim of this study is to provide an approximate estimate of the increase in signal strength which could allow to set a 95% C.L. exclusion limit, if excesses are not found.

In this chapter, a benchmark mass point $m_N = 50\,\mathrm{GeV}$ and $m_\Delta = 130\,\mathrm{GeV}$ is initially studied as a reference. Then, additional mass points including $m_N = [30, 40, 45, 50]$ GeV and $m_\Delta \in [110, 120, 130, 140, 150]$ GeV are considered to compute the expected sensitivity.

5.1 Selection efficiency studies

The selection efficiency studies are performed evaluating both the signal and background events selection efficiency. Different cuts on the minumim p_{T} of the final state leptons, dictated by the ATLAS single lepton and dilepton triggers, are reproduced at truth-level and the different event yields are computed. The single lepton triggers that are mentioned are reported in Tab. 5.1 for electrons and muons respectively.

Trigger type	Trigger name	Threshold	Years used
Single electron	`e26_lhtight_nod0_ivarloose`	$E_T > 26$ GeV	2016*–2018
Single muon	`HLT_mu26_ivarmedium`	$p_T > 26$ GeV	2016–2018

Table 5.1: Single-lepton triggers used in ATLAS Run 2. For electrons [104], the trigger name encodes the E_T threshold, the identification working point (`lhtight`), the absence of a transverse impact parameter cut (`nod0`) and the isolation requirement (`ivarloose`). For muons [103], the prefix `HLT_mu` is followed by the p_T threshold in GeV and the isolation working point (`ivarmedium`). Both triggers correspond to the lowest-threshold unprescaled single-lepton chains used as primary triggers for the majority of the 2016-2018 ATLAS Run 2 data-taking period. *For the single-electron trigger, the E_T threshold was 24 GeV during 2015 and most of 2016, raised to 26 GeV only at the end of 2016, remaining at this value throughout 2017 and 2018. In 2015,lower thresholds also for the muon case were supported.

The SFs are defined as

$$\mathrm{SF} = \frac{N_{\mathrm{sel}}}{N_{\mathrm{sym}}} \tag{5.1}$$

where N_{sym} denotes the number of events passing the symmetric requirement $p_{\mathrm{T}}(l) > 18$ GeV on both leptons, exploited in the baseline analysis (Sec. 3.2.1), while N_{sel} is the number of events passing the alternative selection. The SFs therefore provide an estimate of the variation in event selection efficiency between the alternative strategy and the baseline analysis choice. A SF > 1 indicates that the chosen selection enhances the acceptance of the signal or background events with respect to the baseline.

A first preliminary check is performed counting the number of events for a reference sample with no requirement on lepton p_{T}. Then, three lepton p_{T} selection scenarios are considered:

- A **symmetric** selection, requiring $p_{\mathrm{T}}^{l} > 18$ GeV on both leptons, consistent with the dilepton trigger thresholds used in the baseline analysis.
- An **asymmetric** selection motivated by the ATLAS Run 2 single-lepton trigger threshold, requiring either $p_{\mathrm{T}}(l_{\mathrm{leading}}) > 26$ GeV and $p_{\mathrm{T}}(l_{\mathrm{subleading}}) > 5$ GeV. The softer requirements of 5 GeV reflects the minimum offline threshold needed to ensure a reliable lepton reconstruction and identification. This selection will be identified as selection **A**, for semplicity.
- A logic **OR** of the symmetric and asymmetric trigger requirements. This selection will be identified as selection **B**.

In all cases, jets are required to satisfy $p_{\mathrm{T}}^{\mathrm{jet}} > 20$ GeV; the case $p_{\mathrm{T}}^{\mathrm{jet}} > 15$ GeV, is reported in App. B.2 for completeness, testing the possibility to use an alternative jet reconstruction algorithm with a lower p_{T} threshold.

The SFs are computed selecting events which contain at least two jets, to provide an inclusive estimate which can be applied to all the SRs described in Sec. 3.2.2. The signal event yields and SFs for the benchmark mass point $m_N = 50$ GeV, $m_\Delta = 130$ GeV are summarised in Tab. 5.2.

The statistical uncertainties on the individual SFs are estimated by propagating the Poisson uncertainty on the underlying event counts. Given the definition for SF (Eq.5.1), where N_{sel} is the number of events passing the selection A or B and N_{symm} is the number of events passing the symmetric selection, the relative uncertainty on each SF is given by

$$\frac{\sigma_{\text{SF}}}{\text{SF}} = \sqrt{\frac{1}{N_{\text{sel}}} + \frac{1}{N_{\text{symm}}}} \tag{5.2}$$

where the two terms are combined in quadrature assuming Poisson-distributed event counts.

Table 5.2: Signal event yields and SFs with relative unvertanties for different lepton p_{T} selection scenarios, for events with at least two jets with $p_{\text{T}}^{\text{jet}} > 20\,\text{GeV}$, for the benchmark mass point $m_N = 50\,\text{GeV}$, $m_\Delta = 130\,\text{GeV}$. The percentage is done with respect to the total generated events (100000).

Selection	**Events**	**SF**
No lepton p_{T} cut	67.71%	–
Symmetric: $p_{\text{T}}^{l_{1,2}} > 18\,\text{GeV}$	12.83%	1.000
Asymmetric: $p_{\text{T}}(l_{\text{leading}}) > 26\,\text{GeV}$, $p_{\text{T}}(l_{\text{subleading}}) > 5\,\text{GeV}$ (A)	26.52%	2.068 ± 0.022
OR of symmetric and asymmetric (B)	28.45%	2.218 ± 0.024

The asymmetric selection yields approximately twice the number of signal events with respect to the symmetric baseline, while the OR of the two selections further increases the yield, reaching SF $\simeq 2.2$. This improvement is physically understood by noting that the signal topology involves a lepton p_{T} spectrum that peaks well below the 18 GeV symmetric threshold (Fig. 5.1).

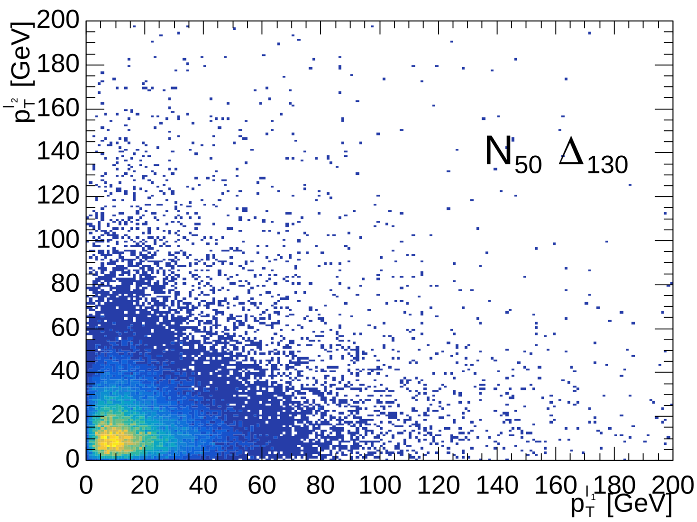

Figure 5.1: Two-dimensional distribution of the leptons transverse momenta, $p_{\text{T}}^{l_1}$ vs. $p_{\text{T}}^{l_2}$, at truth-level for the signal benchmark $m_N = 50\,\text{GeV}$, $m_\Delta = 130\,\text{GeV}$ and $p_{\text{T}}^{\text{jet}} > 20\,\text{GeV}$. The majority of the signal events populates the region $p_{\text{T}} \lesssim 18\,\text{GeV}$.

The OR requirement recovers precisely some of these soft-lepton events (Fig. 5.2), therefore representing the optimal selection strategy which is carried forward in the subsequent sensitivity study.

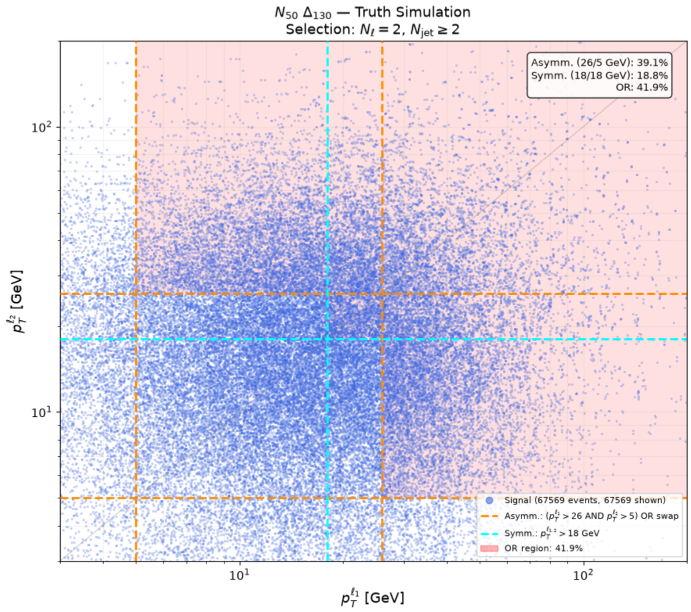

Figure 5.2: Distribution of the two leptons transverse momenta, $p_{\rm T}^{l_1}$ vs. $p_{\rm T}^{l_2}$, in logarithmic scale, for the signal sample for the benchmark mass point $m_N = 50\,\text{GeV}$, $m_\Delta = 130\,\text{GeV}$, requiring exactly two leptons and at least two jets with $p_{\rm T}^{\rm jet} > 20\,\text{GeV}$ ($N_l = 2$, $N_{\rm jet} \geq 2$). The shaded red region indicates the OR of the two lepton $p_{\rm T}$ selection criteria. The orange dashed lines mark the asymmetric thresholds ($p_T^{l_1} > 26\,\text{GeV}$ and $p_T^{l_2} > 5\,\text{GeV}$, or vice versa) and the cyan dashed lines mark the symmetric threshold ($p_T^{l_{1,2}} > 18\,\text{GeV}$).

The OR selection retains 41.9% of signal events (the percentage is done with respect to the total events that passed the selection of two leptons and at least two jets, $N_l = 2$, $N_{\rm jet} \geq 2$, with $p_{\rm T}^{\rm jet} > 20\,\text{GeV}$ with no lepton $p_{\rm T}$ cut), with 39.1% passing the asymmetric selection and 18.8% the symmetric one.

5.1.1 Scale factors for background

The same SFs study is performed independently on the main SM backgrounds: DY, diboson, $t\bar{t}$ and other (other top and single top events). Considering that this study cannot be performed for the misidentified leptons contribution, it is chosen to conservatively apply the highest SF obtained for the backgrounds (Tab. 5.3).

Table 5.3: SFs and relative uncertanties for A and B selections for each background sample and $p_T^{\text{jet}} > 20\,\text{GeV}$.

Background	**A**	**B**
Diboson	1.227 ± 0.005	1.238 ± 0.005
Drell-Yan	1.215 ± 0.004	1.224 ± 0.004
Mis-ID lept.	1.234 ± 0.008	1.254 ± 0.008
Other	1.224 ± 0.008	1.235 ± 0.008
$t\bar{t}$	1.234 ± 0.008	1.254 ± 0.008

For all the background processes, the SFs are approximately 1.22–1.23. The comparison of these values with the ones found for the signal (Tab. 5.2) indicates that the signal yield increase is higher than the number of selected background events.

Fig. 5.3 shows the overlap between the lepton kinematic distribution of the signal sample and that of the various background processes, in the $p_{\mathrm{T}}^{l_1}$ vs. $p_{\mathrm{T}}^{l_2}$ plane. This allows a visual assessment of how effectively the lepton p_T selections (both symmetric and asymmetric, indicated by the dashed lines) discriminate the signal from the backgrounds in the kinematic region of interest. The same plot in logarithmic scale, useful to better appreciate the event density at low p_{T}, is shown in App. B.3.

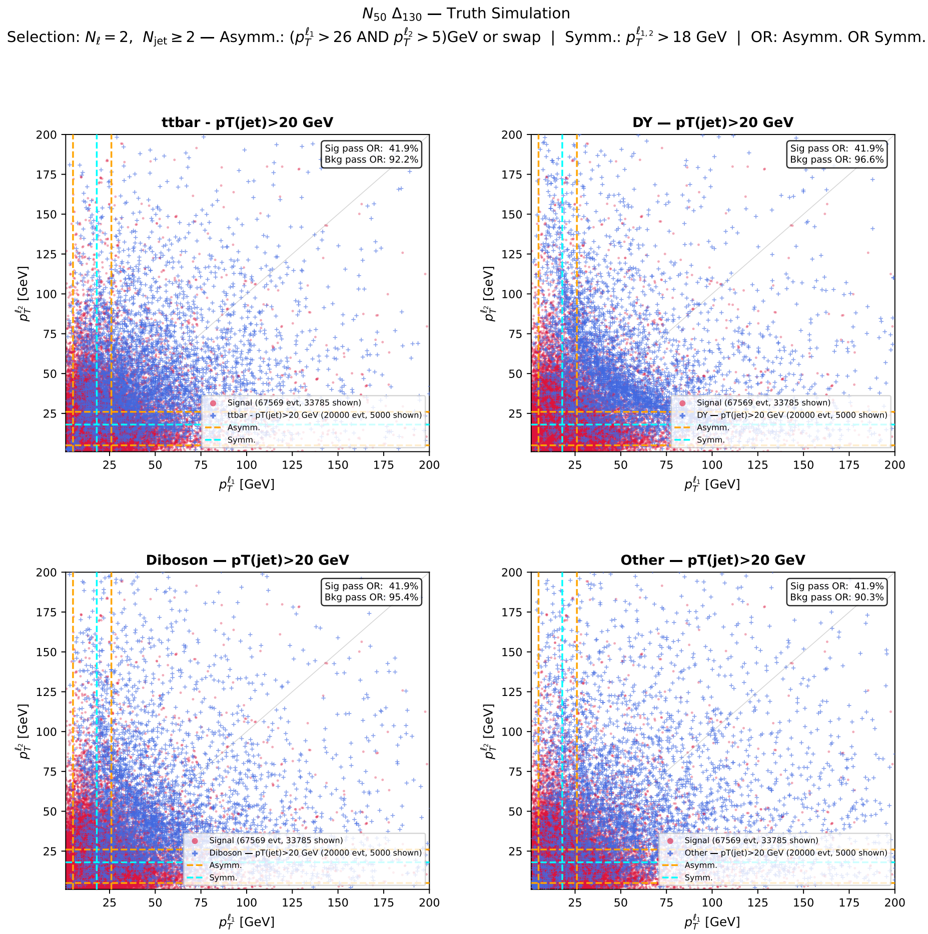

Figure 5.3: Overlap, in the $p_T^{l_1}$ vs. $p_T^{l_2}$ plane, between the distributions of the signal sample ($m_N = 50\,\text{GeV}$, $m_\Delta = 130\,\text{GeV}$, red circles) and that of the four SM background samples considered (blue crosses). The signal distribution is obtained from the truth-level MC sample requiring exactly $N_l = 2$ and $N_{\text{jet}} \geq 2$ with $p_T > 20\,\text{GeV}$. The dashed lines indicate the lepton p_T trigger thresholds used in the selection: orange for the asymmetric selection (A) and cyan for the symmetric selection ($p_T^{l_{1,2}} > 18\,\text{GeV}$).

As can be observed, the background p_T distributions are centered at higher values with respect to the signal events. From these studies is therefore observed that accepting also final-state subleading leptons with a lower p_T, increases more the signal yield with respect to all the main background processes.

5.1.2 Scale factors for data

The data yield N is computed as

$$N = Y_{\text{Dib}} \cdot \text{SF}_{\text{Dib}} + Y_{t\bar{t}} \cdot \text{SF}_{t\bar{t}} + Y_{\text{DY}} \cdot \text{SF}_{\text{DY}} + Y_{\text{MisID}} \cdot \text{SF}_{\text{highest}} + Y_{\text{Other}} \cdot \text{SF}_{\text{Other}} \tag{5.3}$$

where Y_{Dib}, $Y_{t\bar{t}}$, Y_{DY}, Y_{MisID} and Y_{Other} are the MC expected yields for each background process in the given analysis region, reported in Tab. B.1 and SF_{Dib}, $\text{SF}_{t\bar{t}}$, SF_{DY}, $\text{SF}_{\text{highest}}$ and SF_{Other} are the corresponding scale factors derived for each background process.
Both the MC expected yields (Y_i) and the background SFs (SF_i) carry statistical uncertainties.

The uncertainty on N is therefore obtained by standard error propagation including both contributions from Y_i and SF_i:

$$\sigma_N^2 = \sum_i (\mathrm{SF}_i \sigma_{Y_i})^2 + \sum_i (Y_i \sigma_{\mathrm{SF}_i})^2. \tag{5.4}$$

The overall data scale factor is then defined as

$$\mathrm{SF}_{\mathrm{data}} = \frac{N_{\mathrm{expected}}}{N}, \tag{5.5}$$

where $N_{\mathrm{expected}} = \sum_i Y_i$ is the total event yield expected from the MC simulation in that region, which also carries a statistical uncertanty. The uncertainty on $\mathrm{SF}_{\mathrm{data}}$ is thus obtained by propagating the uncertainties on both N_{expected} and N

$$\frac{\sigma(\mathrm{SF}_{\mathrm{data}})}{\mathrm{SF}_{\mathrm{data}}} = \sqrt{\left(\frac{\sigma_{N_{\mathrm{expected}}}}{N_{\mathrm{expected}}}\right)^2 + \left(\frac{\sigma_N}{N}\right)^2} \tag{5.6}$$

The SFs for data with their uncertanties are reported in Tab. 5.4.

Table 5.4: SFs and their relative uncertanties for data in each analysis region and $p_T^{\mathrm{jet}} > 20$ GeV for A and B selections.

Region	**A**	**B**
MLDYCR	1.215 ± 0.005	1.224 ± 0.005
MLDYVR	1.215 ± 0.005	1.224 ± 0.005
MLTopCR	1.233 ± 0.007	1.253 ± 0.007
MLTopVR	1.231 ± 0.006	1.251 ± 0.006
MLDBCR	1.223 ± 0.006	1.236 ± 0.006
MLDBVR	1.226 ± 0.007	1.241 ± 0.007
MLSR2J	1.227 ± 0.007	1.243 ± 0.007
MLSR3J	1.229 ± 0.007	1.246 ± 0.007
MLSR4J	1.230 ± 0.007	1.247 ± 0.007

The resulting SFs are stable across all regions (defined in Sec. 3.2.2), with values around 1.21–1.25.

5.1.3 Scale factors for different signal mass hypotheses

Different mass hypotheses are included in order to compute the exclusion limits. The obtained SFs, computed as described in Sec. 5.1, are reported in Tab. 5.5.

Table 5.5: SFs and their relative uncertanties for different mass hypotheses for A and B selections and $p_T^{\text{jet}} > 20\,\text{GeV}$.

(m_N, m_Δ) [GeV]	**A**	**B**
(50,150)	2.000 ± 0.019	2.118 ± 0.020
(50,140)	2.017 ± 0.020	2.154 ± 0.021
(50,130)	2.050 ± 0.022	2.202 ± 0.023
(50,120)	2.013 ± 0.024	2.181 ± 0.025
(50,110)	1.887 ± 0.024	2.070 ± 0.026
(30,110)	2.407 ± 0.032	2.570 ± 0.034
(40,110)	2.291 ± 0.031	2.452 ± 0.032
(45,110)	2.152 ± 0.028	2.320 ± 0.030

The distributions of the SFs for all the mass points considered are shown in Fig. 5.4.

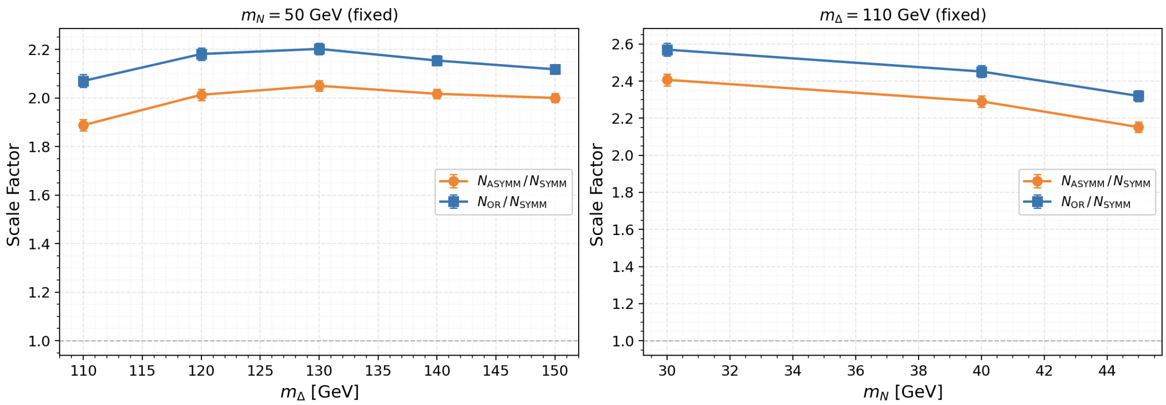

Figure 5.4: Distributions of SFs for different mass hypotheses for A (blue) and B (orange) selections, as a function of m_N or m_Δ, for $p_{\text{T}}^{\text{jet}} > 20\,\text{GeV}$, with relative uncertanty bands. Left: SFs for the mass points with $m_N = 50\,\text{GeV}$ fixed as a function of m_Δ. Right: SFs for the mass points with $m_\Delta = 110\,\text{GeV}$ fixed as a function of m_N.

5.1.4 Scale factors consistency

The SFs presented in the previous sections are derived from truth-level MC information, where the four-momenta of leptons and jets are known exactly. In a realistic experimental environment, however, reconstructed objects are affected by the finite detector resolution, which can modify the efficiency of selections based on transverse-momentum thresholds, related to the ATLAS Run 2 triggers.

To estimate the impact of detector effects on the extracted SFs, a simplified reconstruction-level study is performed. The transverse momentum of each truth-level object is smeared according to

$$p_{\text{T}}^{\text{reco}} = p_{\text{T}}^{\text{truth}}\,(1 + G(0, \sigma(p_{\text{T}}))) \tag{5.7}$$

where $G(0, \sigma(p_{\text{T}}))$ is a Gaussian random variable with zero mean and relative width $\sigma(p_{\text{T}})$. The smearing is applied independently to each object in each event and the event yields for each selection are computed using final state smeared p_{T} values. The SFs resulting from this procedure therefore provide a more reliable estimate of the sensitivity of the analysis, taking into account the effects of the finite detector resolution.

The purpose of this study is not to reproduce the full ATLAS detector response. Effects such as reconstruction efficiencies, fake objects, flavour-tagging performance, acceptance losses and non-Gaussian resolution tails are not included. Instead, the procedure is designed to reproduce the dominant effect relevant to this analysis, that can modify the number of events passing the different signal selection configurations.

The spectra for leptons and jet p_{T}, together with the Δm_{lqq} and Δm_{ljj} distributions, comparing smeared and truth-level scenarios, are reported in App. A.3.

Jet momentum resolution

Jets are expected to provide the largest reconstruction uncertainty. Since the signal topology contains several low-p_{T} jets close to the 20 GeV selection threshold, it is expected that even with a small smearing on $p_{\mathrm{T}}^{\mathrm{jet}}$, the number of events passing the different selections can vary. The jet momentum resolution [114] is given by the quadrature sum

$$\frac{\sigma(p_{\mathrm{T}})}{p_{\mathrm{T}}} = \frac{N}{p_{\mathrm{T}}} \oplus \frac{S}{\sqrt{p_{\mathrm{T}}}} \oplus C \tag{5.8}$$

where N is a noise term (electronic noise and pile-up, dominant for $p_{\mathrm{T}} < 30$ GeV), S is a stochastic term related to the sampling nature of the calorimeters (dominant at intermediate p_{T}) and C is a constant term arising from non-uniformities and calibration residuals (dominant for $p_{\mathrm{T}} > 400$ GeV). The parametrisation used in this work follows from a fitting procedure with the aim of reproducing the overall behaviour observed in Fig. 5.5a and following Ref. [114], the coefficients N, S, C have been assigned with the following values: $N = 2.2$, $S = 0.8$ and $C = 0.05$.

In Fig. 5.5 two different jet calibration schemes are shown: *EM+JES* jets are reconstructed from topo-clusters built at the electromagnetic (EM) energy scale, which measures the energy deposited by electromagnetically interacting particles, excluding hadrons. A Jet Energy Scale (JES) calibration sequence is then applied to correct for the hadronic response and other effects. *PFlow+JES* jets instead use the ATLAS Particle-Flow (PFlow) reconstruction method, which combines charged-particle tracks from the ID with topo-clusters, exploiting the better momentum resolution of the tracker for low-p_{T} charged hadrons. The resulting jets are calibrated with a JES sequence [114]. The momentum resolution is dependent on both p_{T} and η. Nevertheless, as can be seen from Fig. 5.5b, the distribution of the JER as a function of η is almost flat. This dependence is therefore neglected and the same resolution is considered for all the η values in this study case.

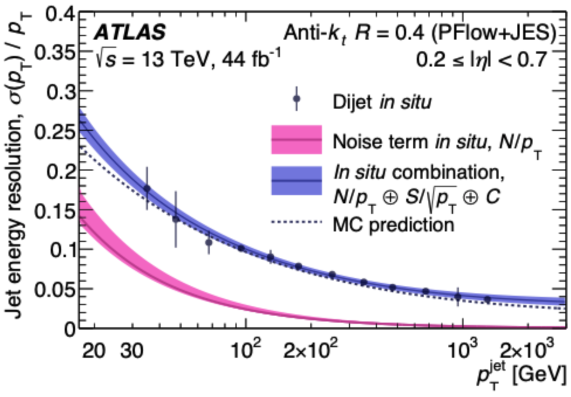

(a) Relative JER as a function of $p_{\mathrm{T}}^{\mathrm{jet}}$ for PFlow+JES jets, showing the measured in-situ resolution and its decomposition into stochastic, noise and constant terms.

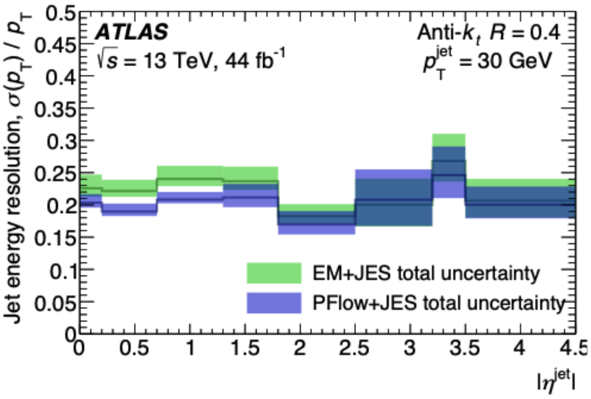

(b) Relative JER as a function of $|\eta^{\mathrm{jet}}|$ evaluated at $p_{\mathrm{T}} = 30\,\mathrm{GeV}$, comparing PFlow+JES and EM+JES calibration schemes, including total systematic uncertainties.

Figure 5.5: Relative JER computed by ATLAS with Run 2 data [114].

Leptons momentum resolution

For the **muons** momentum reconstruction, the ATLAS Experiment exploits the information from both the MS and ID to reconstruct the muons arising from the primary vertex [116]. Therefore the relative momentum resolution is given by the quadrature sum

$$\frac{\sigma(p_{\mathrm{T}})}{p_{\mathrm{T}}} = \frac{\sigma(p_{\mathrm{T}})_{\mathrm{ID}}}{p_{\mathrm{T}}} \oplus \frac{\sigma(p_{\mathrm{T}})_{\mathrm{MS}}}{p_{\mathrm{T}}} \tag{5.9}$$

where

$$\frac{\sigma(p_{\mathrm{T}})_{MS}}{p_{\mathrm{T}}} = \frac{p_0^{MS}}{p_{\mathrm{T}}} \oplus p_1^{MS} \oplus p_2^{MS} \cdot p_{\mathrm{T}} \tag{5.10}$$

for a fixed value of η, with $p_0^{MS}, p_1^{MS}, p_2^{MS}$ the coefficients related to the energy loss in the calorimeter, multiple scattering and intrinsic resolution terms, respectively. The term $\frac{\sigma(p_{\mathrm{T}})_{\mathrm{ID}}}{p_{\mathrm{T}}}$ is defined as

$$\frac{\sigma(p_{\mathrm{T}})_{ID}}{p_{\mathrm{T}}} = p_1^{ID} \oplus p_2^{ID} \cdot p_{\mathrm{T}} \tag{5.11}$$

for $|\eta| < 1.9$, where p_1^{ID}, p_2^{ID} are the coefficients related to multiple scattering and intrinsic resolution. For for $|\eta| > 1.9$ it is instead

$$\frac{\sigma(p_{\mathrm{T}})_{ID}}{p_{\mathrm{T}}} = p_1^{ID} \oplus p_2^{ID} \cdot p_{\mathrm{T}} \frac{1}{\tan^2\theta} \tag{5.12}$$

where θ is the polar angle with respect to the beam line.

Considering that, in this analysis case, the final state signal muons are predominantly produced with $p_{\mathrm{T}} < 100\,\mathrm{GeV}$, the momentum resolution is well described by the ID contribution alone. In fact, as shown in Fig. 5.6, the combined muon resolution follows closely the ID parametrisation in this p_{T} regime, while the MS provides a significant improvement only at higher transverse momenta.

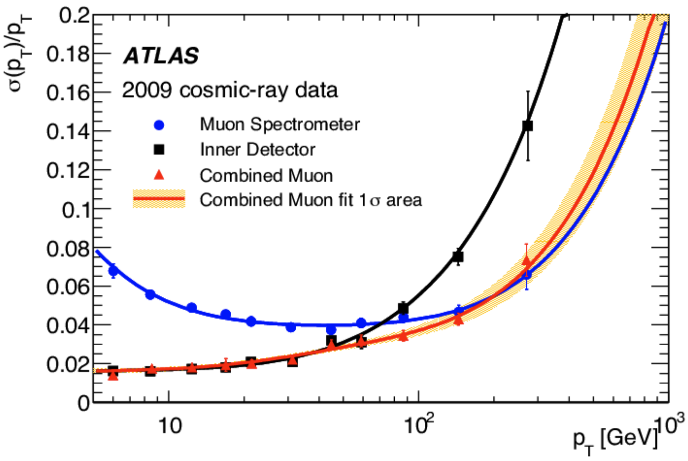

Figure 5.6: Relative momentum resolution as a function of p_T for ID and MS standalone tracks and for CB (Sec. 3.1.1) tracks. The shaded region shows the $\pm 1\sigma$ region of the fit to the resolution curve for the CB tracks [117].

For this reason, in the smearing procedure it is assumed that

$$\frac{\sigma(p_\mathrm{T})}{p_\mathrm{T}} \approx \frac{\sigma(p_\mathrm{T})_\mathrm{ID}}{p_\mathrm{T}} \tag{5.13}$$

The values of the coefficients for the ID are reported in Tab. 5.6.

Table 5.6: Coefficients for the ID momentum resolution parametrisation, extracted from muon momentum resolution measurements in the four η regions of the ATLAS detector: barrel ($|\eta| < 1.05$), transition ($1.05 < |\eta| < 1.7$), end-caps ($1.7 < |\eta| < 2.5$) and CSC/No-TRT ($2.5 < |\eta| < 2.7$)[118].

η region	p_1^{ID} (%)	p_2^{ID} (TeV^{-1})
barrel	1.55 ± 0.01	0.417 ± 0.011
transition	2.55 ± 0.01	0.801 ± 0.567
end-caps	3.32 ± 0.02	0.985 ± 0.019
CSC/No-TRT	4.86 ± 0.22	0.069 ± 0.003

For **electrons**, the relative energy resolution is parametrised in Eq. 2.7 and is composed of three terms: a, the sampling term, b, the noise term and c, the constant term, where b and c both depend on η. The first term of Eq. 2.7 dominates at low energies and its designed value is approximately $\frac{(9\text{–}10)\%}{\sqrt{E}}$ at low η. The noise term is approximately 350 $\cosh\eta$ MeV for a 3×7 cluster in $\eta\times\phi$ space in the barrel at $\langle\mu\rangle = 20$ bunch crossing, and is dominated by pile-up noise at high $|\eta|$. At higher energies, the resolution tends asymptotically to c, with a design value of 0.7% [119]. The applied coefficients in this analysis case are therefore $a = 0.1$, $b = 0.35$ and $c = 0.007$, which reproduce approximately the distribution of $\sigma(E)/E$ as a function of E_T shown in Fig. 5.7.

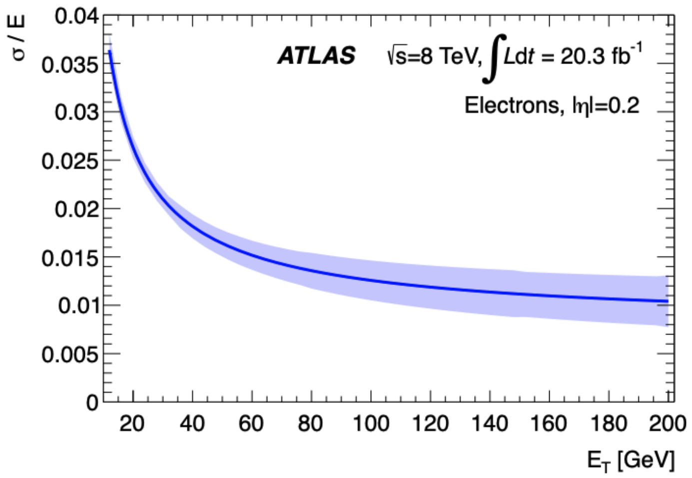

Figure 5.7: Distribution of $\sigma(E)/E$ and its uncertainty band as a function of E_{T} for electrons with $|\eta| = 0.2$ [119].

Results for signal and background smeared SFs

The SFs computed with the smeared lepton and jet p_{T} are reported in Tab. 5.7, alongside the corresponding non-smeared values for all the mass hypotheses.

The ratio R $= \frac{\mathrm{SF}_{\text{Non-smeared}}}{\mathrm{SF}_{\text{Smeared}}}$ provides a proxy for the impact of the simulated detector resolution effects: if R $\simeq$ 1, this indicates that the truth-level $\mathrm{SF}_{\text{Non-smeared}}$ is a reliable proxy for the reconstruction-level efficiency gain and that the improvement in the signal yield observed at truth-level is expected to be preserved once the "reconstructed" quantities are considered. R $\ll$ 1 indicates instead that the inclusion of the detector resolution effects would negatively affect the results obtained at truth-level.

For the ratio R, the uncertainties on the non-smeared and smeared SFs are combined in quadrature, since the two are computed from independent event counts:

$$\frac{\sigma_R}{R} = \sqrt{\frac{1}{N_{\text{sel}}^{\text{non-smeared}}} + \frac{1}{N_{\text{symm}}^{\text{non-smeared}}} + \frac{1}{N_{\text{sel}}^{\text{smeared}}} + \frac{1}{N_{\text{symm}}^{\text{smeared}}}} \tag{5.14}$$

The ratios reported in the last two columns of Tab. 5.7 are all consistent with unity within statistical uncertainties, which are of the order of 1-3%. This confirms that the Gaussian smearing procedure does not introduce any significant systematic bias in the selection efficiency and that the non smeared SFs can be used as a reliable approximation.

	SF$_{\text{Smeared}}$		**R**	
$(m_N,\, m_\Delta)$ [GeV]	**A**	**B**	**A**	**B**
(50, 150)	1.996 ± 0.019	2.113 ± 0.020	1.002 ± 0.013	1.002 ± 0.013
(50, 140)	2.024 ± 0.020	2.158 ± 0.021	0.997 ± 0.014	0.998 ± 0.014
(50, 130)	2.046 ± 0.022	2.196 ± 0.023	1.002 ± 0.015	1.002 ± 0.015
(50, 120)	2.014 ± 0.023	2.187 ± 0.025	0.999 ± 0.016	0.997 ± 0.016
(50, 110)	1.878 ± 0.024	2.067 ± 0.026	1.005 ± 0.018	1.001 ± 0.018
(30, 110)	2.399 ± 0.032	2.560 ± 0.034	1.003 ± 0.019	1.004 ± 0.019
(40, 110)	2.299 ± 0.030	2.465 ± 0.032	0.997 ± 0.019	0.995 ± 0.019
(45, 110)	2.147 ± 0.028	2.316 ± 0.030	1.002 ± 0.019	1.002 ± 0.018

Table 5.7: Signal SFs and relative uncertainties after Gaussian smearing of lepton and jet p_{T} for different mass hypotheses for A and B selection with $p_T^{\text{jet, smeared}} > 20$ GeV. The last two columns report the ratio between SF$_{\text{Non-smeared}}$ and SF$_{\text{Smeared}}$ for each selection configuration, with the associated statistical uncertainties.

Following the same procedure, also the SFs for the different backgrounds are computed and reported in Tab. 5.8.

Table 5.8: Background SFs and relative uncertainties after Gaussian smearing of lepton and jet p_{T} for different mass hypotheses for A and B selections with $p_{\mathrm{T}}^{\text{jet, smeared}} > 20$ GeV.

Background	**A**	**B**
Diboson	1.229 ± 0.005	1.242 ± 0.005
Drell-Yan	1.218 ± 0.004	1.227 ± 0.004
Mis-ID lept.	1.236 ± 0.008	1.257 ± 0.008
Other	1.226 ± 0.008	1.237 ± 0.008
$t\bar{t}$	1.236 ± 0.008	1.257 ± 0.008

As a final consideration, it is important to underline that this smearing study constitutes only a cross-check of the robustness of the truth-level results, not a replacement for a full reconstruction-level analysis. Such a study is beyond the scope of this thesis, but represents a natural step further in the development of this analysis.

5.2 Fit and expected sensitivity

The SFs found provide a first direct measure of the gain introduced by the alternative lepton p_{T} selections. However they do not, by themselves, translate into a statement about sensitivity. To quantify whether the optimised selection is sufficient to exclude a given mass hypothesis at 95% CL, a profile likelihood fit is performed.

The expected signal strength $\hat{\mu}$, is defined as the ratio of the signal cross-section upper limit to the theoretical prediction: a value of $\hat{\mu} < 1$ at 95% CL indicates that the the achieved sensitivity is sufficient to exclude the signal with that confidence level.

In the exclusion fit, the ML score is used as the Parameter Of Interest (POI). For each hypothesised signal mass point, an independent fit is performed and a value of μ is found.

Considering that the analysis is a search for a BSM process, a blinding procedure is adopted. Asimov data[1] are used in the SRs, therefore, the observed yields are taken to be equal to the expected background yields under the background-only hypothesis. The expected $\pm 1\sigma$ and $\pm 2\sigma$ confidence bands for the signal strength parameter μ are also computed.

The SFs computed with the selection configurations A and B are applied as overall rescaling factors to the input histograms of each process, approximating the change in event yield that would result from adopting the alternative selection configurations. The rescaled histograms (two-bin distributions of the ML score for each analysis region) are then passed to TRExFitter [109], which performs the profile likelihood fit identically to the baseline analysis procedure (Sec. 3.2.4). The pre- and post-fit distributions are reported in Fig. 5.8a and Fig. 5.8b.

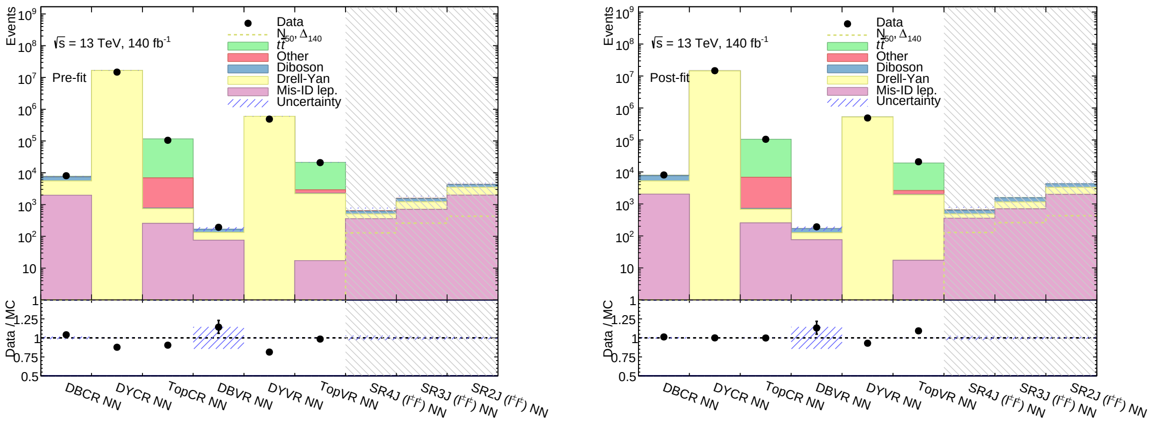

(a) Pre-fit. (b) Post-fit.

Figure 5.8: Pre-fit (a) and post-fit (b) event yields in the CRs and VRs for a representative signal mass hypothesis. Background processes include $t\bar{t}$, Diboson, DY, Other and Mis-ID leptons. The lower panel shows the ratio of data to the MC background prediction.

The Data/MC agreement across all regions confirms that the rescaling procedure does not introduce any bias in the background description and that the fit converges to a physically consistent solution.

5.3 Expected exclusion limits

The improvement in $\hat{\mu}$ is a direct consequence of the relative acceptance gain with the new selections: the signal yield increases by a factor of approximately 2.2 under the OR selection, while each background process increases by only 1.23 – 1.25. Since the expected sensitivity of counting experiments scales approximately as $S/\sqrt{B}$, in this case

$$\frac{2.2 \times S}{\sqrt{1.23 \times B}} = \frac{2.2}{\sqrt{1.23}} \times \frac{S}{\sqrt{B}} \approx 1.98 \times \frac{S}{\sqrt{B}} \tag{5.15}$$

[1] An Asimov dataset is a representative dataset in which the observed event counts are set equal to their expected values under a given hypothesis, without statistical fluctuations. It is commonly used to compute expected sensitivities and exclusion limits [105].

The net improvement in signal-to-background ratio translates into a reduction in the expected upper limit on $\hat{\mu}$, whose values are reported in Tab. 5.9, together with its $\pm 1\sigma$ and $\pm 2\sigma$ values. The $+2\sigma$ band of the expected limit stands below unity for almost all the mass points, indicating that the exclusion (for the mass points) can be done with 95% CL.

Table 5.9: Comparison of the expected limits and uncertainties for the A and B selection configurations for different mass hypotheses with $p_{\mathrm{T}}^{\mathrm{jet}} > 20\,\mathrm{GeV}$.

Selection	(m_N, m_Δ) [GeV]	**Expected**	-1σ	$+1\sigma$	-2σ	$+2\sigma$
A	(50,150)	0.373	0.268	0.522	0.199	0.704
B	(50,150)	0.355	0.255	0.497	0.190	0.670
A	(50,140)	0.319	0.229	0.446	0.171	0.600
B	(50,140)	0.301	0.216	0.421	0.161	0.566
A	(50,130)	0.310	0.223	0.433	0.166	0.583
B	(50,130)	0.291	0.209	0.406	0.155	0.547
A	(50,120)	0.381	0.274	0.532	0.204	0.716
B	(50,120)	0.354	0.255	0.495	0.189	0.666
A	(50,110)	0.568	0.408	0.793	0.304	1.07
B	(50,110)	0.522	0.375	0.729	0.279	0.981
A	(30,110)	1.41	1.01	1.97	0.754	2.65
B	(30,110)	1.33	0.958	1.86	0.713	2.50
A	(40,110)	0.441	0.318	0.616	0.236	0.829
B	(40,110)	0.416	0.299	0.581	0.223	0.781
A	(45,110)	0.410	0.295	0.573	0.219	0.771
B	(45,110)	0.384	0.276	0.535	0.205	0.721

The exclusion limit plots for fixed $m_N = 50\,\mathrm{GeV}$ are shown in Fig. 5.9a and Fig. 5.9b, while for fixed $m_\Delta = 110\,\mathrm{GeV}$ in Fig. 5.10a and Fig. 5.10b.

The jet $p_{\mathrm{T}} > 15, 20\,\mathrm{GeV}$ has a negligible impact on the conclusions, as can be observed with the consistency of the exclusion plots with Fig. B.5 and Fig. B.4. Lowering the jet p_{T} threshold is expected to migrate events from lower to higher jet-multiplicity regions, which carry greater discriminating power. However, this potential gain is not reflected in the exclusion limits obtained with the present fit model, suggesting that the current signal region definitions and fit setup do not yet fully exploit the additional sensitivity. A more dedicated optimisation of the analysis strategy, including a refined treatment of the higher-multiplicity regions, would be needed to assess the full impact of the looser jet selection.

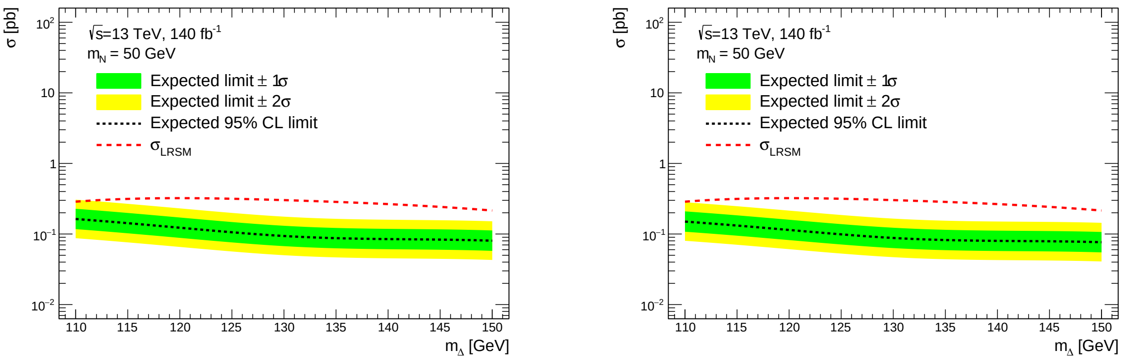

(a) Asymmetric selection, fixed $m_N = 50\,\mathrm{GeV}$.

(b) OR selection, fixed $m_N = 50\,\mathrm{GeV}$.

Figure 5.9: Exclusion plots for $p_{\mathrm{T}}^{\mathrm{jet}} > 20\,\mathrm{GeV}$, shown as a function of m_Δ at fixed $m_N = 50\,\mathrm{GeV}$.

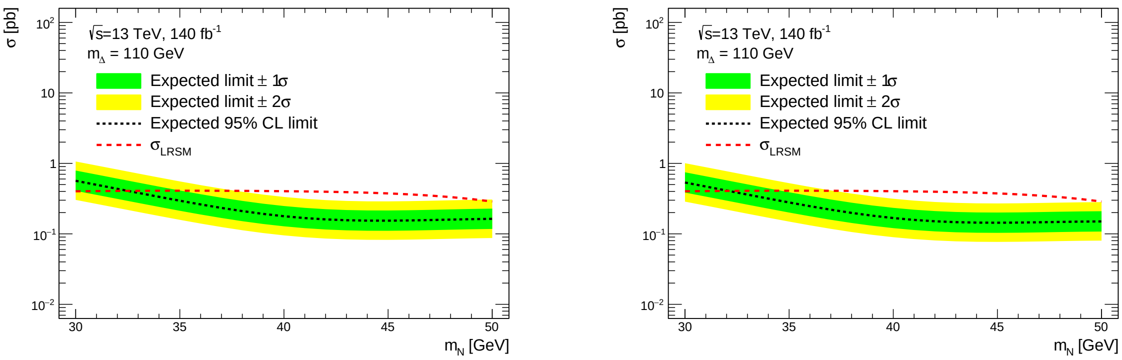

(a) Asymmetric selection, fixed $m_\Delta = 110\,\mathrm{GeV}$.

(b) OR selection, fixed $m_\Delta = 110\,\mathrm{GeV}$.

Figure 5.10: Exclusion plots for $p_{\mathrm{T}}^{\mathrm{jet}} > 20\,\mathrm{GeV}$, shown as a function of m_N at fixed $m_\Delta = 110\,\mathrm{GeV}$.

The inclusion of detector effects through Gaussian smearing produces only minor changes in the expected limits for μ (Tab. 5.10) and the exclusion limit plots for fixed $m_N = 50\,\mathrm{GeV}$ are shown in Fig. 5.11a, Fig. 5.11b and in Fig. 5.12a, Fig. 5.12b for fixed $m_\Delta = 110\,\mathrm{GeV}$. Therefore the results obtained with smeared objects remain consistent with those derived at truth-level, demonstrating that the gain in sensitivity is robust against more realistic detector resolutions.

Table 5.10: Expected limits for the A-smeared and B-smeared selections.

Selection	(m_N, m_Δ) [GeV]	Expected	-1σ	$+1\sigma$	-2σ	$+2\sigma$
A smeared	(50,150)	0.375	0.269	0.524	0.200	0.706
B smeared	(50,150)	0.357	0.256	0.498	0.190	0.672
A smeared	(50,140)	0.319	0.229	0.446	0.171	0.600
B smeared	(50,140)	0.301	0.216	0.420	0.161	0.566
A smeared	(50,130)	0.311	0.223	0.434	0.166	0.585
B smeared	(50,130)	0.292	0.210	0.407	0.156	0.548
A smeared	(50,120)	0.382	0.274	0.533	0.204	0.718
B smeared	(50,120)	0.354	0.255	0.495	0.189	0.666
A smeared	(50,110)	0.571	0.410	0.797	0.305	1.07
B smeared	(50,110)	0.524	0.376	0.731	0.280	0.984
A smeared	(30,110)	1.40	1.01	1.96	0.751	2.64
B smeared	(30,110)	1.33	0.955	1.85	0.711	2.50
A smeared	(40,110)	0.441	0.317	0.615	0.236	0.827
B smeared	(40,110)	0.415	0.298	0.579	0.222	0.779
A smeared	(45,110)	0.411	0.295	0.573	0.220	0.772
B smeared	(45,110)	0.384	0.276	0.536	0.205	0.722

An important note is that in the calculation of these limits, only statistical uncertainties are included, neglecting all the systematic uncertainties. The inclusion of systematic uncertainties would broaden the uncertainty bands and generally weaken the expected exclusion reach. Nevertheless, since the observed improvement originates from a substantial increase in signal acceptance relative to the background, the qualitative conclusion that the OR selection provides a significant enhancement in sensitivity is expected to remain valid.

The improvement in sensitivity obtained with the optimised selection provides the basis for the next stage of the analysis. In particular, the increased signal acceptance motivates the production of an extended grid of signal MC samples covering the (m_N, m_Δ) parameter space. This will enable the determination of the expected exclusion contour in the (m_N, m_Δ) plane at 95% CL, providing a complete assessment of the exclusion potential of this search.

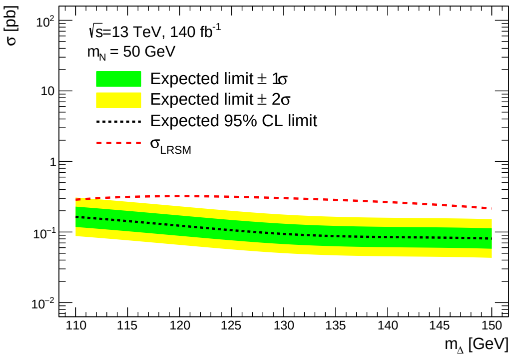

(a) Asymmetric selection, fixed $m_N = 50\,\text{GeV}$.

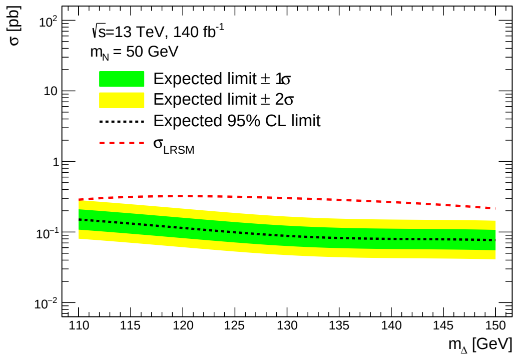

(b) OR selection, fixed $m_N = 50\,\text{GeV}$.

Figure 5.11: Exclusion plots obtained with smeared truth-level momenta for $p_{\mathrm{T}}^{\mathrm{jet}} > 20\,\text{GeV}$, shown as a function of m_Δ at fixed $m_N = 50\,\text{GeV}$.

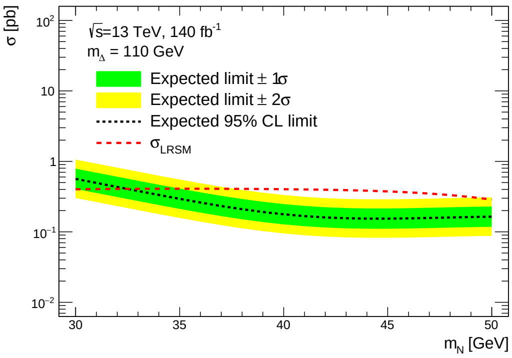

(a) Asymmetric selection, fixed $m_\Delta = 110\,\text{GeV}$.

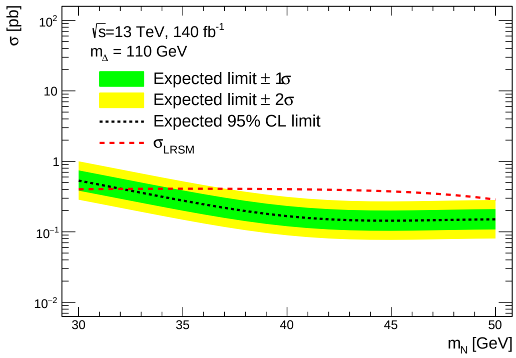

(b) OR selection, fixed $m_\Delta = 110\,\text{GeV}$.

Figure 5.12: Exclusion plots obtained with smeared truth-level momenta for $p_{\mathrm{T}}^{\mathrm{jet}} > 20\,\text{GeV}$, shown as a function of m_N at fixed $m_\Delta = 110\,\text{GeV}$.

Conclusions

The Standard Model of particle physics, despite its remarkable predictive success, leaves several fundamental questions unanswered, among which the origin and the lightness of neutrino masses. The Left-Right Symmetric Model provides an elegant theoretical framework to address these issues simultaneously, predicting the existence of heavy Majorana neutrinos N and an extended scalar sector. An allowed decay chain within this model is $gg \to \Delta \to NN \to 2l^{\pm}\,4j$, which produces a distinctive same-sign dilepton final state with four jets and negligible missing transverse energy, a topology with low Standard Model background that constitutes a clean experimental signature for this class of models.

This thesis presents a feasibility study for improving the signal selection sensitivity in the search for heavy Majorana neutrinos via the above-mentioned decay chain, using LHC Run 2 pp collision data at $\sqrt{s} = 13\,\mathrm{TeV}$ with an integrated luminosity of $140\,\mathrm{fb}^{-1}$ collected by the ATLAS detector. The work is structured in two main parts: a truth-level Monte Carlo validation of the signal topology and a study of alternative lepton p_{T} selection strategies with an assessment of the expected sensitivity through a profile likelihood fit.

The truth-level validation demonstrated the consistency of the generator-level decay chain across all signal mass hypotheses considered. The decay topology was reconstructed by tracing the full parentage information available at truth-level, uniquely assigning each final-state lepton and quark to the parent heavy-neutrino. The invariant mass difference Δm_{lqq} between the lepton-quarks systems associated with each N candidate was found to peak at zero, confirming the correctness of the parentage-based pairing algorithm. The study was extended at the jet-level by matching each truth-quark to its nearest truth-jet via a $\Delta R < 0.4$ criterion. The resulting Δm_{ljj} distribution was found to be broader than its quark-level counterpart, as expected from the finite jet energy resolution. A truth-level JER proxy derived from the relative transverse-momentum difference $\Delta p_{\mathrm{T,rel}} = (p_{\mathrm{T}}^{\mathrm{jet}} - p_{\mathrm{T}}^{q})/p_{\mathrm{T}}^{q}$ showed a resolution degrading from $\sigma \simeq 20\%$ at $p_{\mathrm{T}}^{q} \simeq 10\,\mathrm{GeV}$ to $\sigma \simeq 5\%$ at $p_{\mathrm{T}}^{q} \simeq 70\,\mathrm{GeV}$, qualitatively consistent with published ATLAS reconstruction-level JER measurements.

The second part of the work addressed the optimisation of the lepton p_{T} selection, which is a critical aspect of this analysis given that signal leptons from low-mass N decays are mostly soft, with p_{T} spectra peaking well below the 18 GeV threshold imposed by the ATLAS dilepton triggers. Three selection configurations were studied: the symmetric baseline ($p_{\mathrm{T}}^{l_{1,2}} > 18\,\mathrm{GeV}$), an asymmetric selection motivated by the ATLAS Run 2 single-lepton trigger ($p_{\mathrm{T}}(l_{\mathrm{leading}}) > 26\,\mathrm{GeV}$, $p_{\mathrm{T}}(l_{\mathrm{subleading}}) > 5\,\mathrm{GeV}$) and the logical OR of the two. The scale factors computed as the ratio of event yields with respect to the symmetric baseline reach SF $\simeq$ 2.1-2.6 for the signal under the OR selection, increasing towards lower

m_N where the lepton p_{T} spectrum is softest, while remaining at SF $\simeq$ 1.22-1.25 for all background processes. The robustness of these scale factors under detector resolution effects was confirmed through an approximated Gaussian smearing of the truth-level lepton and jet momenta: the smeared scale factors were found to be consistent with the truth-level values for all mass points considered.

The asymmetric and OR selections were carried forward to a profile likelihood fit, yielding expected upper limits on the signal cross-section at 95% CL that fall below the theoretical LRSM prediction for most of the mass points investigated. The mass point $(m_N,\, m_\Delta) = (30,\, 110)$ GeV represents the boundary of the accessible region, where the additional acceptance provided by the OR configuration is needed to approach exclusion.

The enhanced signal sensitivity achieved in this work provides the foundation for the next stage of the analysis. In particular, it motivates the generation of an extended grid of signal MC samples spanning the (m_N, m_Δ) parameter space. Such a dataset will make it possible to derive the expected 95% CL exclusion contour in the (m_N, m_Δ) plane, allowing the sensitivity of the search to be evaluated over the full parameter space rather than at the limited set of benchmark mass points considered in this study.

The inclusion of the 300 fb^{-1} dataset expected from LHC Run 3 would provide a further improvement in sensitivity of approximately

$$\sqrt{\frac{L_{\mathrm{Run2}} + L_{\mathrm{Run3}}}{L_{\mathrm{Run2}}}} = \sqrt{\frac{140 + 300}{140}} \approx \sqrt{3} \approx 1.7, \tag{5.16}$$

with respect to the present results, assuming a statistically dominated regime with comparable selection efficiency and background composition, potentially extending the exclusion reach to lower mass hypotheses currently at the boundary of the accessible region.

Appendix A
Additional validation studies

A.1 Δm_{lqq} combinatorial pairing

The pairing of leptons and quarks to the two heavy-neutrino candidates can be approached in two ways:

- In the *combinatorial* approach, no information about the true decay chain is used. All 12 possible lepton-quark assignments (6 ways to split the four quarks into two pairs, times 2 ways to assign the two leptons) are tried and the combination that minimises Δm_{lqq} is selected. This is a pure mathematical minimisation with no physics constraint: the algorithm can accidentally find a combination that gives a small mass difference even if the assignment is physically wrong. The resulting distribution (Fig. A.1) is therefore biased towards small values of Δm_{lqq}, since by construction, the minimum over all combinations is always selected.

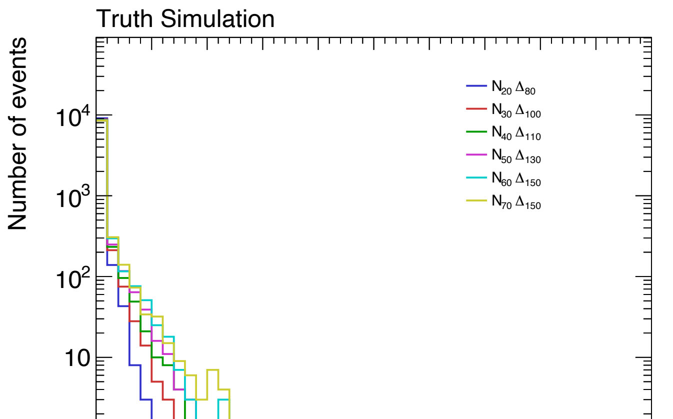

Figure A.1: Distribution of Δm_{lqq} obtained with the combinatorial pairing approach, in which the lepton-quark assignment minimising the mass difference is selected among all 12 possible combinations, without using any truth information.

- In the *truth-matched* approach described in Sec. 4.2.1, each lepton and each quark is uniquely assigned to the heavy neutrino N from which it originates, by tracing the decay chain back through the MC truth record. This gives a single, physically motivated assignment per event and the corresponding Δm_{lqq} reflects the true mass-reconstruction performance without any combinatorial bias.

Since both approaches are applied to the same set of events (those with exactly two charged leptons and four quarks in the final state) the two histograms contain the same number of entries. However, the difference lies entirely in which combination is selected: the combinatorial approach picks the assignment with the smallest Δm_{lqq}, while the truth-matched approach selects the physically correct one regardless of whether it is the minimum. As a result, the mean Δm_{lqq} is smaller in the combinatorial case than in the truth-matched case (Tab. A.1), confirming that the minimisation procedure introduces a downward bias that would enhance the apparent discrimination power of this variable in a real analysis, where the true assignment is not known.

Table A.1: Mean Δm_{lqq} (in GeV) obtained with the truth-matched and combinatorial pairing approaches, for events with exactly two charged leptons and four quarks in the final state.

Pairing approach	$\langle \Delta m_{lqq} \rangle$ [GeV]
Combinatorial (no truth matching)	0.383
Truth-matched (parentage check)	0.601

A.2 Alternative jet-matching algorithm

During the truth-level validation, an alternative jet-matching strategy was investigated alongside the standard ΔR-based approach described in Sec. 4.4.

The standard matching associates each truth-quark with the jet that minimises the angular separation $\Delta R(q, \text{jet})$. An alternative approach was tested, in which the matching criterion is instead the minimisation of the absolute transverse-momentum difference:

$$\Delta p_{\mathrm{T}} = |p_{\mathrm{T}}^{q} - p_{\mathrm{T}}^{\text{jet}}| \tag{A.1}$$

The motivation is that, for the soft signal regime ($p_{\mathrm{T}} \lesssim 20\,\text{GeV}$), jets may be geometrically dispersed and a p_{T}-based criterion could in principle recover associations that the ΔR criterion misses. As it is expected, the p_{T}-based matching achieves a higher jet-matching efficiency, compared to the ΔR-based one, because the p_{T}-based algorithm can always find a jet with a p_{T} close to the quark p_{T}, regardless of the angular distance between them. However, this comes at the cost of reduced purity: since there is no geometric constraint, the matched jet may be physically unrelated to the originating quark.

To assess the quality of the p_{T}-based associations, the $\Delta R(q, \text{jet})$ between each matched quark-jet pair is computed. As shown in Fig. A.2, the p_{T}-based matching yields a broad, uncollimated distribution, while the ΔR-based matching produces a sharp peak at small ΔR.

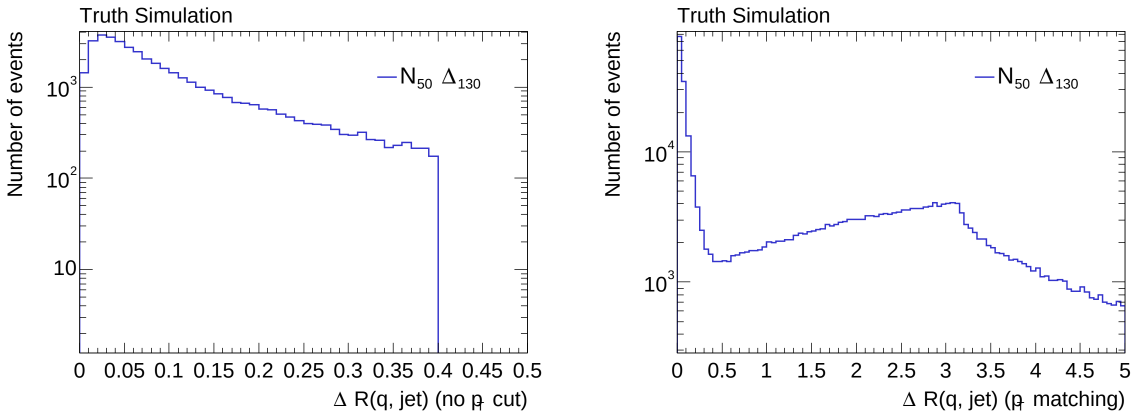

(a) $\Delta R(q, \text{jet})$ for p_{T}-based method.

(b) $\Delta R(q, \text{jet})$ for ΔR-based method.

Figure A.2: Comparison of the $\Delta R(q, \text{jet})$ distribution for the p_{T}-based matching (b) and the ΔR-based matching (a), for the mass point $m_N = 50\,\text{GeV}$,$m_\Delta = 130\,\text{GeV}$.

This confirms that the algorithm frequently associates quarks with geometrically distant jets, producing physically meaningless pairings.

In contrast, the ΔR-based matching produces a distribution sharply peaked at small values, $\langle \Delta R \rangle \approx 0.10$, confirming that the matched jets are geometrically close to the originating quarks.

Therefore, despite its higher efficiency in terms of acceptance, the p_{T}-based matching is not suitable as the primary jet-matching strategy for this analysis, due to the low quality of its selection. The ΔR-based matching, while selecting fewer events, provides a much cleaner and physically motivated association and is indeed adopted as the standard procedure throughout the truth-level validation.

A.3 Gaussian smearing validation distributions

The leptons and jets p_{T} spectra, alongside the Δm_{lqq} and Δm_{ljj} distributions modified by the Gaussian smearing procedure described in Sec. 5.1.4, applied to the benchmark signal point $m_N = 50\,\text{GeV}$, $m_\Delta = 130\,\text{GeV}$, are reported here.

Fig. A.3 and Fig. A.4 compare the smeared and non-smeared distributions of the lepton and the jet p_{T}, before any kinematic selection, so that the full spectrum is visible.

The mean values shift by less than 1% under smearing, therefore the overall shape of both distributions is preserved, confirming that the smearing does not introduce significant distortions of the kinematic spectra.

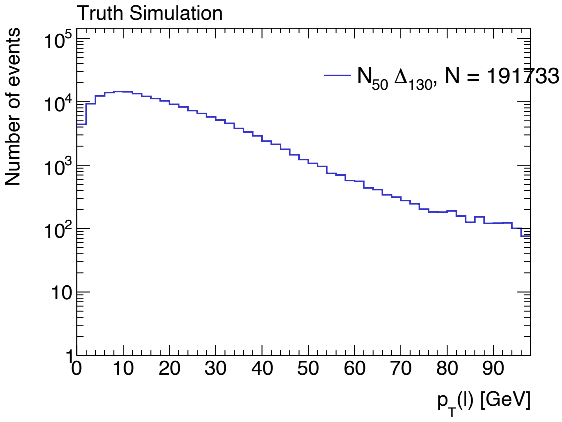

(a) Non-smeared leptons p_{T} distribution.

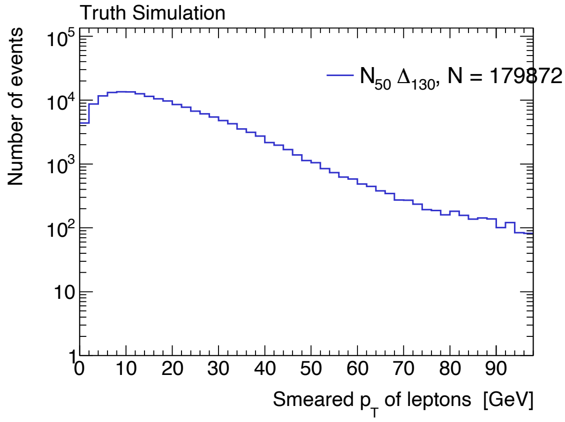

(b) Smeared leptons p_{T} distribution.

Figure A.3: Comparison between lepton p_{T} distributions for the non-smeared and smeared cases.

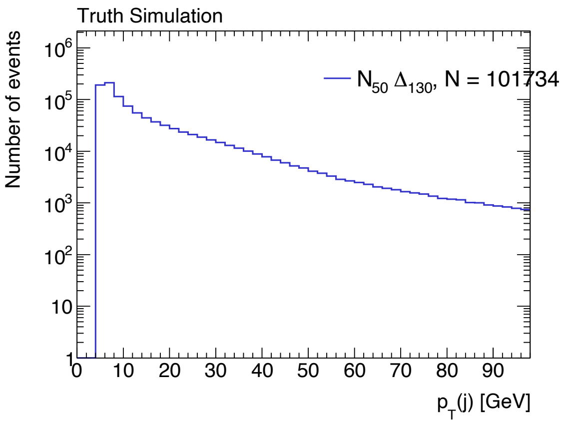

(a) Non-smeared jet p_{T} distribution.

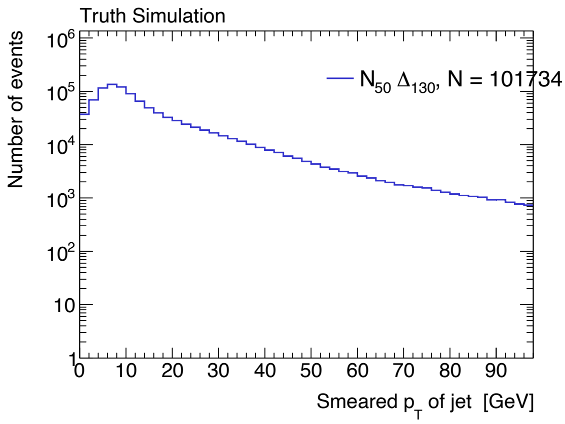

(b) Smeared jet p_{T} distribution.

Figure A.4: Comparison between jet p_{T} distributions for the non-smeared and smeared cases.

Fig. A.5 and Fig. A.6 compare the smeared and non-smeared distributions of Δm_{lqq} and Δm_{ljj}. The quantity Δm_{lqq} is reconstructed using smeared lepton four-momenta and non-smeared (truth) quark four-momenta. The quantity Δm_{ljj} is reconstructed using both smeared lepton and smeared jet four-momenta, requiring $p_{\mathrm{T}}^{\text{jet,smeared}} > 20\,\text{GeV}$ and therefore probes the effect of both resolutions on the mass reconstruction. The broadening of Δm_{lqq} under smearing is the expected consequence of the finite lepton momentum resolution, which degrades the mass balance between the two reconstructed N candidates.

The low statistics visible in the Δm_{ljj} distributions reflect the stricter selection requiring exactly two leptons and four quarks passing the parentage check and the additional request of four jets passing the p_{T} threshold simultaneously. However, in the smeared Δm_{ljj} more events are present since the jet smearing causes a fraction of non-smeared truth-jets with p_{T} near the 20 GeV threshold to go above it and therefore pass the selection.

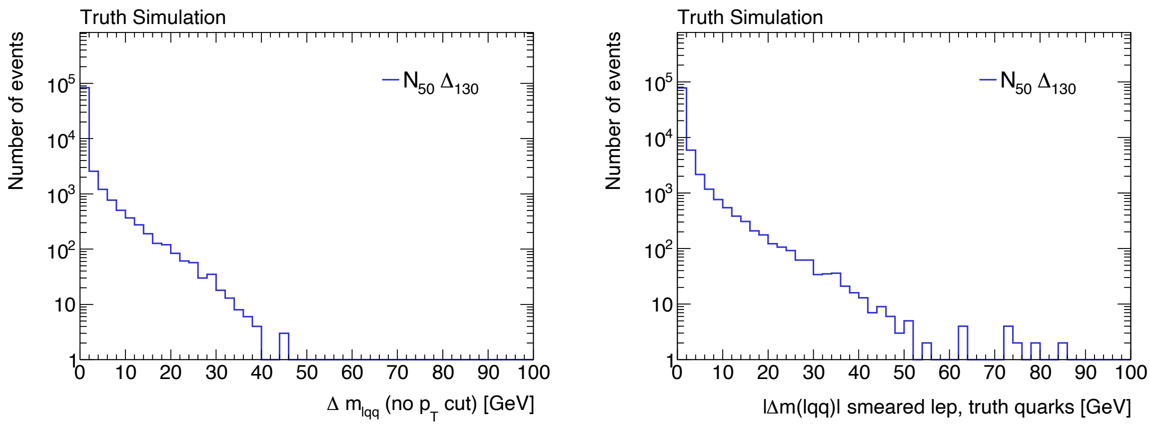

(a) Non-smeared Δm_{lqq} distribution, with no quarks p_{T} cut.

(b) Smeared Δm_{lqq} distribution, with no quarks p_{T} cut.

Figure A.5: Comparison of Δm_{lqq} distributions for the non-smeared and smeared cases.

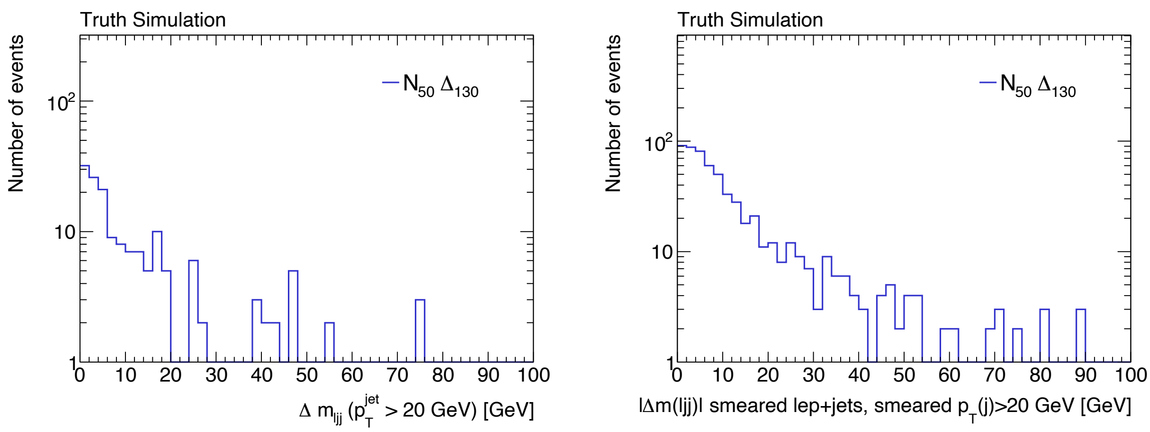

(a) Non-smeared Δm_{ljj} distribution, with $p_{\mathrm{T}}^{jet} > 20$ GeV.

(b) Smeared Δm_{ljj} distribution, with $p_{\mathrm{T}}^{jet} > 20$ GeV.

Figure A.6: Comparison of Δm_{ljj} distributions for the non-smeared and smeared cases.

As a final consideration, the small shift in the lepton p_{T} mean and the limited broadening of Δm_{lqq} confirm that the lepton momentum resolution has a negligible impact. The more significant effect observed in Δm_{ljj} is driven by the JER and the proximity of the signal jet p_{T} spectrum to the 20 GeV selection threshold.

Appendix B
Supplementary results

B.1 Yields

The expected event yields for each background process in CRs, VRs and SRs are reported in Tab. B.1. These values are provided for completeness and document the relative composition of the backgrounds used for the for analysis of Chap. 5.

Table B.1: Yields for each background process for different analysis regions.

Region	**Diboson**	**Drell-Yan**	**Mis-Id lept.**	**Other**	$t\bar{t}$
MLDYCR	124140 ± 50	$(1.362 \pm 0.005) \times 10^7$	1800 ± 900	9810 ± 40	72010 ± 100
MLDYVR	2335 ± 7	492000 ± 1300	15 ± 6	38.1 ± 2.4	272 ± 6
MLTopCR	25.7 ± 0.7	401 ± 11	220 ± 40	4519 ± 25	88990 ± 110
MLTopVR	33.8 ± 0.4	1794 ± 27	10 ± 23	487 ± 8	14850 ± 50
MLDBCR	1494 ± 6	2900 ± 100	1600 ± 50	71.7 ± 3.1	238 ± 6
MLDBVR	29.1 ± 0.8	47 ± 13	61 ± 15	0.021 ± 0.007	0.47 ± 0.23
MLSR2J	653.9 ± 3.1	1220 ± 40	2380 ± 50	8.7 ± 0.7	26.0 ± 2.0
MLSR3J	262.8 ± 1.7	348 ± 17	1078 ± 29	9.4 ± 0.6	16.5 ± 1.6
MLSR4J	93.2 ± 0.9	118 ± 8	495 ± 16	7.7 ± 0.4	10.0 ± 1.2

B.2 Results for $p_{\mathrm{T}}^{\mathrm{jet}} > 15\,\mathrm{GeV}$ alternative selection

Results of the cut optimisation and expected sensitivity studies for the case $p_{\mathrm{T}}^{\mathrm{jet}} > 15\,\mathrm{GeV}$, complementing the main analysis presented in Chap. 5, are reported here for completeness and to confirm that the conclusions are stable with respect to this threshold variation.

Tab. B.2 summarises the signal event yields and SFs computed as $\mathrm{SF} = \frac{N_{\mathrm{sel}}}{N_{\mathrm{sym}}}$, for the benchmark mass point $m_N = 50\,\mathrm{GeV}$, $m_\Delta = 130\,\mathrm{GeV}$, under the three lepton p_{T} selection scenarios. In this case, the two selection configurations are denoted as **C**, for the asymmetric $p_{\mathrm{T}}(l_{\mathrm{leading}}) > 26\,\mathrm{GeV}$, $p_{\mathrm{T}}(l_{\mathrm{subleading}}) > 5\,\mathrm{GeV}$ and **D**, for the logic OR of symmetric and asymmetric selections.

Table B.2: Signal event yields and SFs for different lepton p_{T} selection scenarios, for events with at least two jets with $p_{\mathrm{T}}^{\mathrm{jet}} > 15\,\mathrm{GeV}$, for the benchmark mass point $m_N = 50\,\mathrm{GeV}$, $m_\Delta = 130\,\mathrm{GeV}$. The percentage is done with respect to the total generated events (100000).

Selection	**Events**	**SF**
Symmetric: $p_{\mathrm{T}}(l_{1,2}) > 18\,\mathrm{GeV}$	15.72%	1.000
Asymmetric: $p_{\mathrm{T}}(l_{\mathrm{leading}}) > 26\,\mathrm{GeV}$, $p_{\mathrm{T}}(l_{\mathrm{subleading}}) > 5\,\mathrm{GeV}$ (C)	32.09%	2.041 ± 0.020
OR of symmetric and asymmetric (D)	34.68%	2.206 ± 0.021

The looser jet threshold increases the absolute event yields with respect to the $p_{\mathrm{T}}^{\mathrm{jet}} > 20\,\mathrm{GeV}$ case, while the SFs remain consistent: the asymmetric selection recovers approximately twice the signal of the symmetric baseline and the OR selection provides a further improvement, in close agreement with the values obtained for the $p_{\mathrm{T}}^{\mathrm{jet}} > 20\,\mathrm{GeV}$ case. The two-dimensional lepton p_{T} distribution for this threshold is shown in Fig. B.1, confirming the same kinematic structure observed in the main analysis.

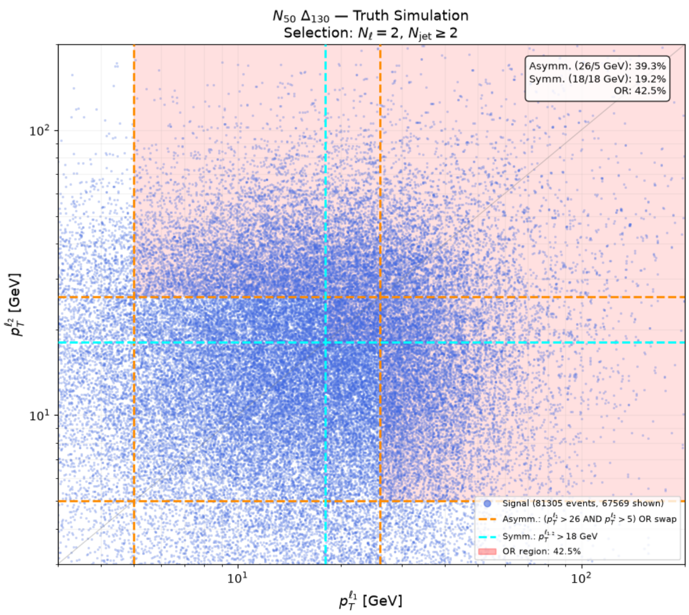

Figure B.1: Distribution of the two leptons transverse momenta, $p_T^{l_1}$ vs. $p_T^{l_2}$, in logarithmic scale, for the signal sample for the benchmark mass point $m_N = 50\,\mathrm{GeV}$, $m_\Delta = 130\,\mathrm{GeV}$, requiring $N_l = 2$ and $N_{\mathrm{jet}} \geq 2$ with $p_T^{\mathrm{jet}} > 15\,\mathrm{GeV}$. The shaded red region indicates the OR union of the two lepton p_{T} selection criteria. The orange dashed lines mark the asymmetric thresholds (C) and the cyan dashed lines mark the symmetric threshold ($p_T^{l_{1,2}} > 18\,\mathrm{GeV}$). The OR selection retains 42.5% of signal events (the percentage is done with respect to the total events that pass the selection of $N_l = 2$, $N_{\mathrm{jet}} \geq 2$ with $p_{\mathrm{T}} > 15\,\mathrm{GeV}$), with 39.3% passing the asymmetric criterion and 19.2% the symmetric one.

The SFs with their relative uncertanties are computed also for additional mass hypotheses and are reported in Tab B.3.

Table B.3: SFs and their relative uncertanties for different mass hypotheses for selections C and D with $p_T^{\text{jet}} > 15\,\text{GeV}$.

(m_N, m_Δ) [GeV]	**C**	**D**
(50,150)	1.965 ± 0.017	2.083 ± 0.018
(50,140)	1.981 ± 0.018	2.124 ± 0.019
(50,130)	2.022 ± 0.020	2.186 ± 0.021
(50,120)	1.989 ± 0.021	2.184 ± 0.023
(50,110)	1.865 ± 0.022	2.092 ± 0.024
(30,110)	2.353 ± 0.031	2.535 ± 0.032
(40,110)	2.282 ± 0.030	2.472 ± 0.031
(45,110)	2.134 ± 0.028	2.336 ± 0.030

The values are in good agreement with those obtained for $p_T^{\text{jet}} > 20\,\text{GeV}$ (Tab. 5.5), with differences at the percent level.

The distribution of SFs for the different configurations as a function of the masses considered is provided in Fig. B.2.

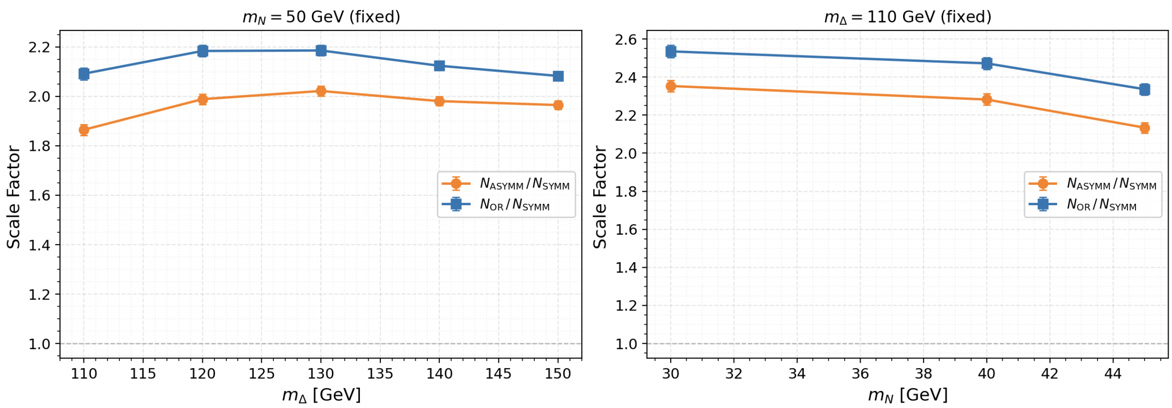

Figure B.2: Distributions of SFs for different mass hypotheses for A (blue) and B (orange) selections, as a function of m_N or m_Δ, for $p_T^{\text{jet}} > 15\,\text{GeV}$, with relative uncertanty bands. Left: SFs for the mass points with $m_N = 50\,\text{GeV}$ fixed as a function of m_Δ. Right: SFs for the mass points with $m_\Delta = 110\,\text{GeV}$ fixed as a function of m_N.

The SFs for the backgrounds are reported in Tab. B.4 and as in the main analysis, are approximately uniform across processes, with values in the range 1.22–1.26 for both C and D selection configurations, differing negligibly from their $p_T^{\text{jet}} > 20\,\text{GeV}$ counterparts.

Table B.4: SFs and relative uncertanties for C and D selections for each background sample and $p_T^{\text{jet}} > 15\,\text{GeV}$.

Background	**C**	**D**
Diboson	1.227 ± 0.005	1.240 ± 0.005
Drell-Yan	1.218 ± 0.004	1.228 ± 0.004
Mis-ID lept.	1.234 ± 0.008	1.255 ± 0.008
Other	1.224 ± 0.008	1.235 ± 0.008
$t\bar{t}$	1.234 ± 0.008	1.255 ± 0.008

The scatter plot which shows the lepton p_{T} distributions for all background samples under the $p_{\text{T}}^{\text{jet}} > 15\,\text{GeV}$ requirement is shown in Fig. B.3. The same plot in logarithmic scale is shown in App. B.3.

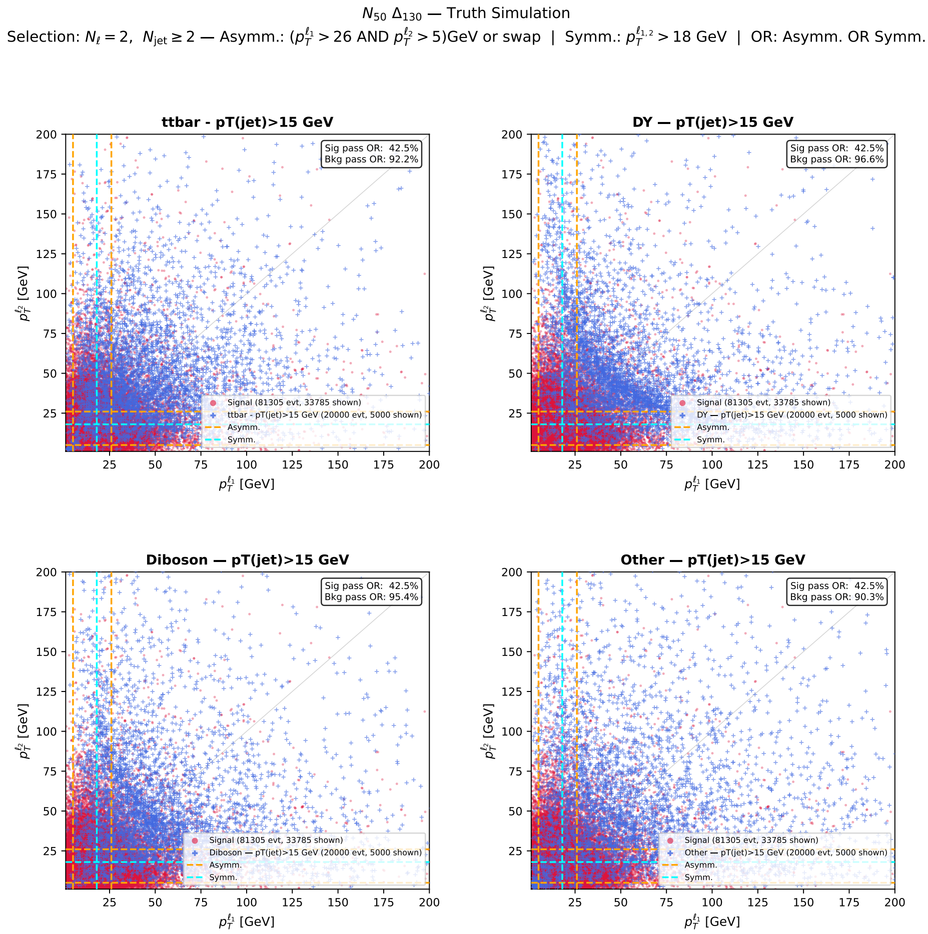

Figure B.3: Overlap, in the $p_{\text{T}}^{l_1}$ vs. $p_{\text{T}}^{l_2}$ plane, between the distributions of the signal sample ($m_N = 50\,\text{GeV}$, $m_\Delta = 130\,\text{GeV}$, red circles) and that of the four SM background samples considered (blue crosses). The signal distribution is obtained from the truth-level MC sample requiring exactly $N_l = 2$ and $N_{\text{jet}} \geq 2$ with $p_{\text{T}} > 15\,\text{GeV}$. The dashed lines indicate the lepton p_{T} trigger thresholds used in the selection: orange for the asymmetric selection (C) and cyan for the symmetric selection ($p_{\text{T}}^{l_{1,2}} > 18\,\text{GeV}$).

The SFs for data in the different regions are instead shown in Tab. B.5. The uncertanties for this case are computed by considering the uncertanties for background SFs for $p_{\mathrm{T}}^{\mathrm{jet}} > 15\,\mathrm{GeV}$ while the errors on the yields Y_i are considered equal to the ones for the case $p_{\mathrm{T}}^{\mathrm{jet}} > 20\,\mathrm{GeV}$.

Table B.5: SFs and their relative uncertanties for data in each analysis region and $p_T^{\mathrm{jet}} > 15\,\mathrm{GeV}$ for C and D selections. The uncertainties include the propagation of the statistical uncertainties on both the MC yields evaluated at $p_T^{\mathrm{jet}} > 20\,\mathrm{GeV}$ and the background scale factors evaluated at $p_T^{\mathrm{jet}} > 15\,\mathrm{GeV}$.

Region	**C**	**D**
MLDYCR	1.218 ± 0.005	1.228 ± 0.005
MLDYVR	1.218 ± 0.005	1.228 ± 0.005
MLTopCR	1.234 ± 0.007	1.254 ± 0.007
MLTopVR	1.232 ± 0.006	1.252 ± 0.006
MLDBCR	1.225 ± 0.006	1.239 ± 0.006
MLDBVR	1.227 ± 0.007	1.243 ± 0.007
MLSR2J	1.228 ± 0.007	1.245 ± 0.007
MLSR3J	1.230 ± 0.007	1.247 ± 0.007
MLSR4J	1.231 ± 0.007	1.249 ± 0.007

The expected limits and uncertainty bands for the C and D selections for different mass hypotheses with $p_{\mathrm{T}}^{\mathrm{jet}} > 15\,\mathrm{GeV}$ case are shown in Tab. B.6.

Table B.6: Comparison of the expected limits and uncertainties for the C and D selection configurations for different mass hypotheses with $p_T^{\mathrm{jet}} > 15\,\mathrm{GeV}$.

Selection	(m_N, m_Δ) **[GeV]**	**Expected**	-1σ	$+1\sigma$	-2σ	$+2\sigma$
A	(50,150)	0.381	0.273	0.532	0.203	0.717
B	(50,150)	0.362	0.260	0.506	0.193	0.682
A	(50,140)	0.325	0.234	0.454	0.174	0.612
B	(50,140)	0.306	0.220	0.427	0.164	0.575
A	(50,130)	0.315	0.227	0.440	0.169	0.593
B	(50,130)	0.294	0.211	0.410	0.157	0.552
A	(50,120)	0.386	0.277	0.539	0.206	0.726
B	(50,120)	0.354	0.255	0.495	0.189	0.666
A	(50,110)	0.576	0.414	0.804	0.308	1.08
B	(50,110)	0.517	0.372	0.722	0.277	0.972
A	(30,110)	1.44	1.04	2.01	0.772	2.71
B	(30,110)	1.35	0.973	1.89	0.724	2.54
A	(40,110)	0.444	0.319	0.619	0.237	0.833
B	(40,110)	0.413	0.297	0.577	0.221	0.776
A	(45,110)	0.414	0.298	0.578	0.221	0.778
B	(45,110)	0.382	0.274	0.532	0.204	0.717

The exclusion plots are Fig. B.4 for $m_N = 50\,\mathrm{GeV}$ fixed and in Fig. B.5 for $m_\Delta = 110\,\mathrm{GeV}$

fixed. The results mirror those of the main analysis: the asymmetric selection fails to exclude the $m_\Delta = 110\,\text{GeV}$ mass point at 95% CL, while OR selection achieves exclusion across the full range $m_\Delta \in [110, 150]\,\text{GeV}$ at $m_N = 50\,\text{GeV}$.

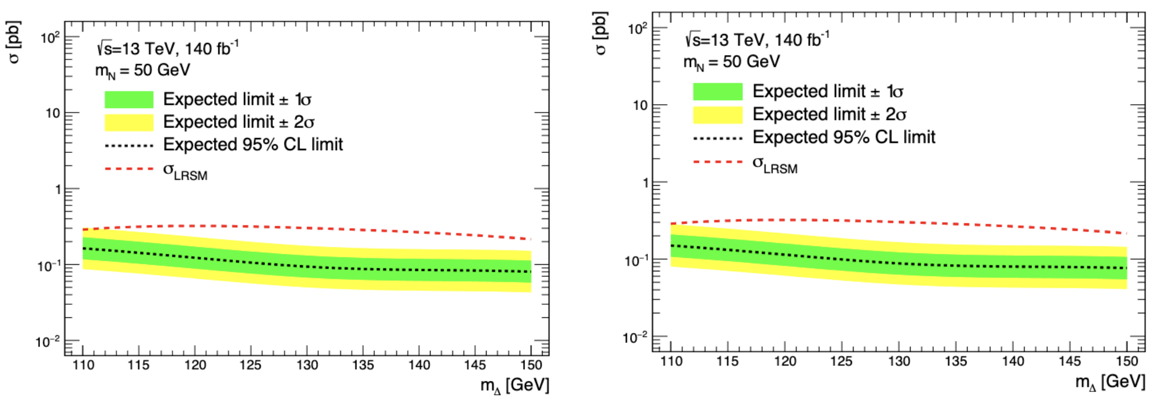

(a) Asymmetric selection, fixed $m_N = 50\,\text{GeV}$. (b) OR selection, fixed $m_N = 50\,\text{GeV}$.

Figure B.4: Exclusion plots for $p_T^{\text{jet}} > 15\,\text{GeV}$, shown as a function of m_Δ at fixed $m_N = 50\,\text{GeV}$.

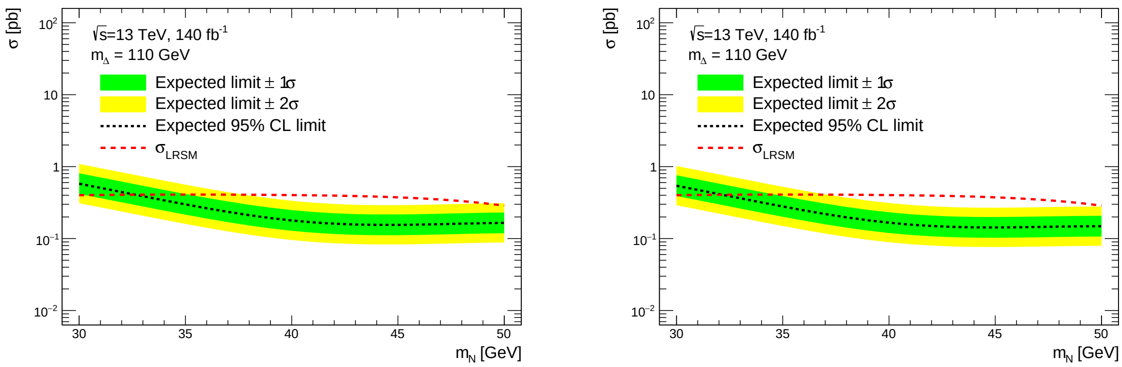

(a) Asymmetric selection, fixed $m_\Delta = 110\,\text{GeV}$. (b) OR selection, fixed $m_\Delta = 110\,\text{GeV}$.

Figure B.5: Exclusion plots for $p_T^{\text{jet}} > 15\,\text{GeV}$, shown as a function of m_N at fixed $m_\Delta = 110\,\text{GeV}$.

The consistency between the two jet thresholds confirms that the sensitivity improvement driven by the optimised lepton selection is robust.

B.3 Signal-background overlap

This appendix complements the scatter plots presented in Sec. 5.1.1 and App. B.2 by showing the same two-dimensional lepton-p_T distributions in logarithmic scale, which provides a clearer view of the low-p_T region. This region is particularly relevant for the signal, since leptons originating from heavy neutrino decays are predominantly soft. Fig. B.6 and Fig. B.7 show the distributions for the $p_T^{\text{jet}} > 20$ and 15 GeV selections, respectively.

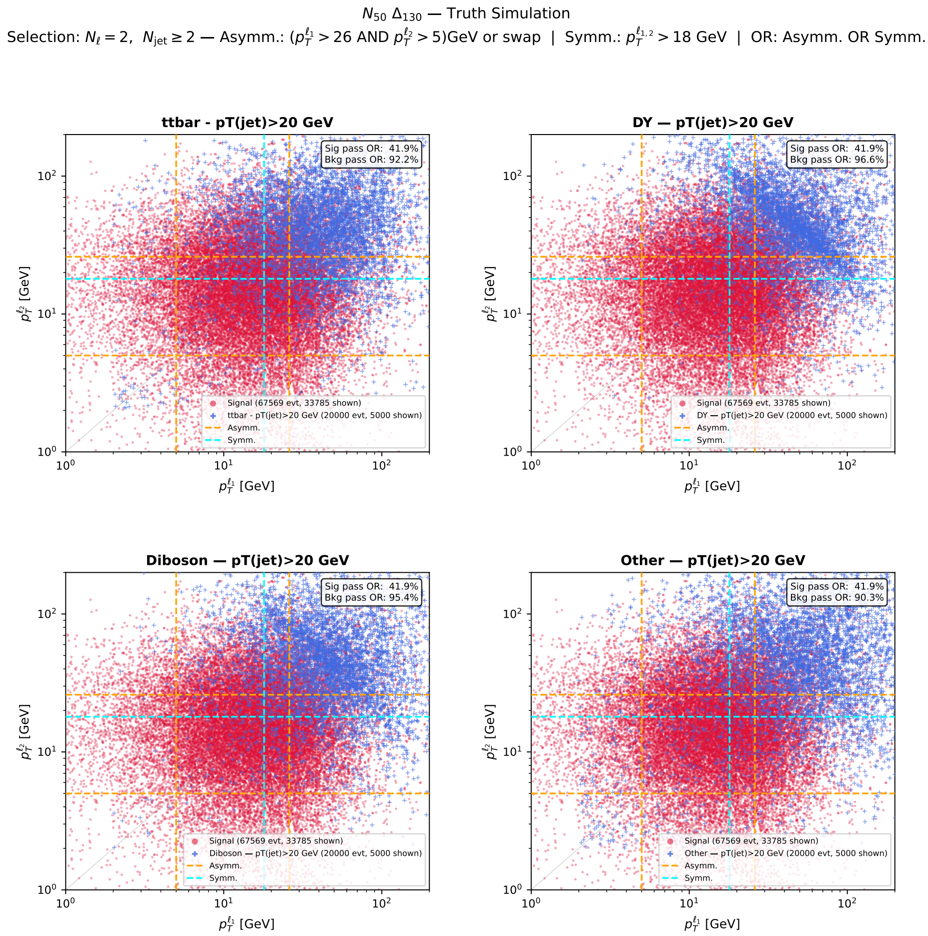

Figure B.6: Scatter plots of $p_{\mathrm{T}}^{l_2}$ vs. $p_{\mathrm{T}}^{l_1}$ in logarithmic scale for all background samples, requiring $N_l = 2$ and $N_{\mathrm{jet}} \geq 2$ with $p_{\mathrm{T}}^{\mathrm{jet}} > 20\,\mathrm{GeV}$.

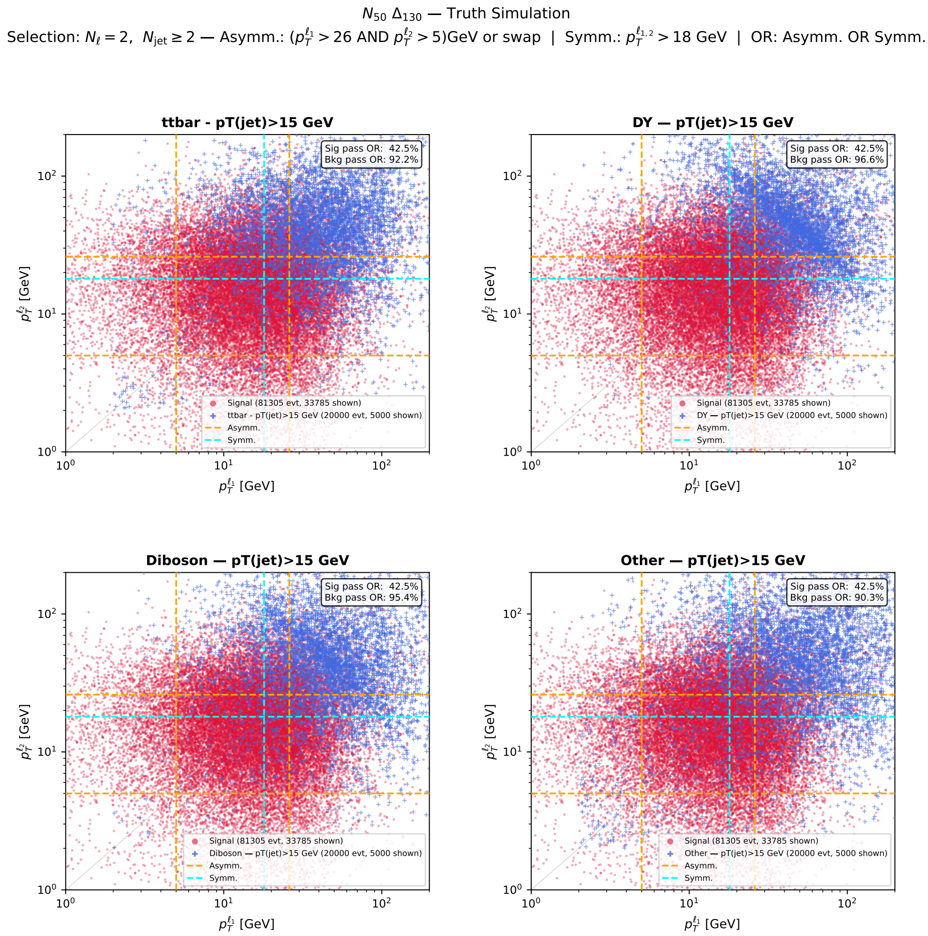

Figure B.7: Scatter plots of $p_{\mathrm{T}}^{l_2}$ vs. $p_{\mathrm{T}}^{l_1}$ in logarithmic scale for all background samples, requiring $N_l = 2$ and $N_{\mathrm{jet}} \geq 2$ with $p_{\mathrm{T}}^{\mathrm{jet}} > 15\,\mathrm{GeV}$.

The signal population extends significantly towards lower lepton transverse momenta than the SM backgrounds. In principle, lowering the lepton p_{T} thresholds would therefore recover a substantial fraction of signal events. However, these thresholds cannot be lowered indefinitely because of the trigger requirements imposed by the ATLAS data-taking strategy. The alternative asymmetric selection adopted in this work is designed to recover part of this low-p_{T} signal acceptance while remaining compatible with the available Run 2 trigger menu.

List of Figures

List of Tables

Bibliography

[1] Michael E. Peskin and Daniel V. Schroeder. *An Introduction to Quantum Field Theory*. Addison-Wesley, Reading, MA, 1995.

[2] F. Englert and R. Brout. Broken symmetry and the mass of gauge vector mesons. *Physical Review Letters*, 13:321, 1964.

[3] P. W. Higgs. Broken symmetries and the masses of gauge bosons. *Physical Review Letters*, 13:508, 1964.

[4] Mark Thomson. *Modern Particle Physics*. Cambridge University Press, Cambridge, United Kingdom, 2013.

[5] ATLAS Collaboration. Observation of a new particle in the search for the Standard Model Higgs boson with the ATLAS detector at the LHC. *Physics Letters B*, 716:1–29, 2012.

[6] CMS Collaboration. Observation of a new boson at a mass of 125 GeV with the CMS experiment at the LHC. *Physics Letters B*, 716:30–61, 2012.

[7] Emmy Noether. Invariant variation problems. *Transport Theory and Statistical Physics*, 1(3):186–207, January 1971.

[8] H. Fritzsch, M. Gell-Mann, and H. Leutwyler. Advantages of the color octet gluon picture. *Physics Letters B*, 47(4):365–368, 1973.

[9] Wolfgang Pauli. Letter to the physical society of tübingen. Pauli Archive, CERN, Geneva, 12 1930. Reproduced in W. Pauli, *Collected Scientific Papers*, eds. R. Kronig and V. F. Weisskopf, Interscience, New York (1964).

[10] E. Fermi. Tentativo di una teoria dei raggi β. *Il Nuovo Cimento (1924-1942)*, 11(1):1, 1934.

[11] C. S. Wu, E. Ambler, R. W. Hayward, D. D. Hoppes, and R. P. Hudson. Experimental test of parity conservation in beta decay. *Phys. Rev.*, 105:1413–1415, Feb 1957.

[12] Carlo Giunti and Chung W. Kim. *Fundamentals of Neutrino Physics and Astrophysics*. Oxford University Press, Oxford, 2007.

[13] M. Goldhaber, L. Grodzins, and A. W. Sunyar. Helicity of neutrinos. *Phys. Rev.*, 109(3):1015–1017, 1958.

[14] Super-Kamiokande Collaboration. Evidence for an Oscillatory Signature in Atmospheric Neutrino Oscillation. *Physical Review Letters*, 81:1562–1567, 1998.

[15] SNO Collaboration. Direct Evidence for Neutrino Flavor Transformation from Neutral-Current Interactions in the Sudbury Neutrino Observatory. *Physical Review Letters*, 89:011301, 2002.

[16] F. J. Hasert et al. Observation of Neutrino Like Interactions Without Muon Or Electron in the Gargamelle Neutrino Experiment. *Phys. Lett. B*, 46:138–140, 1973.

[17] Samuel Hedges. *Low Energy Neutrino-Nucleus Interactions at the Spallation Neutron Source*. Springer Theses: Recognising Outstanding Ph.D. Research. Springer Nature Switzerland, Cham, 2024.

[18] S. Glashow. The renormalizability of vector meson interactions. *Nucl. Phys.*, 10:107, 1959.

[19] A. Salam and J.C. Ward. Electromagnetic and weak interactions. *Phys. Lett.*, 13(2):168–171, 1964.

[20] S. Weinberg. A model of leptons. *Phys. Rev. Lett.*, 19(21):1264, 1967.

[21] M. Gell-Mann. The interpretation of the new particles as displaced charge multiplets. *Il Nuovo Cimento (1955-1965)*, 4:848, 1956.

[22] T. Nakano and K. Nishijima. Charge independence for v-particles. *Progress of Theoretical Physics*, 10:581, 1953.

[23] J. Goldstone. Field Theories with Superconductor Solutions. *Il Nuovo Cimento*, 19:154–164, 1961.

[24] J. Goldstone, Abdus Salam, and Steven Weinberg. Broken Symmetries. *Physical Review*, 127:965–970, 1962.

[25] S. Schael et al. Precision electroweak measurements on the Z resonance. *Phys. Rept.*, 427:257–454, 2006.

[26] Nicola Cabibbo. Unitary Symmetry and Leptonic Decays. *Phys. Rev. Lett.*, 10:531–533, 1963.

[27] Makoto Kobayashi and Toshihide Maskawa. CP Violation in the Renormalizable Theory of Weak Interaction. *Prog. Theor. Phys.*, 49(2):652–657, 1973.

[28] A. D. Sakharov. Violation of CP Invariance, C Asymmetry, and Baryon Asymmetry of the Universe. *JETP Letters*, 5:24–27, 1967. Pisma Zh. Eksp. Teor. Fiz. 5 (1967) 32.

[29] KATRIN Collaboration. Direct neutrino-mass measurement based on 259 days of KATRIN data. *Science*, 2025.

[30] K. Assamagan et al. Upper limit of the muon-neutrino mass and charged-pion mass from momentum analysis of a surface muon beam. *Physical Review D*, 53:6065–6077, 1996.

[31] ALEPH Collaboration. An upper limit on the τ neutrino mass from three- and five-prong tau decays. *European Physical Journal C*, 2:395–406, 1998.

[32] Rabindra N. Mohapatra. Seesaw mechanism and its implications. 12 2004. arXiv:hep-ph/0412379v1.

[33] Asmaa Abada et al. Low energy effects of neutrino masses. *Journal of High Energy Physics*, 12:061, 2007.

[34] Steven Weinberg. Baryon and lepton nonconserving processes. *Phys. Rev. Lett.*, 43:1566–1570, 1979.

[35] Murray Gell-Mann, Pierre Ramond, and Richard Slansky. Complex spinors and unified theories. pages 315–321, 1979.

[36] Rabindra N. Mohapatra and Goran Senjanovic. Neutrino mass and spontaneous parity nonconservation. *Phys. Rev. Lett.*, 44:912–915, 1980.

[37] Tsutomu Yanagida. Horizontal symmetry and masses of neutrinos. *Conf. Proc. C*, 7902131:95–99, 1979.

[38] Peter Minkowski. $\mu \to e\gamma$ at a rate of one out of 10^9 muon decays? *Phys. Lett. B*, 67:421–428, 1977.

[39] Yi Cai, Tao Han, Tong Li, and Richard Ruiz. Lepton number violation: Seesaw models and their collider tests. *Front. in Phys.*, 6:40, 2018.

[40] Frank F. Deppisch, P. S. Bhupal Dev, and Apostolos Pilaftsis. Neutrinos and collider physics. 2018.

[41] W. Grimus. Introduction to left-right symmetric models. Lectures given at the Schladming Winter School.

[42] Utkarsh Patel, Pratik Adarsh, Sudhanwa Patra, and Purushottam Sahu. Leptogenesis in a left-right symmetric model with double seesaw. *JHEP*, 03:029, 2024.

[43] Alessio Maiezza, Miha Nemevsek, and Fabrizio Nesti. Lepton number violation in higgs decay at the LHC. 9 2015. arXiv:1503.06834v3.

[44] Alessio Maiezza, Miha Nemešček, Fabrizio Nesti, and Goran Senjanović. Left-right symmetry at LHC. *Physical Review D*, 82:055022, 2010.

[45] ATLAS Collaboration. Search for heavy majorana or dirac neutrinos and right-handed w gauge bosons in final states with two charged leptons and two jets at $\sqrt{s} = 13$ tev with the atlas detector. *JHEP*, 01:016, 2019.

[46] CMS Collaboration. Search for a right-handed w boson and a heavy neutrino in proton-proton collisions at $\sqrt{s} = 13$ TeV. *Journal of High Energy Physics*, 2022:47, 2022.

[47] ATLAS Collaboration. Search for heavy Majorana or Dirac neutrinos and right-handed w gauge bosons in final states with two charged leptons and two jets at $\sqrt{s} = 13$ TeV with the ATLAS detector. *Journal of High Energy Physics*, 2019:16, 2019.

[48] ATLAS Collaboration. Search for a right-handed gauge boson decaying into a high-momentum heavy neutrino and a charged lepton in pp collisions with the ATLAS detector at $\sqrt{s} = 13$ TeV. *Physics Letters B*, 798:134942, 2019.

[49] ATLAS Collaboration. Search for heavy Majorana or Dirac neutrinos and right-handed w gauge bosons in final states with charged leptons and jets in pp collisions at $\sqrt{s} = 13$ TeV with the ATLAS detector. *The European Physical Journal C*, 83:1164, 2023.

[50] Miha Nemeščček, Fabrizio Nesti, and Juan Carlos Vasquez. Majorana higgses at colliders. *Journal of High Energy Physics*, 2017:114, April 2017.

[51] Abdelhak Djouadi. The Anatomy of EWSB I: The Higgs boson in the Standard Model. *Physics Reports*, 457:1–216, 2008.

[52] Sudhanwa Patra, S. T. Petcov, Prativa Pritimita, and Purushottam Sahu. Neutrinoless double beta decay in a left-right symmetric model with a double seesaw mechanism. *Phys. Rev. D*, 107:075037, 2023.

[53] Miha Nemešek, Fabrizio Nesti, and Goran Popara. Keung-senjanović process at LHC: from LNV to displaced vertices to invisible decays. 2018. arXiv:1801.05813v2.

[54] CMS Collaboration. Search for third-generation scalar leptoquarks and heavy right-handed neutrinos in final states with two tau leptons and two jets in proton-proton collisions at $\sqrt{s} = 13$ TeV. *Journal of High Energy Physics*, 2017:121, 2017.

[55] CMS Collaboration. Search for heavy neutrinos and third-generation leptoquarks in hadronic states of two τ leptons and two jets in proton-proton collisions at $\sqrt{s} = 13$ TeV. *Journal of High Energy Physics*, 2019:170, 2019.

[56] CMS Collaboration. Search for z' bosons decaying to pairs of heavy Majorana neutrinos in proton-proton collisions at $\sqrt{s} = 13$ TeV. *Journal of High Energy Physics*, 2023:181, 2023.

[57] M. Cepeda et al. Report on the physics at the HL-LHC and perspectives for the HE-LHC. *CERN Yellow Reports: Monographs*, 7:1–220, 2019.

[58] A. Abada et al. FCC physics opportunities. *The European Physical Journal C*, 79:474, 2019.

[59] Alain Blondel, Elena Graverini, Nicola Serra, and Mikhail Shaposhnikov. Search for heavy right handed neutrinos at the FCC-ee. *Nuclear and Particle Physics Proceedings*, 273–275:1883–1890, 2016.

[60] Stefan Antusch, Eros Cazzato, and Oliver Fischer. Sterile neutrino searches at future $e^- e^+$, pp, and $e^- p$ colliders. *International Journal of Modern Physics A*, 32:1750078, 2017.

[61] CERN. The large electron-positron collider. https://home.cern/science/accelerators/large-electron-positron-collider/. Accessed: 2026-05-10.

[62] Ph Lebrun. Commissioning and First Operation of the Large Hadron Collider (LHC). Technical report, CERN, Geneva, 2010.

[63] R Alemany-Fernandez et al. Operation and Configuration of the LHC in Run 1. 2013.

[64] Jorg Wenninger. Operation and Configuration of the LHC in Run 2. 2019.

[65] Stephane Fartoukh et al. LHC Configuration and Operational Scenario for Run 3. Technical report, CERN, Geneva, 2021.

[66] Andrew J. Larkoski. *Elementary Particle Physics: An Intuitive Introduction*. Cambridge University Press, Cambridge, United Kingdom, 2019.

[67] Hannes Bartosik and Giovanni Rumolo. Performance of the LHC injector chain after the upgrade and potential development. Technical report, 2022. Contribution to Snowmass 2021.

[68] ALICE Collaboration. The alice experiment at the cern lhc. *Journal of Instrumentation*, 3:S08002, 2008.

[69] CMS Collaboration. The cms experiment at the cern lhc. *Journal of Instrumentation*, 3:S08004, 2008.

[70] LHCb Collaboration. The lhcb detector at the lhc. *Journal of Instrumentation*, 3:S08005, 2008.

[71] ATLAS Collaboration. Atlas data quality operations and performance for 2015–2018 data-taking. *JINST*, 15:P04003, 2020.

[72] Oliver Brüning and Markus Zerlauth. Lhc operation and the high-luminosity lhc upgrade project. *arXiv preprint arXiv:2505.03535*, 2025. Contribution to the CERN Accelerator School: Advanced Accelerator Physics, Spa, Belgium, 10–22 November 2024.

[73] ATLAS Collaboration. The atlas experiment at the cern large hadron collider. *Journal of Instrumentation*, 3:S08003, 2008.

[74] Peilian Liu and ATLAS Collaboration. Expected performance of the upgrade ATLAS experiment for HL-LHC. 2018.

[75] M. Limper. Atlas sct commissioning. In *Proceedings of a detector or instrumentation conference*, Amsterdam, The Netherlands, 2010. NIKHEF, on behalf of the ATLAS SCT Collaboration.

[76] E. Abat et al. The ATLAS transition radiation tracker (TRT) proportional drift tube: design and performance. *Journal of Instrumentation*, 3:P02013, 2008.

[77] ATLAS Collaboration. ATLAS insertable B-layer technical design report. Technical Report CERN-LHCC-2010-013, ATLAS-TDR-019, CERN, Geneva, September 2010.

[78] S. Navas et al. Review of particle physics. *Physical Review D*, 110:030001, 2024.

[79] ATLAS Collaboration. ATLAS liquid argon calorimeter technical design report. Technical Report CERN-LHCC-96-41, CERN, Geneva, 1996.

[80] ATLAS Collaboration. Electron and photon energy calibration with the atlas detector using data collected in 2015 at $\sqrt{s} = 13$ tev. Technical Report ATL-PHYS-PUB-2016-015, CERN, August 2016. ATLAS Public Note.

[81] Dag Gillberg and ATLAS Liquid Argon Calorimeter Group. Performance of the atlas forward calorimeters in first lhc data. In *Proceedings of Science (PoS)*, ICHEP 2010, page 421, Trieste, 2010. SISSA. On behalf of the ATLAS Liquid Argon Calorimeter Group.

[82] Luciano Pontecorvo. The atlas muon spectrometer. *European Physical Journal C*, 34:s117–s128, 2003. ATLAS Scientific Note, CERN.

[83] ATLAS Collaboration. ATLAS Public DAQ Plots. https://twiki.cern.ch/twiki/bin/view/AtlasPublic/ApprovedPlotsDAQ, 2019. Accessed: 2026-04-25.

[84] ATLAS Collaboration. Performance of the atlas detector at the lhc. *arXiv preprint arXiv:2305.16623*, 2024. Version 2, 7 June 2024.

[85] Markus Elsing, Luc Goossens, Armin Nairz, and Guido Negri. The ATLAS Tier-0: Overview and operational experience. *Journal of Physics: Conference Series*, 219:072011, 2010. Distributed Processing and Analysis.

[86] ATLAS Collaboration. Performance of the atlas trigger system in 2015. *Eur. Phys. J. C*, 77:317, 2017.

[87] Analysis Tutorial Contents - ATLAS Software documentation. Last updated October 29, 2025.

[88] T. Sjöstrand et al. An introduction to PYTHIA 8.2. *Comput. Phys. Commun.*, 191:159, 2015.

[89] J. Alwall et al. The automated computation of tree-level and next-to-leading order differential cross sections, and their matching to parton showers. *JHEP*, 07:079, 2014.

[90] C. Degrande et al. UFO - The Universal FeynRules Output. *Comput. Phys. Commun.*, 183:1201, 2012.

[91] S. Agostinelli et al. Geant4 – a simulation toolkit. *Nucl. Instrum. Meth. A*, 506:250, 2003.

[92] ATLAS Collaboration. Track and vertex reconstruction with the ATLAS inner detector. 2025.

[93] R. E. Kalman. A new approach to linear filtering and prediction problems. *Journal of Basic Engineering*, 82(1):35–45, 1960.

[94] ATLAS Collaboration. Electron and photon performance measurements with the ATLAS detector using the 2015–2017 LHC proton-proton collision data. 2019.

[95] ATLAS Collaboration. Topological cell clustering in the ATLAS calorimeters and its performance in LHC Run 1. *Eur. Phys. J. C*, 77:490, 2017.

[96] ATLAS Collaboration. Muon reconstruction and identification efficiency in ATLAS using the full Run 2 pp collision data set at $\sqrt{s} = 13$ TeV. 2020.

[97] ATLAS Collaboration. Jet reconstruction and performance using particle flow with the atlas detector. *Eur. Phys. J. C*, 77:466, 2017.

[98] Matteo Cacciari, Gavin P. Salam, and Gregory Soyez. The anti-k_t jet clustering algorithm. *JHEP*, 04:063, 2008.

[99] Matteo Cacciari, Gavin P. Salam, and Gregory Soyez. FastJet user manual. *Eur. Phys. J. C*, 72:1896, 2012.

[100] ATLAS Collaboration. Performance of missing transverse momentum reconstruction with the ATLAS detector using proton-proton collisions at $\sqrt{s} = 13$ TeV. 2018.

[101] A. Buckley et al. Implementation of the ATLAS Run 2 xAOD data format. Technical report, CERN, 2015.

[102] Gaudi Project. `https://gaudi.web.cern.ch/gaudi/`. Software framework for building High-Energy Physics data processing applications, developed at CERN for the LHCb and ATLAS experiments.

[103] ATLAS Collaboration. Performance of the ATLAS muon triggers in Run 2. *JINST*, 15:P09015, 2020.

[104] ATLAS Collaboration. Performance of electron and photon triggers in ATLAS during LHC Run 2. *Eur. Phys. J. C*, 80:47, 2020.

[105] Glen Cowan, Kyle Cranmer, Eilam Gross, and Ofer Vitells. Asymptotic formulae for likelihood-based tests of new physics. *The European Physical Journal C*, 71(2), February 2011.

[106] ATLAS Collaboration. ATLAS flavour-tagging algorithms for the LHC Run 2 pp collision dataset. *Eur. Phys. J. C*, 83:681, 2023.

[107] Ian Goodfellow, Yoshua Bengio, and Aaron Courville. *Deep Learning*. Adaptive Computation and Machine Learning. MIT Press, 2016.

[108] Aurélien Géron. *Hands-On Machine Learning with Scikit-Learn, Keras, and TensorFlow: Concepts, Tools, and Techniques to Build Intelligent Systems*. O'Reilly Media, 3 edition, 2022.

[109] ATLAS Collaboration. Documentation for TRExFitter. https://trexfitter-docs.web.cern.ch/trexfitter-docs, 2025.

[110] Wouter Verkerke and David Kirkby. The RooFit toolkit for data modeling. https://arxiv.org/abs/physics/0306116, 2003.

[111] Lorenzo Moneta et al. The RooStats project. https://arxiv.org/abs/1009.1003, 2011.

[112] Alexander L. Read. Presentation of search results: the CL_s technique. *Journal of Physics G: Nuclear and Particle Physics*, 28:2693, 2002.

[113] Steven Schramm and ATLAS Collaboration. Atlas jet reconstruction, calibration, and tagging of lorentz-boosted objects. In *Proceedings of the 6th International Conference on New Frontiers in Physics (ICNFP 2017)*, Kolymbari, Crete, Greece, 2017. EPJ Web of Conferences.

[114] ATLAS Collaboration. Jet energy scale and resolution measured in proton–proton collisions at $\sqrt{s}$ = 13 tev with the atlas detector. *European Physical Journal C*, 81(8):689, 2021.

[115] ATLAS Collaboration. Determination of jet calibration and energy resolution in proton–proton collisions at $\sqrt{s}$ = 8 TeV using the ATLAS detector. *Eur. Phys. J. C*, 80:1104, 2020.

[116] ATLAS Collaboration. Measurement of the muon reconstruction performance of the atlas detector using 2011 and 2012 lhc proton–proton collision data. *Eur. Phys. J. C*, 74:3130, 2014.

[117] ATLAS Collaboration. Studies of the performance of the ATLAS detector using cosmic-ray muons. *Eur. Phys. J. C*, 71:1593, 2011.

[118] Antonio Salvucci. Measurement of muon momentum resolution of the atlas detector. *EPJ Web of Conferences*, 28:12039, 2012. On behalf of the ATLAS Collaboration.

[119] ATLAS Collaboration. Electron and photon energy calibration with the ATLAS detector using LHC Run 1 data. *JINST*, 9:P10009, 2014.

Acknowledgments

Ora che questo capitolo della mia vita a Bologna sta per concludersi, mi ritrovo con tanti pensieri, storie ed emozioni che vorrei raccontare per rendervi partecipi di ciò che questi anni hanno significato per me, e che spero di riuscire a comunicare in queste poche righe. È stato un viaggio incredibile: i momenti belli sono stati immensamente belli, mentre quelli difficili mi hanno messa alla prova e, a volte, mi hanno fatto dubitare. Nonostante tutto, oggi mi sento profondamente grata e fortunata per aver avuto l'opportunità di vivere questa città e incontrare tutte le persone che ha portato nella mia vita.

Desidero innanzitutto ringraziare il Professor Maximiliano Sioli per l'opportunità che mi ha offerto attraverso questo lavoro di tesi, permettendomi di avvicinarmi allo studio della fisica oltre il Modello Standard, un ambito che ho scoperto essere estremamente affascinante e stimolante.
Ringrazio Antonio per il supporto costante, per la disponibilità e per avermi guidata e consigliata durante questo complesso percorso di ricerca.
Un ringraziamento speciale va ad Elisa, che fin dal primo momento mi ha accolta e accompagnata passo dopo passo in questi mesi di lavoro. Nonostante il ruolo formale di correlatrice, sei diventata un'amica speciale con cui condividere non solo gli sviluppi della tesi, ma anche un'infinità di gatti e memini. Non avrei mai immaginato di costruire un legame così bello e sono felice di essermi ricreduta. Grazie per la pazienza, per il sostegno e per essere stata molto più di una guida accademica.

Vorrei ringraziare i miei genitori e tutta la mia famiglia. Con grandi sacrifici mi avete permesso di studiare per tutti questi anni, regalandomi la possibilità di scegliere una strada che amo davvero. Senza di voi nulla di tutto questo sarebbe stato possibile. Mi dispiace se a volte sono stata distante o un po' scontrosa a causa dello stress, ma sappiate che vi ho sempre portato nel cuore e che continuerò a farlo ovunque andrò.

Vorrei ringraziare il mio cuoricino Leo, che in tutti questi anni è stato la mia certezza più grande. Insieme abbiamo condiviso vittorie e sconfitte, affrontato la distanza, siamo cresciuti e maturati insieme senza mai smettere di credere l'uno nell'altra. La tua presenza nei giorni più felici e in quelli più difficili, quando ero stanca o piena di energie, serena o nervosa non mi ha mai fatta sentita sola. Grazie per avermi aiutata a scoprire e ad apprezzare la parte migliore di me, e per non avermi mai fatto sentire sbagliata per quella più fragile. Sei la persona più genuina e autentica che abbia mai conosciuto e la tua bontà, dolcezza e rispetto con cui tratti chiunque ti circondi, mi ricordano ogni giorno di quanto sia fortunata

ad averti accanto e di quanto valore ci sia nella gentilezza. La tua presenza è stata, e continua a essere, un punto fermo nella mia vita. Ti amo ogni giorno di più.

Vorrei poi ringraziare tutti gli amici speciali che hanno reso gli anni dell'università, e non solo, davvero indimenticabili.
Un grazie speciale va a Chiara, che dal primo anno di università mi accompagna giorno dopo giorno in quella che è diventata la mia quotidianità. Grazie per le sessioni di studio, la Formula 1, le pizze del sabato sera, le serie sui vampiri e, soprattutto, per i gelatini pre-esame, che ormai ci legheranno per sempre. Grazie per i tuoi consigli, che riescono sempre, quasi magicamente, ad essere esattamente ciò di cui ho bisogno nel momento giusto, e per essermi accanto anche quando faccio fatica ad ascoltare. So che ci sarai sempre e per questo ti voglio un bene immenso.
Grazie a Lori, Bea e Leo per essere stati la mia banda di matti e la mia famiglia allargata, un ponte prezioso tra la vita aretina e quella universitaria. Con voi riesco sempre a dimenticare stress, ansie e paure, semplicemente ridendo e scherzando come se le preoccupazioni non esistessero. Abbiamo alle spalle tante birrette al limone e pane rabbit, e sono sicura che ne avremo ancora molte altre davanti. Non so se un giorno avrò il coraggio di raccontare ai miei figli tutto quello che abbiamo combinato insieme... ma conoscendovi, probabilmente lo farete voi. Vi voglio bene.
Grazie a Ene, Gio e Fra, che hanno sempre avuto la pazienza di ascoltare le mie infinite lamentele. In fondo lo so che ormai vi divertono. Le serate passate con voi sono tra i ricordi più belli, divertenti e spensierati che porterò con me di questi anni. Sono davvero grata di avervi conosciuti, perché siete riusciti a farmi credere un po' di più in me stessa, sia all'università che nella vita. Forse non ve ne siete mai accorti, ma per me è stato importante più di quanto possiate immaginare. E purtroppo per voi, non sarà facile liberarsi di me, neanche a chilometri di distanza.
Grazie agli amiketti di Arezzo (che non elencherò uno ad uno, ma voi sapete), che ci sono sempre ogni volta che torno a casa. Anche se passiamo gran parte del tempo lontani e mi mancate tantissimo, ogni ritorno sembra annullare la distanza e il tempo trascorso. Siete una colonna portante della mia vita e vi ringrazio per non avermi mai lasciata sola.
Grazie ai nuovi amiketti conosciuti durante la magistrale. È stato bellissimo condividere con voi questi ultimi due anni di università e spero davvero che questo sia soltanto l'inizio di una lunga amicizia.
Grazie ai colleghi del Collegium, che negli anni hanno saputo rendere più leggero e piacevole il clima dell'orchestra, anche nei momenti meno sereni. Vi ringrazio di cuore per aver condiviso con me questa esperienza e per la musica che abbiamo suonato insieme, rimarrà per sempre il filo che ci unisce.

Grazie a tutti voi. Grazie per esserci stati, per aver condiviso con me momenti, emozioni ed esperienze che custodirò con cura per tutta la vita. Ognuno di voi ha lasciato un segno dentro di me e ha contribuito a rendere questi anni così speciali. Qualunque sarà la strada che prenderemo da qui in avanti, porterò per sempre con me i ricordi, le risate, gli insegnamenti e l'affetto che mi avete donato.
Siete nel mio cuore.